

Quantifying the Impact of Imaging with Elevated Acoustic Output in Diagnostic Ultrasound

by

Yufeng Deng

Department of Biomedical Engineering
Duke University

Date: _____

Approved:

Kathryn Nightingale, Supervisor

Gregg Trahey

Stephen Smith

Donald Bliss

Clare Haystead

Dissertation submitted in partial fulfillment of the requirements for the degree of
Doctor of Philosophy in the Department of Biomedical Engineering
in the Graduate School of Duke University
2017

ABSTRACT

Quantifying the Impact of Imaging with Elevated Acoustic
Output in Diagnostic Ultrasound

by

Yufeng Deng

Department of Biomedical Engineering
Duke University

Date: _____

Approved:

Kathryn Nightingale, Supervisor

Gregg Trahey

Stephen Smith

Donald Bliss

Clare Haystead

An abstract of a dissertation submitted in partial fulfillment of the requirements for
the degree of Doctor of Philosophy in the Department of Biomedical Engineering
in the Graduate School of Duke University

2017

Abstract

Ultrasound imaging is one of the most widely used diagnostic imaging modalities. Abdominal ultrasound is typically used for screening liver diseases, and it is the recommended modality for six month screening in patients at risk for hepatocellular carcinoma (HCC). The major drawback of abdominal ultrasound is poor image quality that is insufficient for diagnosis, which is reported in 25-60% of patients, and is often correlated with obesity. Tissue harmonic imaging (THI) has become the default imaging mode for most abdominal imaging exams. It has also been applied in motion tracking in ultrasound elastography. THI provides better image quality through decreased sidelobe energy and decreased reverberation clutter in the abdominal wall compared to fundamental imaging. However, THI can be both signal-to-noise ratio (SNR) and penetration-depth limited during clinical imaging, resulting in decreased diagnostic utility.

A logical approach to increase the SNR of harmonic imaging is to increase the acoustic source pressure, but the acoustic output of diagnostic imaging has been subject to a *de facto* upper limit based upon the Food and Drug Administration (FDA) guideline for the Mechanical Index ($MI < 1.9$). This value was derived from historic values, rather than being linked to scientific evidence of bioeffects. A recent report from the American Institute of Ultrasound in Medicine (AIUM) concluded that exceeding the recommended maximum MI given in the FDA guidance up to an estimated *in situ* value of 4.0 could be warranted without concern for increased risk

of cavitation in non-fetal tissues without gas bodies, if there there were concurrent improvement in diagnostic utility.

This thesis presents the preliminary work of evaluating the potential diagnostic benefit of employing acoustic output beyond the FDA guideline of $MI = 1.9$ in the context of hepatic imaging. Three clinical studies were performed with goals of: (1) quantifying the image quality improvement of using elevated acoustic output in B-mode harmonic imaging; (2) assessing penetration depth changes in harmonic imaging; and assessing elevated MI in (3) harmonic motion tracking and in (4) acoustic radiation force impulse (ARFI) excitation of shear wave elasticity imaging (SWEI). High MI B-mode harmonic imaging resulted in modest increases in the contrast-to-noise ratio of hypoechoic hepatic vessels. Difficult-to-image patients who suffer from poor ultrasound image quality demonstrated larger improvement than easy-to-image subjects. The imaging penetration depth increased linearly with increasing MI, on the order of 4 – 8 cm per unit MI increase for a given focal depth. High MI harmonic motion tracking resulted in considerable increase in shearwave speed (SWS) estimation yield, by 27% and 37% at focal depths of 5 cm and 9 cm respectively, due to improved harmonic tracking data quality through increased SNR and decreased jitter of tissue motion data. In addition, SWS estimation yield was shown to be linearly proportional to the push (ARFI excitation) energy. SWEI measurements with elevated push energy were successful in patients for whom standard push energy levels failed. These studies suggested that liver capsule depth could be used prospectively to identify patients who would benefit from elevated output in push energy. These results indicate that using elevated acoustic output has the potential to provide clinical benefit for diagnostic ultrasound.

I would like to dedicate this dissertation to my family.

Table of Contents

Abstract	iv
List of Tables	xi
List of Figures	xii
List of Abbreviations and Symbols	xiv
Acknowledgements	xviii
1 Introduction	1
1.1 Clinical Motivation	1
1.2 Hypothesis	3
1.3 Thesis Outline	3
2 Background	5
2.1 Mechanical Index (MI)	5
2.1.1 Definition	5
2.1.2 Limitation of MI Assumptions	6
2.2 Non-linear Acoustics	8
2.2.1 Governing equations	8
2.2.2 Tissue non-linearity parameter B/A	12
2.2.3 Harmonic generation in sound propagation and shock formation	13
2.3 Ultrasonic B-mode imaging	15
2.3.1 Electronic noise	16

2.4	Tissue Harmonic Imaging (THI)	17
2.4.1	Implementation	17
2.4.2	Benefits and limitations of THI	20
2.5	Ultrasound Elasticity Imaging	21
2.5.1	ARFI and SWEI imaging	21
2.5.2	ARFI excitation	22
2.5.3	Displacement estimation and harmonic tracking	22
3	Analyzing the impact of increasing Mechanical Index (MI) and energy deposition on shear wave speed (SWS) reconstruction in human liver	25
3.1	Abstract	25
3.2	Introduction	26
3.3	Methods	28
3.3.1	Data acquisition sequence and SWS calculation	28
3.3.2	SWS yield	30
3.3.3	MI measurement	30
3.3.4	Clinical study design and population	31
3.4	Results	32
3.5	Discussion	38
3.6	Conclusions	44
4	Quantifying image quality improvement using elevated acoustic output in B-mode harmonic imaging	45
4.1	Abstract	45
4.2	Introduction	46
4.3	Methods	48
4.3.1	Imaging pulse parameters	48
4.3.2	B-mode sequence and contrast-to-noise ratio (CNR)	49

4.3.3	M-mode sequence and penetration depth (PD)	50
4.3.4	MI measurement	51
4.3.5	Clinical study design and population	52
4.4	Results	53
4.4.1	Mechanical Index (MI)	53
4.4.2	Contrast-to-noise ratio (CNR)	53
4.4.3	Penetration depth (PD)	57
4.5	Discussion	58
4.6	Conclusions	62
5	Evaluating the benefit of elevated Mechanical Index (MI) harmonic motion estimation in ultrasonic shear wave elasticity imaging (SWEI)	64
5.1	Abstract	64
5.2	Introduction	65
5.3	Methods	68
5.3.1	Data acquisition sequence and calibration	68
5.3.2	SWS calculation and SWS yield	69
5.3.3	Data quality metrics: correlation coefficient (CC), displacement jitter, and maximum displacement	69
5.3.4	Clinical study design and population	70
5.4	Results	72
5.5	Discussion	75
5.6	Conclusions	78
6	Challenges of developing high MI imaging systems	79
6.1	Saturation pressure	79
6.2	MI and MIE	80
6.3	Region of increased acoustic output	82

6.4	System non-linearity	82
6.5	Real-time high MI imaging systems	85
7	Conclusions	88
7.1	Future work	89
7.2	Technical and Clinical Contributions and Implications	91
	Bibliography	93
	Biography	103

List of Tables

3.1	Configurations of 8 SWEI excitations	29
3.2	Demographics of 26 study subjects.	33
3.3	Patient details from the 6 patients without any successful SWS measurements	36
4.1	Transmit frequency, focal depth, and MI configurations	49
4.2	Subject demographics, 25 subjects in total	52
5.1	Track beam configurations	68
5.2	Subject demographics, 25 subjects in total	71
5.3	Correlation coefficients (CC) and Signal-to-noise ratio (SNR) of the tracking data at both MI values for each focal depth	73

List of Figures

2.1	Two patients that have different liver capsule depths	7
2.2	Time domain and frequency spectrum of a sinusoidal wave initially and traveling for 5 cm	14
2.3	An example B-mode image on a phantom	16
2.4	Frequency spectrum of the transmitted pulses optimized for fundamental imaging and harmonic imaging	18
3.1	Pressure waveforms measured in water that were used in the study described in Chapter 3.	31
3.2	Example RANSAC and Radon sum SWS reconstructions	34
3.3	The combined percent yield across all patients versus push energy	35
3.4	Normalized peak ARFI displacement versus transmit push energy	35
3.5	Number of subjects for whom the energy level was the minimum for SWS measurement success	36
3.6	Percentage of successful subjects versus push energy levels	37
3.7	Per patient percent yield versus different parameters	38
3.8	Frequency spectra of the push waveforms and jitter levels	39
4.1	Pressure measurements using the 4C1 transducer with a focus at 6 cm	53
4.2	Sample B-mode and CNR results from an easy-to-image volunteer	54
4.3	Sample B-mode and CNR results from a medium-to-image volunteer	55
4.4	The number of hepatic hypoechoic structures that exhibited a CNR increase between matched low and high MI B-mode imaging	55

4.5	Percent CNR change as a function of subjective assessment of overall image quality	56
4.6	Percent CNR change versus focal depth	56
4.7	Penetration depth quantified from correlation coefficients	57
4.8	Penetration depth measurements at a given focal depth	58
4.9	THI images focusing at 5 cm in an obese volunteer	61
5.1	Percent yield of successful SWS measurements across all study subjects for low and high MI tracking	72
5.2	Example shear wave trajectories using low and high MI tracking focused at 5 cm	73
5.3	Correlation coefficients (CC) for each subject at low and high MI tracking	74
5.4	Displacement jitter computed from low and high MI tracking	74
5.5	Ratio of maximum displacements obtained with high and low MI tracking	75
5.6	Percent SWS yield at various image qualities	76
5.7	Scatter plot of liver capsule depths as a function of B-mode image quality	78
6.1	MI and MIE measurements	81
6.2	Region of increased acoustic output that was explored	83
6.3	Positive and negative leading edge transmit pulses measured with the hydrophone at the transducer surface at 2 scanner voltages	84
6.4	CC and RMS difference between positive and negative ledge pulses	85
6.5	Intensity distribution of an F/1.5 transmit focused at 6 cm using the 4C1 transducer	86
6.6	Example intensity distribution at -10° , 0.1° , 10° with respect to the apex of the 4C1 transducer	86
6.7	Intensity multiplier between the maximum intensity of a B-mode imaging case and a single transmit	87

List of Abbreviations and Symbols

Symbols

α Acoustic amplitude attenuation coefficient

B/A Tissue non-linear parameter

BW Fractional bandwidth of ultrasound transducer

β Coefficient of non-linearity ($1+B/2A$)

CC Correlation coefficient

c_o speed of sound

c_p Specific heat at constant pressure

c_v Specific heat at constant volume

δ Diffusivity of sound

E Energy

ϵ Acoustic Mach number

F Acoustic radiation force

$F/ F/\#$ of focal configuration ($F = \frac{z}{D}$)

f Center frequency

G Focusing gain

G_s Shear modulus

I Temporal average acoustic intensity

λ Ultrasound wavelength

K Bulk modulus

k Wave number
 κ Thermal conductivity
 l_d Shock distance
 μ Shear viscosity
 μ' Bulk viscosity
 p Acoustic pressure
 $p_{r,3}$ Attenuated (derated) peak-rarefactional acoustic pressure
 $p_{sat,f}$ Saturation pressure
 p_0 Source pressure
 ρ material density
 ρ_0 Equilibrium (ambient) density
 σ_s Shock parameter
 T Correlation window length
 ΔT Temperature change
 t Time
 u Particle velocity
 Z acoustic impedance
 z Focal depth

Abbreviations

ADC	Analog-to-digital converter
AIUM	American Institute of Ultrasound in Medicine
ARFI	Acoustic radiation force impulse
BMI	Body Mass Index
CNR	Contrast-to-noise ratio
CRLB	Cramér-Rao lower bound
FDA	Food and Drug Administration
FOV	Field of view
HCC	Hepatocellular carcinoma
IQ	In-phase and quadrature
IRB	Institutional Review Board
KZK	Khokhlov-Zabolotskaya-Kuznetsov
LHS	Left hand side
MI	Mechanical Index
MIE	Effective Mechanical Index
MTL	Multiple track location
NEMA	National Electrical Manufacturers Association
NX-corr	Normalized cross-correlation
PD	Penetration depth
PI	Pulse-inversion
PRF	Pulse repetition frequency
PRI	Pulse repetition interval
PRP	Peak rarefactional pressure
PVDF	Polyvinylidene difluoride
PZT	Lead zirconate titanate

RANSAC	Random Sample Consensus
RF	Radio-frequency
RHS	Right hand side
RMS	Root mean square
THI	Tissue harmonic imaging
SNR	Signal-to-noise ratio
STL	Single track location
SWEI	Shear wave elasticity imaging
SWS	Shearwave speed

Acknowledgements

First of all, I would like to thank Kathy for her guidance and support throughout my graduate career in her lab. Her enthusiasm in research has always been the driving force for me to move forward and she continued her support of my development throughout the journey of my graduate school career. It has been an honor to be a member of the Nightingale lab.

I am also thankful to the other members of my thesis committee for their time, support and enthusiasm for my work. I would like to specifically thank Gregg Trahey for the many valuable advice he gave me in my work and the numerous funny conversations that occurred in the lab and in the hall way of Hudson Hall Annex.

I would like to thank Mark Palmeri for all the valuable insights on research as well as many conversations about life and other random topics. Mark provided insight and inspiration in every project I have worked on, and provided tremendous help in the clinical studies. I would like to thank Ned Rouze who was always available to help me in my work. Ned was a great office mate, his focused approach to research and his attention to detail greatly impacted my daily work.

In addition, I would like to thank the clinical collaborators that I have worked during my graduate career, in particular, Clare Haystead, for her patience in the imaging room and her generous support despite her busy schedule.

There are many students and friends that I would like to thank for their advice, encouragement, and other help. Thank you to the members of the Nightingale,

Trahey, Wolf and Dahl labs for their support and daily interactions that made my graduate career enjoyable. Special thanks to Stephen Rosenzweig, for teaching me the joys (and pains) of working with ultrasound scanners.

I would like to acknowledge NIH grants R01-EB002132, R01-CA142824, and R01-EB022106 for funding my graduate research. I would like to thank Siemens Healthcare in Mountain View, CA for a valuable and enjoyable internship experience during my graduate studies.

Lastly, I would like to thank my parents for their support along the journey. I would not have accomplished any academic achievement without their love. I would like to thank all of my family and friends for their words of inspiration and encouragement.

1

Introduction

1.1 Clinical Motivation

Ultrasound imaging is one of the most widely used diagnostic imaging modalities, with advantages including its low cost, its real-time nature, and its lack of ionizing radiation. Abdominal ultrasound is widely used for screening liver diseases [57, 59], and it is the recommended modality for six month screening in patients at risk for hepatocellular carcinoma (HCC) [12, 7]. The major drawback of abdominal ultrasound is poor image quality that is insufficient for diagnosis, which is reported in 25-60% of patients [7, 95, 88, 50], and is often correlated with obesity[51, 85]. A recent study concluded that 34.9% of the adult population (20+ years) in the U.S is obese [23]. In obese patients, poor ultrasonic image quality arises from decreased penetration depth, and increased aberration, attenuation and reverberation clutter in the abdominal wall [51, 78].

Tissue harmonic imaging (THI) has become the default imaging mode for most abdominal imaging exams. THI is based upon nonlinear acoustic wave propagation, where images are created from the harmonics generated as the transmitted wave travels through biological tissues. Its success in creating higher quality ultrasound images compared to fundamental imaging is attributed to decreased sidelobe en-

ergy and decreased reverberation clutter in the abdominal wall. However, second harmonic pressure amplitude is generally 15-20 dB lower than the corresponding fundamental pressure [29]. Thus, THI can be both signal-to-noise ratio (SNR) and penetration-depth limited during clinical imaging, resulting in decreased diagnostic utility [85, 51, 25].

THI techniques have also been applied in tissue motion tracking in ultrasonic elasticity imaging methods [30, 3], to obtain higher quality tracking data utilizing the benefits of *in vivo* harmonic imaging. Harmonic tracking reduces the reverberation clutter and bias in tissue displacement estimates. On the other hand, harmonic tracking has the challenge of low SNR and low penetration depth similar to B-mode THI.

In addition, ultrasonic elasticity imaging methods suffer from depth penetration limitations due to insufficient tissue motion induced by acoustic radiation force impulse (ARFI) excitation. Studies routinely report technical failure and unreliable shear wave measurements for hepatic lesions deeper than 6-8 cm [74]. The failure rate increases with elevated patient Body Mass Index (BMI) [101] and in the presence of significant hepatic fibrosis [81]. These challenges likely result from: (1) significant propagation distances of ultrasound waves through subcutaneous fat in elevated BMI patients, which can attenuate ARF excitations, and (2) decreasing displacement amplitudes with increasing liver stiffness.

A logical approach to increase the SNR of harmonic imaging is to increase the acoustic source pressure, but the *in situ* pressures used in diagnostic imaging have been subject to a *de facto* upper limit based upon the Food and Drug Administration (FDA) guideline for the Mechanical Index ($MI < 1.9$) since 1992 [15]. This value was derived from historic values, rather than being linked to scientific evidence of bioeffects. A recent report from the American Institute of Ultrasound in Medicine (AIUM) concluded that exceeding the recommended maximum MI given in the FDA

guidance up to an estimated *in situ* value of 4.0 could be warranted without concern for increased risk of cavitation in non-fetal tissues without gas bodies, if imaging with an increased MI were associated with a corresponding significant clinical benefit [64].

No studies exist exploring the potential clinical benefit of employing elevated acoustic output beyond $MI = 1.9$ in diagnostic ultrasound, which is presented herein. Imaging systems with elevated acoustic output were developed and optimized in order to study the benefits of elevated acoustic output in the context of hepatic imaging.

1.2 Hypothesis

This dissertation proposes to quantify the impact of using elevated acoustic output in diagnostic ultrasound in the context of hepatic imaging. The goal is to determine if there is clinical benefit in exceeding the current FDA guideline for $MI = 1.9$ in diagnostic ultrasound. We explore the following hypotheses herein: (1) Using elevated acoustic output in ARFI excitation increases displacement and SWS estimation yield; (2) High MI B-mode harmonic imaging increases lesion visibility and imaging depth penetration; (3) Using elevated acoustic output in harmonic motion tracking improves tracking data quality and SWS estimation yield. These hypotheses were tested in three clinical studies presented in this thesis, and the data quality improvements associated with using elevated acoustic output were quantified by a series of image quality metrics, such as contrast-to-noise ratio (CNR), imaging penetration depth (PD), and SWS estimation yield.

1.3 Thesis Outline

This thesis encompasses the development and clinical evaluation of imaging sequences with elevated acoustic output. It includes three clinical studies that were dedicated to evaluate the image quality improvement of using elevated acoustic output in ARFI excitation, B-mode harmonic imaging, and harmonic motion tracking respectively.

Chapter 2 provides background information on the formulation of the Mechanical Index (MI) and the FDA guideline of MI for diagnostic ultrasound. The theory of non-linear acoustics is introduced, and the imaging methods of B-mode harmonic imaging and ultrasound elastography are presented.

Chapter 3 presents a clinical study that evaluates the benefit of using elevated acoustic output in the ARFI excitation (push pulse) in shear wave elasticity imaging at 2 MI values, 1.6 and 2.2. The Siemens Acuson SC2000TM was chosen for this work because of its technological improvements over previous generations of scanners, specifically its increased parallel receive capabilities and stable power supply for long duration push pulses. Chapters 4 and 5 present two additional clinical studies that focus on using elevated acoustic output ($MI \leq 3.3$) in B-mode harmonic imaging and harmonic motion tracking (track pulse) in shear wave imaging. The Siemens Acuson S2000TM was chosen for these studies due to its power supply capabilities to achieve high MI values.

Chapter 6 identifies the systematic and physical challenges we faced during the development of high MI imaging sequences and provides solutions to overcome some of these challenges. Finally in Chapter 7, the work presented in this thesis is summarized and future directions are outlined.

2

Background

2.1 Mechanical Index (MI)

2.1.1 Definition

The Mechanical Index (MI) was developed to predict cavitation events in the presence of optimally-sized gas bubbles in water [5]. Inertial cavitation is a bubble motion characterized by a large expansion followed by a violent collapse, which can generate damaging shock waves and raise the local temperatures as high as 5000 K. The MI definition used by the FDA is:

$$\text{MI} = \frac{p_{r.3}(z_{MI})}{\sqrt{f_{awf}}} \quad (2.1)$$

where $p_{r.3}(z_{MI})$ is the attenuated (derated) peak-rarefactional acoustic pressure at the depth z_{MI} (assuming an attenuation coefficient (α) of 0.3 dB/cm/MHz); z_{MI} is depth on the beam axis from the transducer to the plane of maximum attenuated pulse-intensity integral (which generally occurs near the shallower focal depth when the electronic lateral focus is away from the elevational lens focus [15]), and f_{awf} is the acoustic-working frequency [34].

The FDA established the MI as an acoustic output metric to address the potential risks of non-thermal mechanical effects during diagnostic ultrasound exams in

1992 [4]. The FDA adopted an MI threshold of 1.9, because this value corresponds to the maximum MI that was computed for ultrasound scanners in use prior to 1976 when the FDA began monitoring output, and, no deleterious events had been reported for ultrasonic imaging prior to 1976 [15]. This threshold value of 1.9 was determined not based upon reported evidence of bioeffects. The MI is commonly further limited by commercial ultrasound vendors when a 20–30% safety buffer is applied to reduce the number of production transducers requiring quality assurance testing [4, 103], which results in most current commercial scanners using a maximum MI between 1.3 and 1.6.

2.1.2 Limitation of MI Assumptions

The MI was developed to gauge the likelihood of inertial cavitation associated with diagnostic ultrasound, and its calculation is based upon the assumption of a pre-existing gas bubble in the path of the acoustic beam [5]. There are tissues in the body that naturally harbor gas bubbles, such as lungs and intestines. However, other biological tissues, such as the liver, are generally free of gas bubbles [66, 19]. In such tissues, the requisite amplitude of the ultrasound field for inducing cavitation is consistently reported to be relatively high. MI values > 5.0 are required to generate and detect cavitation when using diagnostic frequencies (i.e. $> 1\text{MHz}$), and pulse durations (i.e. $< 1\text{ msec}$) [64]. A recent report from the AIUM concluded that exceeding the recommended maximum MI given in the FDA guidance, up to an estimated *in situ* value of 4.0, could be justified without concern for increased risk of cavitation in these tissues, if that elevated MI imaging is associated with a significant clinical benefit [64].

The current FDA guidance specifies that MI measurements be made in water, and derated by a factor of $\alpha = 0.3\text{ dB/cm/MHz}$ to account for frequency-dependent attenuation in tissue. Ultrasound must pass through the body wall before reaching

the abdominal organs. The thickness of the body wall varies significantly among patients, typically being much thicker in overweight and obese patients. In practice, a wide range of energy levels occur *in vivo* for a given system output due to differences in imaging location and patient-to-patient variability in attenuation. In a liver study with 26 patients conducted by our group [26], the shallowest liver capsule was 20 mm from the skin surface, while deepest liver capsule was 45 mm from the skin surface. Figure 2.1 shows example liver images of two patients in this study. Their liver capsule depths varied significantly from 25 mm to 45 mm. Other factors such as liver fibrosis, inflammation, and steatosis further alter the *in vivo* energy level. As a result, a wide range of energy levels could occur for the same MI used in different patients.

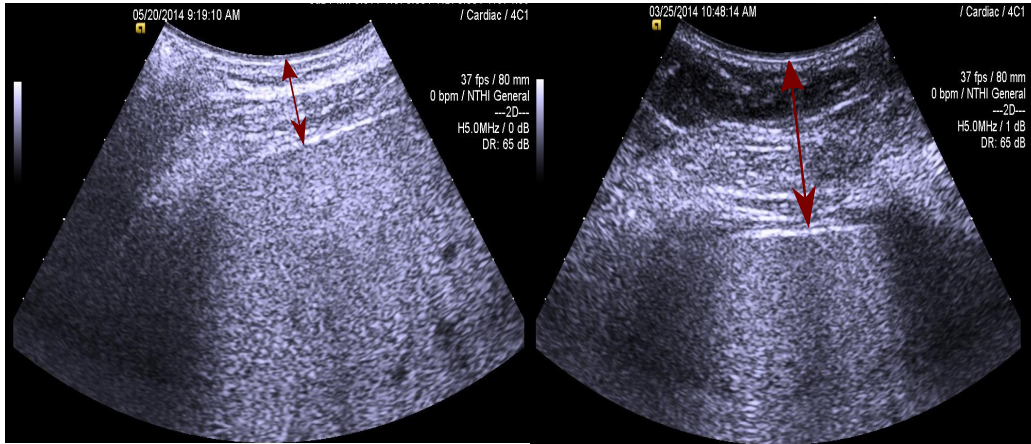


FIGURE 2.1: Two patients that have different liver capsule depths. Left: liver capsule depth = 25 mm. Right: liver capsule depth = 45 mm.

In addition, the single derating factor ($\alpha = 0.3 \text{ dB/cm/MHz}$) is lower than the actual attenuation that occurs in abdominal imaging. Liver has a typical attenuation of 0.5 dB/cm/MHz , while connective tissue and fat have different attenuations of 0.68 dB/cm/MHz and 0.40 dB/cm/MHz respectively [41]. As a result, the MI likely overestimates *in situ* acoustic energy levels in livers, especially in the overweight and obese patient population. The Effective Mechanical Index (MIE) was proposed

to accurately characterize *in situ* acoustic pressures [97, 58]. The MIE approach employs the estimated *in situ* p_r in the numerator of Equation 2.1, rather than using a derating factor of 0.3 dB/cm/MHz. The MIE provides a more calibrated reference for comparison of the actual *in situ* values of p_r associated with cavitation-mediated bioeffects in different experimental protocols, for which the prefocal losses are often not accurately modeled by an attenuation factor of 0.3 dB/cm/MHz. The MIE is thus more indicative of absolute safety thresholds compared to MI.

2.2 Non-linear Acoustics

2.2.1 Governing equations

Linear wave equation

When an acoustic wave passes through a compressible medium, there are dynamic fluctuations in the pressure, density, temperature, particle velocity, etc. These physical changes can be described by a series of coupled partial differential equations based on fundamental physics laws such as conservation of mass, momentum and energy. For example, in the classical case of a plane acoustic wave propagating through a homogeneous and lossless medium, the governing equations are given by [75]:

$$\rho_0 \frac{\partial \mathbf{u}}{\partial t} + \nabla p = 0, \text{ (momentum conservation)} \quad (2.2a)$$

$$\frac{\partial \rho'}{\partial t} + \rho_0 \nabla \cdot \mathbf{u} = 0, \text{ (mass conservation)} \quad (2.2b)$$

$$p = \frac{K}{\rho_0} \rho', \text{ (equation of state)} \quad (2.2c)$$

where \mathbf{u} is the particle velocity, p is the acoustic pressure, ρ is the density, ρ_0 is the equilibrium (ambient) density, $\rho' = \rho - \rho_0$, and K is the bulk modulus. These equations are first order, linear, partial differential equations, where higher order

terms have been ignored in their derivations. They are combined to give the linear second-order wave equation:

$$\nabla^2 p - \frac{1}{c_0^2} \frac{\partial^2 p}{\partial t^2} = 0, \quad (2.3)$$

where c_0 is the nominal wave speed. It can be derived from the bulk modulus (K) and the equilibrium density (ρ_0): $c_0 = \sqrt{K/\rho_0}$.

Non-linear equations

To extend the governing equations (2.2) for non-linear wave propagation, medium viscosity, and non-linearity need to be considered to construct a more realistic model for acoustic propagation. When these effects are considered for a thermoviscous medium, and keeping the second-order terms, the system of partial differential equations becomes [43]:

$$\rho_0 \frac{\partial \mathbf{u}}{\partial t} + \nabla p = (\mu' + \frac{4}{3}\mu) \nabla^2 \mathbf{u} - \frac{1}{2} \rho_0 \nabla(\mathbf{u} \cdot \mathbf{u}) - \rho' \frac{\partial \mathbf{u}}{\partial t} \quad (2.4a)$$

$$\frac{\partial \rho'}{\partial t} + \rho_0 \nabla \cdot \mathbf{u} = -\rho' \nabla \cdot \mathbf{u} - \mathbf{u} \cdot \nabla \rho', \quad (2.4b)$$

$$p = c_0^2 \left(\rho' + \frac{B}{2A} \frac{\rho'^2}{\rho_0} \right), \quad (2.4c)$$

where μ is the shear viscosity, μ' is the bulk viscosity. Shear viscosity accounts for diffusion of momentum between adjacent fluid elements having different velocities. Bulk viscosity provides an approximate description of non-equilibrium deviations between the actual local pressure and the thermodynamic pressure. B/A is called the tissue non-linearity parameter, and is discussed in more detail in the next section. These equations are combined to give the **Westervelt equation** (1963) for non-linear plane wave propagation in a thermoviscous medium:

$$\nabla^2 p - \frac{1}{c_0^2} \frac{\partial^2 p}{\partial t^2} + \frac{\delta}{c_0^4} \frac{\partial^3 p}{\partial t^3} = -\frac{\beta}{\rho_0 c_0^4} \frac{\partial^2 p^2}{\partial t^2} \quad (2.5)$$

where $\beta = 1 + B/2A$ is the coefficient of nonlinearity, and δ is the diffusivity of sound, δ is related to μ and μ' as:

$$\delta = \frac{1}{\rho_0} \left(\mu' + \frac{4}{3}\mu \right) + \frac{\kappa}{\rho_0} \left(\frac{1}{c_v} - \frac{1}{c_p} \right) \quad (2.6)$$

κ is the thermal conductivity of the medium, c_v and c_p are the specific heat of the media at constant volume and pressure respectively.

There are other commonly used equations that describe non-linear wave propagation. For example, the Burgers equation simplifies the Westervelt equation to take a one-dimensional form with an assumption of strictly forward propagating waves. The generalized Burgers equation takes into account the divergence (or convergence) of progressive spherical or cylindrical waves. The KZK (Khokhlov-Zabolotskaya-Kuznetsov) equation accounts for the combined effects of diffraction, absorption, and nonlinearity in directional sound beams.

Harmonic pressure amplitude

The magnitude of the second harmonic increases with the square of the acoustic pressure in the fundamental [16, 33]. This can be deduced from the frequency domain solution to the Burgers equation. The Burgers equation is the simplest model that describes the combined effects of non-linearity and dissipation on the propagation of 1-D plane waves, and it is the most widely used model equation for studying nonlinear acoustics. It can be derived from the Westervelt equation (Equation 2.5), and can be written as (page 57 of [43]):

$$\frac{\partial p}{\partial z} - \frac{\delta}{2c_0^3} \frac{\partial^2 p}{\partial \tau^2} = \frac{\beta}{\rho_0 c_0^3} p \frac{\partial p}{\partial \tau} \quad (2.7)$$

where $\tau = t - z/c_0$ represents the retarded time frame, i.e., the observer moves at speed c_0 in a reference frame. Consider a Fourier series representation of a trial

solution to Equation (2.7):

$$p(z, \tau) = \sum_{n=-\infty}^{\infty} P_n(z) e^{jn\tau}, \quad (2.8)$$

Substitute this solution into Equation (2.7):

$$\sum_{n=-\infty}^{\infty} \left(\frac{\partial P_n}{\partial z} + n^2 X P_n \right) e^{jn\tau} = Y \sum_{l=-\infty}^{\infty} P_l e^{jl\tau} \sum_{m=-\infty}^{\infty} jm P_m e^{jm\tau}, \quad (2.9a)$$

$$X = \frac{\delta}{2c_0^3}, Y = \frac{\beta}{\rho_0 c_0^3}, \quad (2.9b)$$

Let $n' = l + m$, the RHS (right hand side) of (2.9a) becomes

$$\sum_{n'=-\infty}^{\infty} \left(jY \sum_{m=-\infty}^{\infty} m P_m P_{n'-m} \right) e^{jn'\tau}, \quad (2.10)$$

The terms in the parentheses of the LHS (left hand side) of Equation (2.9a) and of Equation (2.10) are equal:

$$\frac{\partial P_n}{\partial z} + n^2 X P_n = jY \sum_{m=-\infty}^{\infty} m P_m P_{n-m} \quad (2.11)$$

The convolution term in (2.11) can be further extended, and let $k = m$:

$$\frac{\partial P_n}{\partial z} = -n^2 X P_n + jY \left(\sum_{k=1}^{n-1} k P_k P_{n-k} + \sum_{k=n}^{\infty} n P_k P_{k-n}^* \right), n = 1, 2, \dots, \infty. \quad (2.12)$$

Equation (2.12) describes the frequency domain solution to the Burgers equation. The first term of the RHS accounts for viscous attenuation in thermoviscous media, and the second term accounts for nonlinear generation. This is consistent with the derivation in [16], which was written in terms of particle velocity, and was derived

ignoring attenuation (X term is 0). In Equation (2.12), P_n is the n th term in a complex Fourier series describing the pressure waveform at a point in the field. The first summation term in the parentheses represents the accretion of the n th harmonic by nonlinear combination of other harmonics. The second summation term represents the depletion of the n th harmonic to other harmonics with a difference frequency equal to n th harmonic [16]. When n is equal to 2 (second harmonic P_2) in Equation (2.12), the first summation becomes $1P_1P_1$, which is equal to P_1^2 . The second summation can be approximated by the second term in that summation, $2P_3P_1^*$, which is negligible due to the relatively small amplitudes of the third harmonic. Thus, P_2 is proportional to P_1^2 in the absence of attenuation, i.e., the magnitude of the second harmonic is simply proportional to the square of the fundamental.

2.2.2 Tissue non-linearity parameter B/A

The ratio B/A has become a common term in the field of nonlinear acoustics. It originates from the Taylor series expansion of the variations of the pressure in a medium in terms of variations of the density [43]. It represents the fact that density does not follow linearly the changes in the applied pressure.

$$P - P_0 = \left(\frac{\partial P}{\partial \rho} \right)_0 (\rho - \rho_0) + \frac{1}{2!} \left(\frac{\partial^2 P}{\partial \rho^2} \right)_0 (\rho - \rho_0)^2 + \dots, \quad (2.13)$$

where P and ρ are pressure and density, respectively, P_0 and ρ_0 are their ambient values. Equation 2.13 can be expressed in a more succinct form:

$$p = A \left(\frac{\rho'}{\rho_0} \right) + \frac{B}{2!} \left(\frac{\rho'}{\rho_0} \right)^2 + \frac{C}{3!} \left(\frac{\rho'}{\rho_0} \right)^3 + \dots, \quad (2.14)$$

where $p = P - P_0$ is the sound pressure, $\rho' = \rho - \rho_0$ is the excess density, and

$$A = \rho_0 \left(\frac{\partial P}{\partial \rho} \right)_0 \equiv \rho_0 c_0^2, \quad (2.15a)$$

$$B = \rho_0^2 \left(\frac{\partial^2 P}{\partial \rho^2} \right)_0, \quad (2.15b)$$

$$C = \rho_0^3 \left(\frac{\partial^3 P}{\partial \rho^3} \right)_0, \quad (2.15c)$$

where c_0 is the nominal speed of sound. The ratio B/A can be calculated from the definitions in 2.15:

$$\frac{B}{A} = \frac{\rho_0}{c_0^2} \left(\frac{\partial^2 P}{\partial \rho^2} \right)_0. \quad (2.16)$$

The quantity B/A is directly related to the ratio of the quadratic to the linear terms in the Taylor series (Equation 2.14) and therefore quantifies the contribution of second harmonics in wave propagation. Higher order effects exist, but are commonly excluded from consideration because they are extremely small. Another parameter, $\beta = 1 + B/2A$, is called the coefficient of nonlinearity. The B/A and β parameters of many solutions and biological tissues have been measured and reported in the literature. Most commonly, water has a B/A of 5.0 at room temperature [10], which corresponds to a β of 3.5. Liver has a B/A of 7.6 [41], which corresponds to a β of 4.8.

2.2.3 Harmonic generation in sound propagation and shock formation

Harmonics are generated as a sound wave propagates in a non-linear material. Figure 2.2(a) illustrates the change in acoustic pressure as an initially sinusoidal wave propagates. The change is best characterized by noting the shift to the left of the maximum compression with respect to zero-crossing; and, conversely, the shift to the right of the peak rarefaction. The relative positions of peak compression and peak rarefaction become closer. This wave shape change leads to alterations in the frequency spectrum of the wave, as evident in Figure 2.2(b). A monochromatic wave progressively becomes richer in harmonic frequencies of the fundamental. In this

case, harmonic frequencies are present after the wave travels for 5 cm, while they are not present at the source.

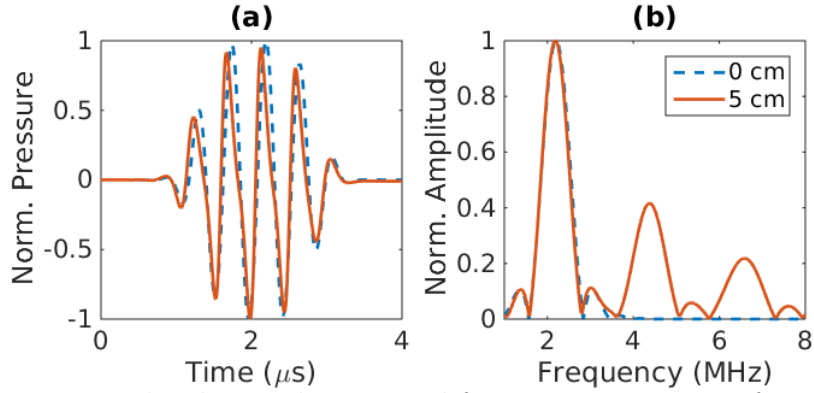


FIGURE 2.2: Normalized time domain and frequency spectrum of a sinusoidal wave initially (dotted line) and traveling for 5 cm (solid line) ignoring attenuation.

The explanation for this position change lies in the variation in phase speed v_t at different points on the wave. The phase speed is positively related to the local sound pressure, i.e., the phase speed is highest in the peak compression, and lowest in the peak rarefaction. The relationship between v_t and particle velocity u can be derived from the nonlinear wave equation (p.67 of [43]):

$$v_t = c_0 + (1 + B/2A)u = c_0 + \beta u, \quad (2.17)$$

the extent of variation of v_t across the sound wave is higher for materials that have a higher non-linear parameter B/A . In the case of a linear material where $B/A = 0$, the phase speed is constant across a wavelength of the sound wave, and no harmonics will be generated. This is rarely the case in diagnostic ultrasound, as most biological materials have a B/A between 5 – 12 (p.36 of [43]).

Eventually, the peak compression and peak rarefaction will coincide, and form a pressure discontinuity. This discontinuity is called an acoustic shock: the peak compression follows immediately and discontinuously behind the peak rarefaction [33]. The concept of acoustic shock leads to the definition of shock propagation distance

or discontinuity distance l_d . This is the point at which a shock first forms, and l_d is given by (p.72 of [43]):

$$l_d = \frac{1}{\epsilon k \beta}, \quad (2.18)$$

where ϵ is the acoustic Mach number, defined as u_0/c_0 , u_0 is the particle velocity at the source, and k is the wave number.

At an arbitrary distance z away from the source, the distortion of the wave can be conveniently described using the shock parameter σ_s :

$$\sigma_s = z/l_d = \epsilon k \beta z. \quad (2.19)$$

The shock parameter σ_s increases linearly with the distance traveled z , and with the coefficient of tissue nonlinearity β . In addition, there is linear dependence on ϵ , hence on the acoustic pressure at the source, and on k , the wave number. Since k is equal to $2\pi/\lambda$ or $2\pi f/c_0$, σ depends linearly on frequency. Increases in both source pressure and frequency increase the tendency for shocks to be generated as a wave propagates.

The shock parameter is often used to refer to distorted waveforms in a part quantitative, part descriptive way [33]. For σ_s below 0.1, the wave may be considered linear. $\sigma_s = 1$ is taken to be the threshold at which a pressure discontinuity has just formed. $\sigma_s = \pi/2$ marks the formation of a full shock and $\sigma_s = 3$ the formation of a saw-tooth wave. In diagnostic ultrasound imaging, the wave is usually in the weak shock regime, which means $0.1 < \sigma_s < 1$.

2.3 Ultrasonic B-mode imaging

B-mode imaging utilizes sound waves generated from the transducer, which propagates through tissue as longitudinal waves. The pressure and particle velocity at each spatial location are related by the acoustic impedance, which is dependent on

the density and speed of sound of the medium [22]. As the acoustic wave propagates through tissue, it is reflected and scattered due to acoustic impedance variations. The B-mode image is generated from the backscattered sound recorded by the transducer.

The ultrasound transducer converts the backscattered acoustic energy into an electrical signal, which then passes through the receive circuitry of the ultrasound scanner to form a B-mode image. The receive circuitry typically consists of pre-amplifiers, analog-to-digital converters (ADCs), analog and digital beamformers, and digital image formers. The received analog signal typically undergoes a depth dependent amplification to have uniform signal strength over depth, then it is converted to digital signals for down stream beamforming and processing.

2.3.1 Electronic noise

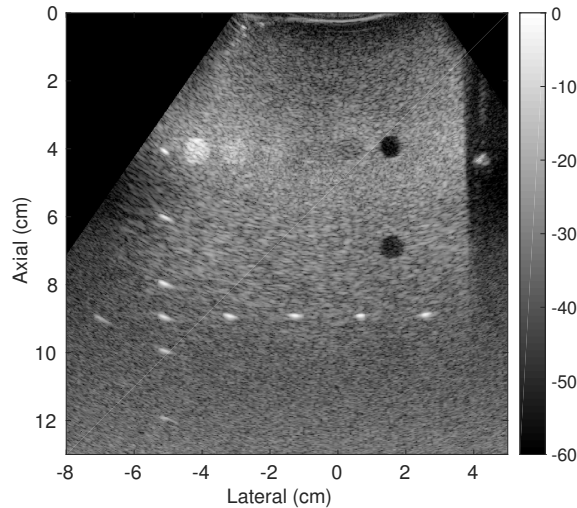


FIGURE 2.3: An example B-mode image on a phantom. The deepest 25% (beyond 9 cm) of the image is dominated by salt and pepper electronic noise and a lack of signal.

Uncorrelated electronic noise is typically present in B-mode images. There are two major sources of electronic noise: thermal sensor noise and intrinsic amplifier noise [42]. Sensor noise is due to thermal molecular activity in the transducer and the

acoustic medium it is connected to. The available sensor noise power is proportional to the absolute temperature and the bandwidth. Amplifier noise is primarily caused by electrons crossing a potential barrier. This noise is denoted shot noise and is proportional to the DC-currents in the transistors and the bandwidth of the system.

The electronic noise can be viewed as a Gaussian distributed white noise source. Figure 2.3 shows an example B-mode image on a phantom. The deepest 25% (beyond 9 cm) of the image is dominated by electronic noise and a lack of signal (< -60 dB). The electronic noise manifests as a "salt-and-pepper" noise in the B-mode images and is temporally varying.

2.4 Tissue Harmonic Imaging (THI)

THI is a nonlinear imaging modality that is the default imaging mode by most commercial clinical abdominal imaging systems. The emergence of THI started from ultrasound contrast agents. Contrast bubbles form a local source of nonlinearity in an acoustic field. As a result, the backscattered sound from contrast agents is rich in harmonics, and it can be distinguished from echoes from elsewhere [24]. However, it was later discovered that harmonic images could be obtained without the introduction of contrast agents, and these images demonstrated better quality than conventional Bmode images.

2.4.1 Implementation

Given the finite bandwidth of an ultrasound transducer, THI sequences typically transmit at a frequency that is lower than the center frequency of the transducer, to allow reception of the second harmonics included within the higher end of the transducer bandwidth. The earliest method of THI post-processing was to perform a high-pass filter on the received data, to separate the second-harmonic signal from the fundamental [28]. However, this method only works well at the expense of ax-

ial resolution. The transmit pulses optimized for a fundamental imaging case, by design, are broadband and have short pulse lengths to maximize axial resolution. The frequency spectrum of such an imaging pulse is shown in Figure 2.4(a). The fundamental and second harmonic bands overlap due to the broad bandwidth of the fundamental signal. The result is that the fundamental band corrupts the harmonic images obtained after filtering. To achieve better performance of THI images, the shape of the transmitted spectrum and its bandwidth need to be carefully modified to minimize the overlap between fundamental and harmonic bands. The optimized spectrum for harmonic imaging is shown in Figure 2.4(b). The fundamental band is narrowed to avoid overlap. This approach minimizes the corruption of fundamental signal in THI images at the expense of axial resolution.

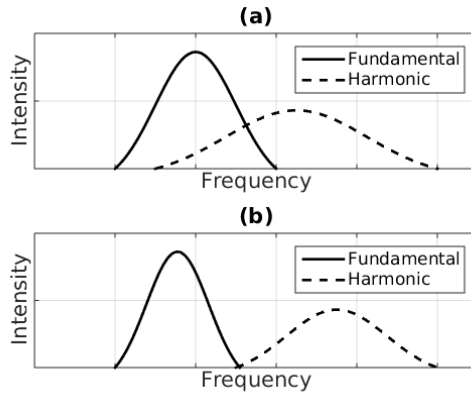


FIGURE 2.4: (a): Frequency spectrum of the transmitted pulse optimized for fundamental imaging. There is overlap between the fundamental band and the harmonic band. (b): Frequency spectrum of the transmitted pulse optimized for harmonic imaging. Overlap between fundamental and harmonic bands is eliminated by narrowing the fundamental band.

Pulse-inversion (PI) harmonic imaging was later proposed to isolate the second-harmonic signals and make harmonic images while maintaining bandwidth and axial resolution [29]. PI techniques generally use two transmit-receive cycles for each scan line in the image, with the second transmit pulse 180° out of phase with the first. Both the first pulse and the second, mirror-image pulse, undergo nonlinear distortion

as they travel through the tissue, forming harmonics. With Fourier analysis of the distorted waveform, it can be shown that the fundamental and odd-order harmonics (3rd, 5th, and so forth) retain their mirror image 180° phase relationship. The even order harmonics (2nd, 4th, and so forth), however, are in-phase and therefore add to form a stronger harmonic signal than either generates alone [14]. An image formed from these two pulses consists solely of echoes from the in-phase even harmonics, with the fundamental band removed through phase cancellation. Practically, the summed PI image only contains the second harmonic signal because the limited transducer bandwidth filters harmonics beyond the second harmonic.

Given the benefit of higher SNR and freedom to use broadband transmit, PI harmonic imaging is typically the default method for THI. However, PI implementations using sequential transmit-receive cycles for each scan line imply that the frame rate is half that obtained with fundamental mode imaging. Combining PI harmonics with parallel receive processing and coherent beam formation, it is possible to reduce the frame rate penalty of PI harmonics. Doherty *et al.* proposed fully sampled harmonic imaging, where each (+) pulse is summed with the subsequent (-) pulse, and each (-) pulse is also summed with the subsequent (+) pulse, to construct a harmonic signal with a temporal sampling frequency equal to the pulse repetition frequency [30].

PI harmonic imaging is used in the work presented in this thesis. It only works well if the fundamental signals completely cancel out each other between the 2 pulses that are 180° out of phase, so that all the signal left is the generated harmonic signals when the transmitted sound wave propagates through the tissue. Imperfect cancellation of the out-of-phase transmitted signals can introduce undesirable harmonic content in the received signal and degrades harmonic image quality. This was monitored in the clinical studies presented in this thesis, and is further discussed in Chapter 6.

2.4.2 Benefits and limitations of THI

THI images typically offer better image quality compared to fundamental images. The significant factors that contribute to the improvement in THI image quality include: (1) reduced side lobe levels; (2) reduced susceptibility to aberration; and (3) reduced reverberation clutter [33, 29, 16]. At the edges of the sound beam, the pulse amplitude is lower than on the axis and harmonics are poorly generated. Therefore, the side lobe levels for harmonics are low, and THI images are better at suppressing off-axis bright structures. In addition, harmonic generation builds up only during the propagation of the transmit pulse when there is sufficient pressure to generate nonlinearity, which typically occurs near the focal region, bypassing the aberrating tissues near the skin surface in many cases. Therefore, THI images only suffer one-way phase aberration when the echoes propagate back to the transducer, as compared to two-way aberration (transmit and receive) for fundamental images. Moreover, the propagation of return echoes is accompanied by no further significant harmonic generation, because of their low amplitude. This is also true for any reverberant echoes, whose harmonic content will be limited to only that generated by the transmission to the target. THI has been shown to produce better image quality clinically in many applications [68, 67, 45].

The magnitude of the fundamental signal increases linearly with source pressure, whereas the magnitude of the harmonic signal increases quadratically with source pressure [16]. Even so, the harmonic signals generated during nonlinear wave propagation in current commercial implementations are typically 15-20 dB lower than the fundamental signals [16]. Thus, THI approaches can be both SNR and penetration-depth limited during clinical imaging, resulting in decreased diagnostic utility [68, 82]. A logical solution would be to increase the transmitted source pressure; however, the maximum pressure that is employed by current commercial systems has been limited

by the *de facto* limit established by the FDA guidelines for the MI, as described in Section 2.1.

2.5 Ultrasound Elasticity Imaging

2.5.1 ARFI and SWEI imaging

Ultrasound elasticity imaging methods have been under investigation since the mid 1990's. Tissue elasticity is known to be associated with underlying pathological conditions, and ultrasound elasticity imaging methods are able to image these features non-invasively to provide diagnostic information. Acoustic Radiation Force Impulse (ARFI) imaging provides information about relative differences in tissue stiffness, similar to those generated with compressive strain imaging methods. However, ARFI offers advantages over compressive strain methods due to its limited susceptibility to out of plane motion artifacts and operator dependence. On the other hand, Shear Wave Elasticity Imaging (SWEI) quantifies tissue stiffness by exciting the tissue with an ARFI push and measuring the speed of the associated shear wave propagation. Both methods use long duration focused ultrasound waves to generate ARFI excitations to induce tissue motion, and use standard ultrasound imaging techniques to track the tissue displacement. ARFI measures on-axis displacement, and portrays relative differences in the displacement response within each excited region. For a given force, displacement is inversely proportional to tissue stiffness. SWEI monitors the off-axis tissue displacement and tracks the shear wave originating from the ARFI push to measure the speed of propagation. The shear wave speed (SWS) measured is related to the material's shear modulus. For a homogeneous, linear, elastic, isotropic material, SWS is proportional to the square root of the shear modulus G_S divided by the density ρ :

$$\text{SWS} = \sqrt{\frac{G_S}{\rho}}. \quad (2.20)$$

SWS typically has units of m/s, shear modulus (G_S) of soft tissue typically has units of kPa, and ρ is usually assumed to be 1 g/cm³ for soft tissue. Many clinical applications of these techniques in various organs and diseases have been reported in the literature, such as liver fibrosis staging [73], bladder dysfunction [62], kidney monitoring [40], thyroid gland [86], breast [9], and prostate cancer detection [102].

2.5.2 ARFI excitation

As the acoustic wave propagates through a medium, it also transfers momentum to the medium due to scatter and absorption, which results in the acoustic radiation force (ARF). The radiation force can be modeled by [65]:

$$F = \frac{2\alpha I}{c_0}, \quad (2.21)$$

where F is the radiation force [$kg/(s^2cm^2)$], I is the temporal average acoustic intensity [W/cm^2], α is the acoustic attenuation [Np/m], and c_0 is the speed of sound [m/s].

ARF is generated whenever acoustic waves propagate through a medium. However, to harness this force for ultrasonic elasticity imaging, high energy, relatively long duration ($> 100 \mu s$) focused ultrasonic waves are typically used to generate micron level tissue displacements [31]. The radiation force is directly proportional to the intensity of the acoustic beam, which is proportional to the square of pressure amplitude. Using elevated MIs in ARFI excitation would result in larger ARF magnitude, which in turn results in higher tissue displacement.

2.5.3 Displacement estimation and harmonic tracking

Displacement estimation is an important step in all ultrasound elasticity imaging methods. M-mode type ultrasound pulses are transmitted and received several times at the same region of interest of tissue before and after the ARFI push. The tissue dis-

placement can be estimated by comparing the ultrasound data using cross-correlation approaches or phase based methods [77]. The magnitude of tissue displacement from ARFI excitation is typically on the order of 0–30 microns.

Harmonic imaging methods have been proposed for the tracking sequences of ultrasound elasticity imaging [30, 89], to obtain higher quality tracking data utilizing the benefit of *in vivo* harmonic imaging. Similar to the benefits of THI, harmonic tracking can reduce bias in tissue displacement estimates from strong off-axis scatterers, reverberation clutter, and phase aberration. In addition, harmonic tracking also reduces underestimation bias associated with a smaller tracking beam size [70]. Song *et al.* showed that the shear wave SNR increased by 5.4 dB using PI harmonic tracking as compared to fundamental tracking, when imaging a phantom through excised pork belly [89]. Doherty *et al.* showed that harmonic tracking provided higher contrast in ARFI images of carotid arteries [30].

On the other hand, harmonic tracking can be susceptible to higher jitter due to its generally lower SNR. Jitter measures the magnitude of random errors arising from displacement estimation. Based upon the Cramér-Rao lower bound, a theoretical lower limit of the jitter can be expressed as [96]:

$$\text{Jitter} \geq \sqrt{\frac{3}{2f_c^3\pi^2T(BW^3 + 12BW)} \left(\frac{1}{CC^2} \left(1 + \frac{1}{SNR} \right)^2 - 1 \right)}, \quad (2.22)$$

where f_c is the center frequency, T is the correlation window length, BW is the fractional bandwidth, CC is the correlation coefficient between the signals, and SNR is the electronic signal-to-noise ratio. For harmonic tracking, f_c is higher and would result in smaller jitter. However, because of the SNR and depth penetration limitations of THI, CC and SNR can be lower for harmonic tracking, therefore resulting in higher jitter. We hypothesize that using elevated acoustic output in harmonic tracking will increase the SNR of the harmonic signal, therefore decreasing the jitter of

displacement tracking, and increasing the success rate of ARFI and SWEI imaging.

3

Analyzing the impact of increasing Mechanical Index (MI) and energy deposition on shear wave speed (SWS) reconstruction in human liver

This chapter has been published in the journal of Ultrasound in Medicine & Biology, 41(7):1948 – 1957, 2015.

3.1 Abstract

Shear wave elasticity imaging (SWEI) has found success in liver fibrosis staging. This work evaluates hepatic SWEI measurement success as a function of push pulse energy using 2 Mechanical Index (MI) values (1.6 and 2.2) over a range of pulse durations. Shear wave speed (SWS) was measured in the livers of 26 study subjects with known or potential chronic liver diseases. Each measurement consisted of 8 SWEI sequences, each with different push energy configurations. The rate of successful SWS estimation was linearly proportional to the push energy. SWEI measurements with higher push energy were successful in patients for whom standard push energy levels failed. The findings also suggest that liver capsule depth could be used prospectively to identify patients who would benefit from elevated output. We conclude that there is clinical benefit to using elevated acoustic output for hepatic SWS measurement in patients

with deeper livers.

3.2 Introduction

Liver biopsy has been the gold standard for staging liver fibrosis [100], with common disease etiologies such as viral hepatitis [94, 80], metabolic diseases [48, 13], autoimmune diseases [55] and toxin-related causes [61]. However, due to its invasiveness, risk of patient discomfort and lack of sensitivity [6], liver biopsy is poorly suited as a diagnostic test for longitudinal monitoring. Recently, Shear Wave Elasticity Imaging (SWEI) [84], has found success in the staging of liver fibrosis [73, 72, 52, 79, 38, 44, 47, 54, 36]. However, studies routinely report depth penetration limitations and exclude patients with livers and hepatic lesions deeper than 6-8 cm [74], and technical failure and unreliable measurement rates for liver stiffness have been reported to increase both with elevated patient BMI (a measure of obesity) [101], and in the presence of significant hepatic fibrosis [81]. These challenges likely result from: (1) significant propagation distances of ultrasound waves through subcutaneous fat in patients with higher BMIs, which can attenuate acoustic radiation force impulse (ARFI) excitations and abberate tracking ultrasound beams, and (2) smaller displacement amplitudes in stiffer livers. Current clinical SWEI protocols require 10 successful measurements for each patient, and record the median value of the 10 measurements [90]. Herein we test the hypothesis that a stronger acoustic radiation force excitation will increase the SNR of the shear wave signal as well as increasing the percentage of successful SWS estimates.

The tissue displacement magnitude is proportional to the amount of momentum change induced by the ‘acoustic radiation force impulse’, which is given by:

$$ARFI = \frac{2\alpha I}{c}t, \quad (3.1)$$

where α represents the ultrasonic attenuation of the tissue, I represents the pulse-

average intensity of the acoustic beam, c is the sound speed, and t is the duration of ARFI push. In a given material, where α and c are fixed, increasing the tissue displacement is achieved by using an ARFI push with higher impulse. Technical approaches to increase the push impulse include: (1) generating higher intensities (I) and (2) increasing the duration of the ARFI excitation. The peak pressure, and thus intensity, of commercial systems is limited by the U.S Food and Drug Administration (FDA) guidelines on Mechanical Index ($MI = P_{-.3}/\sqrt{f_c}$, where $P_{-.3}$ is the peak-rarefactional pressure derated by $\alpha = 0.3$ dB/cm/MHz, and f_c is the center frequency) [35].

The acoustic output of diagnostic ultrasonic imaging systems in the United States has been limited to an MI of 1.9 by FDA guidelines based on substantial equivalence with commercial products in the market prior to 1976 [2]. The MI guideline is intended to minimize the potential risks of non-thermal bioeffects, such as inertial cavitation, during diagnostic ultrasound exams. Inertial cavitation, i.e., bubble motion characterized by a large expansion followed by a rapid, violent collapse, can radiate damaging shock waves and raise the local temperature to as high as 5000 K, producing large numbers of reactive free radicals [21]. The MI formulation is based on the assumption of pre-existing bubbles in water [5], but the cavitation threshold in viscoelastic tissues, such as liver, can be twice compared to that in water [18]. A recent theoretical analysis of pressure thresholds for cavitation with pulses typically employed in ARFI imaging in tissue-like viscoelastic materials with a bubble present indicated that an MI value of 1.9 represents a conservative guideline in the context of hepatic imaging [20]. Further, endogeneous cavitation nuclei are rare in most soft tissues [66]. In tissues such as the liver that are not known to contain well defined gas bubbles, theoretical models indicate that the likelihood of inducing a cavitation related bioeffect with an ultrasound signal with an MI of 4.0 is 1 in 10,000,000 [37].

This work presents a clinical study that evaluates hepatic SWEI measurement

success as a function of ARFI push energy using 2 MI values (1.6 and 2.2) over a range of pulse durations. The goal is to quantify the effect of increasing push energy on measurement success and to determine if there is clinical benefit in exceeding the current MI FDA guideline of 1.9 in the context of hepatic SWEI measurements.

3.3 Methods

3.3.1 Data acquisition sequence and SWS calculation

Group SWS was measured using a modified Siemens Acuson SC2000TM ultrasound scanner (Siemens Healthcare, Ultrasound Business Unit, Mountain View, CA, USA) and an Acuson 4C1 curvilinear transducer. Each measurement consisted of 8 SWEI sequences, each with different ARFI push energy configurations. Four of 8 pushes had an MI of 1.6, which is typical of ARFI/SWEI on commercial scanners; through increased excitation voltage, the other four pushes had a higher MI of 2.2. Pairs of MI 1.6 and 2.2 sequences had matched scanner excitation transmit energy (E) by adjusting the pulse duration. The scanner excitation transmit energy (E) was calculated as the energy used to generate the push impulse,

$$E = \frac{V_{rms}^2}{Z} t \quad (3.2)$$

where V_{rms} is the root mean square of the excitation voltage, Z is the transducer impedance at the center frequency of the push pulse as specified on the scanner, and t is the push duration. Table 3.1 presents a summary of the 8 push pulses. The smallest energy used in this study was 4.0 mJ (Sequence 1), which is typical of commercial SWEI. In this study, we have encountered scanner power droop over the course of ARFI pushes. The pressure amplitude gradually decays towards the end of the push pulses. All of the sequences were characterized for scanner droop, which was incorporated into the energy calculations in Table 3.1. The push pulse

Table 3.1: Configurations of 8 SWEI excitations, Sequence #1 is similar to the energy used in current commercial SWEI implementations, Sequence #3 and #5 (bold) are a pair of high and low MI sequences that have the same excitation transmit energy (E), which was computed using Equation 2.

Seq Number	MI	$I_{sppa}(W/cm^2)$	duration (μs)	E (mJ)
1	1.6	420	364	4.0
2	1.6	420	546	6.0
3	1.6	420	727	8.0
4	1.6	420	1000	10.2
5	2.2	730	157	8.0
6	2.2	730	176	9.0
7	2.2	730	309	15.2
8	2.2	730	411	17.5

was transmitted with a center frequency of 2.2 MHz, and had a fixed F/1.5 focus near 50 mm axially.

Pulse-inversion harmonic tracking at 4 MHz was used for all sequences to reduce the clutter in tracking data [30]. The pulse repetition frequency (PRF) was 5 kHz. Due to equipment limitations, the MI for both pushing and tracking beams was the same for a given sequence. Eight repeated measurements were performed in each patient, and the order of the 8 pushes within each measurement was randomized to avoid systematic errors.

All post-processing tasks were completed offline using Matlab (R2012a, MathWorks®), Natick, MA). Displacement estimation was performed using a phase-shift estimator on the beamformed in-phase and quadrature (IQ) data [53, 77]. SWS was reconstructed using the Random Sample Consensus (RANSAC) [98] algorithm applied to arrival times of the peak particle velocities, and the Radon Sum [83] algorithm applied to the particle velocity data.

3.3.2 SWS yield

In this study, SWEI measurements with less than 50% inliers in the RANSAC algorithm were considered unsuccessful and were rejected, consistent with previously published *in vivo* liver data [98]. In addition, it has been shown that the RANSAC and Radon sum algorithms reconstruct SWS estimates with good agreement, with a correlation coefficient of 0.91 [83]. Therefore, acquisitions were also rejected when the SWS estimates from the two algorithms differed by more than 15%.

Differences between SWS measurements as a function of energy level were determined using a one-way ANOVA for each patient. A p-value exceeding 0.05 meant that the SWS measurements were not significantly different. A post-hoc Tukey's range test was applied in conjunction with an ANOVA for patients that had $p < 0.05$, to find the push energy level that produced SWS measurements significantly different from others.

3.3.3 MI measurement

Acoustic output pressure measurements were made in accordance with the AIUM/NEMA standard [4]. The measurements were performed in a water tank with the 4C1 transducer directly coupled to a 3D stepper motor-controlled translation stage (Newport, Irvine, CA). The transducer was configured to transmit 10-cycle push pulses at a PRF of 10 Hz to avoid heating of the transducer. The pressure waveform was measured with a calibrated membrane hydrophone (PVDF, with a 0.6 mm spot size, Sonic Technologies, Wyndmoor, PA). Custom LabView (National Instruments, Austin, TX) programs were written to translate the hydrophone and automatically trigger the scanner to transmit the desired pulses and the oscilloscope to record pressure waveforms. Five repeated measurements were acquired and averaged at each position in a 3D grid ($3.9 \text{ mm} \times 1.2 \text{ mm} \times 1.5 \text{ mm}$, axial \times lateral \times elevational) centered around the focal point using a step size of 0.3 mm, in order to capture the

global maximum of the acoustic pressure.

The pressure waveform was estimated from the recorded voltage waveform by deconvolution based on the magnitude of the sensitivity of the hydrophone [99]. This deconvolution method reduces over-estimation of the peak negative pressure arising from non-uniform hydrophone sensitivity. After voltage to pressure conversion, the MI was obtained by derating the peak-rarefactional pressure by 0.3 dB/cm/MHz at the center frequency (2.2 MHz) of the transmit waveform, and then dividing by the square root of center frequency of the push pulse [35]. Figure 3.1 shows example pressure waveforms of 10-cycle pulses at both MIs. The pressure waveforms were also measured in lossy media (a solution of evaporated milk and water with $\alpha = 0.5$ dB/cm/MHz) to more closely match *in vivo* imaging [92].

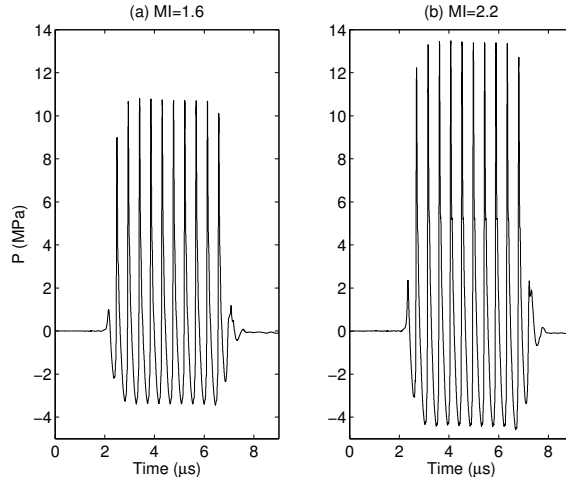


FIGURE 3.1: 10 cycles of the pressure waveforms measured in water that were used in this study. (a): peak-rarefactional pressure = 3.43MPa, which corresponds to MI = 1.6 and $I_{sppa.3} = 420 W/cm^2$. (b): peak-rarefactional pressure = 4.59MPa, which corresponds to MI = 2.2 and $I_{sppa.3} = 730 W/cm^2$.

3.3.4 Clinical study design and population

Twenty six study subjects with known or potential chronic liver diseases were recruited. This clinical study was approved by the Institutional Review Board at the Duke University, and each study subject provided written informed consent prior

to enrollment. Patient age, BMI, and fibrosis stage (if a liver biopsy had been performed) were recorded. Liver capsule depth was measured from the Bmode image for each study subject.

All 8 repeated SWEI measurements per study subject were performed at the inferior-intercostal location (i.e., 10-11th rib intercostals space coinciding most often with the location of the liver biopsy needle insertion), and a single trained imager completed all imaging tasks to avoid inter-operator variability. Study subjects were asked to pause breathing during each data acquisition, which lasted approximately 8 seconds. After the study subject paused breathing, an imaging location was targeted in a homogeneous liver region on Bmode imaging, devoid of any vessels or other structures. The study subject was instructed to resume breathing after each measurement.

3.4 Results

Table 3.2 summarizes patient demographics in this study. The study subjects cover a wide range of BMI and all fibrosis stages.

Figure 3.2 shows example RANSAC and Radon sum results. The top row portrays data from a successful SWS measurement, whereas the bottom row shows a dataset that was rejected due to its low percentage of inliers and the disparity between the two SWS estimation methods.

Figure 3.3 shows the total percent yield of successful SWS measurements as a function of scanner energy (E). The number of successful SWS reconstructions was summed over 8 repeated measurements for all 26 subjects to determine the total yield at each push energy level. The percent yield was then calculated by normalizing the total yield by the total number of measurements at each energy level (8 repeated measurements \times 26 study subjects = 208). The total percent yield for the highest energy excitation was 48%, and that for the lowest energy excitation

Table 3.2: Demographics of 26 study subjects.

Gender	Total #
Male	13
Female	13
BMI (kg/m ²)	Total #
< 25	0
25-30	8
31-40	14
> 40	4
Fibrosis stage	Total #
F 0	5
F 1-2	8
F 3-4	11
N/A	2
Liver capsule depth (mm)	Total #
20-34	13
35-59	13

was only 9%. Figure 3.3 indicates that the rate of successful SWS reconstruction is linearly proportional to the magnitude of the push energy deposition in the liver.

Figure 3.4 shows the normalized peak displacements resulting from ARFI excitations with various push energy levels. For each patient, the peak displacements were normalized to the displacement level at the lowest energy level. The peak displacements increase with increasing transmit excitation energy, as expected.

An ANOVA analysis was performed on the data from the 19 study subjects that produced successful SWS estimates at more than one push energy level. The SWS estimates from each push energy level were not significantly different in 17 of the 19 subjects ($p > 0.05$). The two subjects that yielded different SWS estimates between sequences both had limited successful measurements with outliers at the lower energy levels. Subject 1 produced 2 SWS estimates at $E = 6$ mJ described in Table 3.1, and one of them was 42% higher than the mean of the other estimates. Subject 4 produced only 1 SWS estimate at 6 mJ energy, and it was 62% higher than the mean

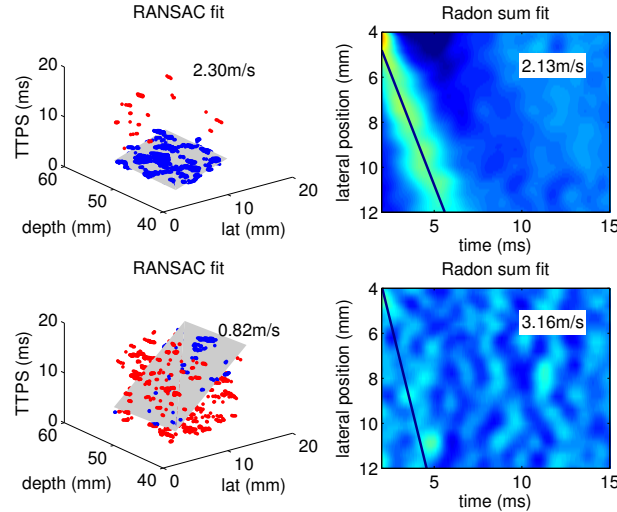


FIGURE 3.2: Example RANSAC and Radon sum SWS reconstructions. In the RANSAC data, the blue points depict inliers of shear wave arrival times, while the red points depict outliers. The gray plane shows the 3D plane that best fits the arrival time profile. In the Radon sum data, which was averaged through depth, the line depicts the best fit that approximates the shear wave trajectory. Each pixel indicates the peak particle velocity ranging from $-5 - 15$ mm/s. The top row shows the RANSAC and Radon sum fit of a successful SWS reconstruction, there were 98% inliers in the RANSAC fit, and the estimates are within 8% of each other. The bottom row shows an unsuccessful SWS reconstruction, where the data is so noisy that no shear wave propagation is evident. There were only 28% inliers in RANSAC fit, and the RANSAC and Radon sum fits were arbitrary, with the SWS estimates differing by 75%.

of the other estimates.

Figure 3.5 further evaluates the energy threshold in the data and includes liver depth information. Figure 3.5 shows the number of study subjects for whom the energy level specified was the smallest energy level that produced a successful SWS estimate, and the color of the bars represents liver capsule depth. Out of the 26 study subjects, 11 had successful SWS estimates at $E = 4.0$ mJ (typical of commercial SWEI), 9 had successful SWS estimates only at elevated push energy levels ($E \geq 6.0$ mJ), and 6 subjects failed to yield any successful SWS reconstructions. Table 3.3 provides details from the 6 failed patients. Deep liver capsules and advanced fibrosis stages are highlighted in bold in Table 3.3. The 6 failed patients had significantly deeper liver capsules than the rest of the study population (45.0 ± 6.3 mm versus

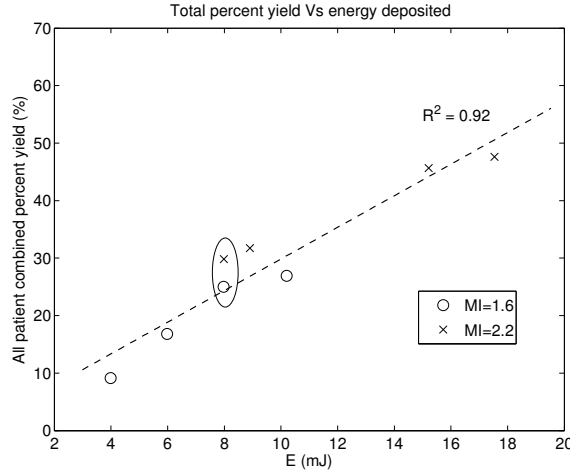


FIGURE 3.3: The combined percent yield across all patients linearly increases with increasing push energy. Of the 8 excitation energy levels used in each patient, four had an MI of 1.6 and four had an MI of 2.2. Generally MI 2.2 excitations have higher push energy than MI 1.6 excitations. There is a pair of high and low MI excitations (circled) that have the same energy level of 8mJ. The dashed line shows the linear fit.

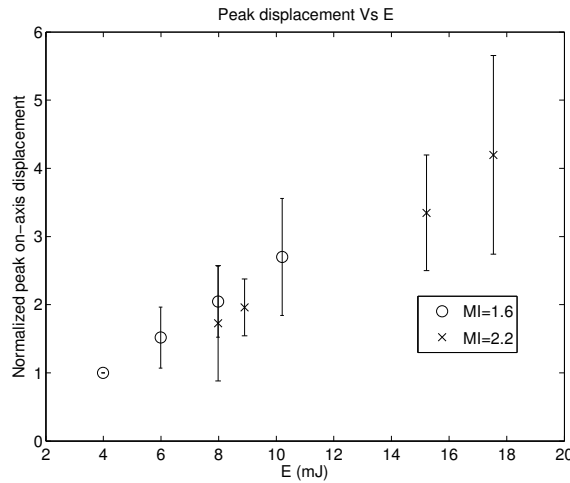


FIGURE 3.4: Normalized peak ARFI displacement versus transmit push energy. The error bars represent variation across the 26 study subjects. For each subject, the displacements were normalized to the amplitude at the lowest push energy level. As expected, peak displacements increase with increasing push energy.

33.5 ± 7.3 mm, $p < 0.001$), and 3 of them had advanced fibrosis.

In order to determine whether patients with deep liver capsules had lower yield, the 26 study subjects were divided into 2 groups: one with shallow liver capsule depths less than 35 mm (light gray bars), and the other with liver capsule depths

Table 3.3: Patient details from the 6 patients without any successful SWS measurements

Number	BMI (kg/m ²)	Liver capsule depth (mm)	Fibrosis stage
1	33	35	3
2	36	40	N/A
3	32	45	4
4	39	50	2
5	55	50	1
6	56	50	4

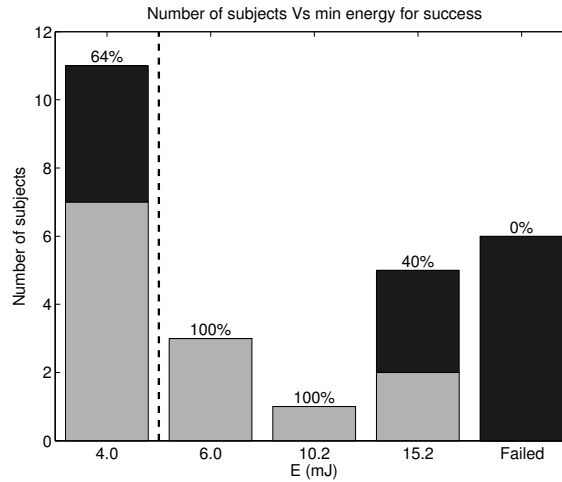


FIGURE 3.5: Number of subjects for whom the energy level was the minimum for SWS measurement success. Light gray bars represent patients with shallow liver capsules (< 35 mm), and black bars represent patients with deeper liver capsules. Percentages indicate the proportion of patients with shallow livers for each energy level. The dashed line separates the energy level typical of commercial SWEI products from the elevated energies used in this study.

greater than 35 mm (black bars). The percentages in Figure 3.5 show the proportion of patients with shallow livers at each energy cut-off (i.e., the ratio of gray to black in each bar). The 5 patients that only succeeded at $E \geq 15.2$ mJ and 6 failed patients had 60% and 100% deep livers, respectively. Figure 3.6 shows the percentage of study subjects that produced at least one SWS estimate at each push energy level for both shallow and deep livers. For patients with shallow livers, 54% succeeded at $E = 4.0$ mJ, and 100% succeeded at $E = 15.2$ mJ. In contrast, 31% of the patients

with deep livers succeeded at $E = 4.0$ mJ, increasing to only 54% at $E = 15.2$ mJ.

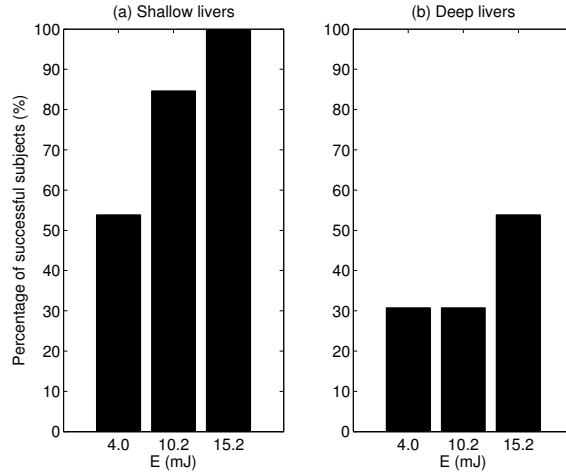


FIGURE 3.6: Percentage of successful subjects versus push energy levels for (a) patients with shallow livers (liver capsule depth < 35 mm), and for (b) patients with deep livers (liver capsule depth ≥ 35 mm).

To further investigate other factors leading to lower yield, Figure 3.7 shows scatter plots of per-patient percent yield out of 64 SWEI measurements (8 repeated measurement \times 8 energy levels) as a function of fibrosis stage, SWS, BMI and liver capsule depth, as well as a scatter plot of liver capsule depth versus BMI. Per-patient percent yield is moderately negatively correlated with fibrosis stage, SWS, and BMI; it is more strongly negatively correlated with liver capsule depth. There is also a strong positive correlation between BMI and liver capsule depth.

In order to assess the possible impact of increased track beam signal strength on yield, we evaluated both the jitter magnitude and harmonic content of tracking beams with different MI values in matched push energy sequences. Figure 3.8 shows the normalized frequency spectra of 10-cycle pressure waveforms at both MIs measured in an attenuating tissue mimicking fluid. The arrows point to the peaks of the second harmonics at 4.4 MHz. There is an 11% increase in the relative magnitude of the second harmonics comparing MI 2.2 to 1.6. Figure 3.8 (c) shows the jitter level for sequences 3 (MI = 1.6) and 5 (MI = 2.2), which each had an energy level of 8

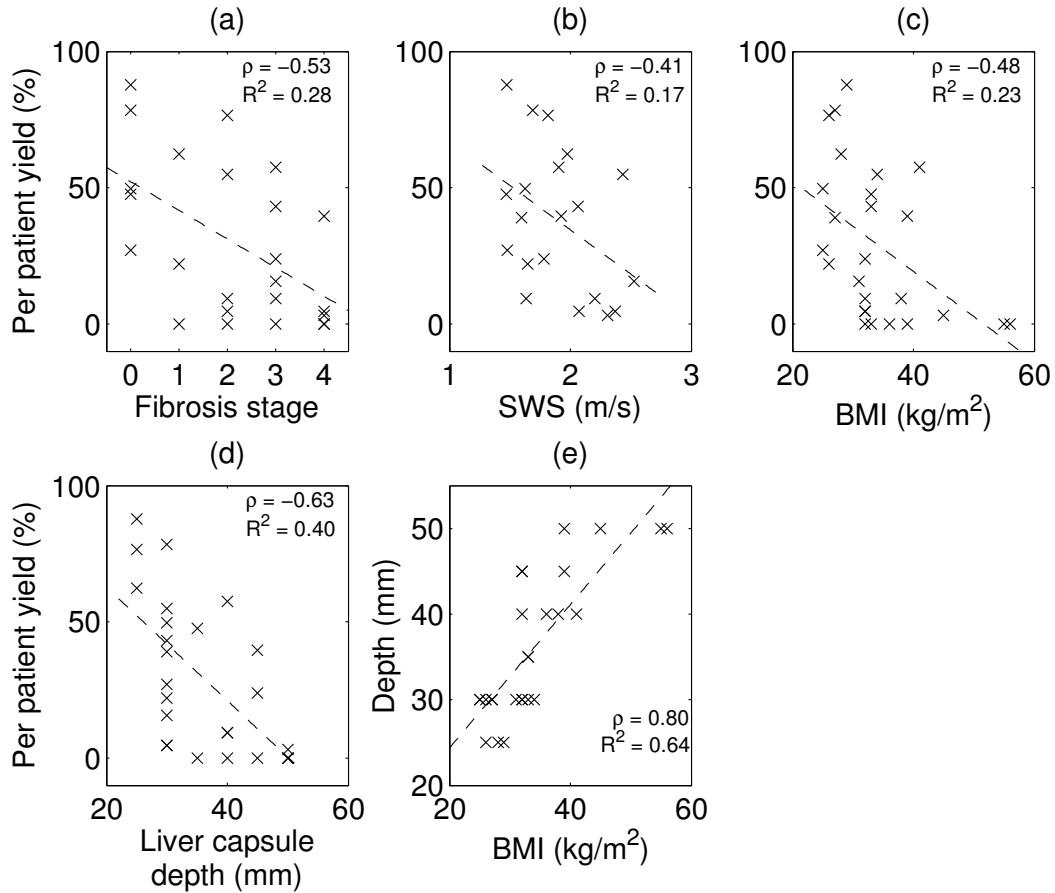


FIGURE 3.7: Per patient percent yield (out of 8 repeated measurements \times 8 energy levels = 64) versus (a) fibrosis stage, (b) SWS, (c) BMI and (d) liver capsule depth respectively. Dashed lines show the linear correlation. (e) shows the correlation between liver capsule depth and BMI. Correlation coefficients ρ and R^2 values are shown for each plot.

mJ (Table 3.1), measured on a CIRS ZerdineTM homogeneous elastic phantom in a location away from the push with zero displacement. The jitter level of Seq 5 is significantly lower than that in Seq 3.

3.5 Discussion

The Mechanical Index (MI) was developed to gauge the likelihood of inertial cavitation associated with diagnostic ultrasound, and its calculation is based upon the assumption of a pre-existing gas bubble in the path of the acoustic beam [5]. There

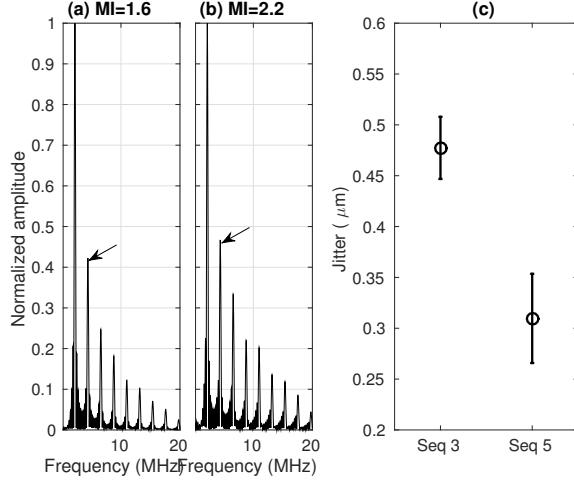


FIGURE 3.8: (a)-(b): Normalized frequency spectra of the push pressure waveforms measured in a solution of condensed milk and water with $\alpha = 0.5$ dB/cm/MHz. The arrows point to the 2nd harmonics at 4.4 MHz. (c): The jitter level for Seq 3 and 5 specified in Table I, measured on a tissue mimicking phantom with a shear modulus of 4kPa. Seq 3 has MI 1.6 and Seq 5 has MI 2.2. The errorbars arise from repeated measurements from 5 independent speckle realizations.

are tissues in the body that naturally harbor gas bubbles, such as lungs and intestines. However, other biological tissues, such as the liver, are generally free of gas bubbles [66, 19]. In such tissues, the requisite amplitude of the ultrasound field for inducing cavitation is relatively high, with one analysis indicating that the likelihood of cavitation using an MI of 4.0 in such tissues is 1 in 10,000,000,000 [19]. In 2012, the American Institute of Ultrasound in Medicine (AIUM) Technical Standards Committee convened a working group of its Output Standards Subcommittee to examine and report on the potential risks and benefits of increasing acoustic output levels under specific clinical imaging scenarios where there is strong expectation of a relatively high benefit-to-risk ratio. Liver imaging is one such scenario, and in this study, we compared SWEI performance using MIs of 1.6 and 2.2 in livers, where inertial cavitation is unlikely to occur due to the lack of pre-existing gas bubbles [66, 19].

From a tissue heating standpoint, these sequences were designed to operate within FDA guidelines, and temperature rises were less than 1°C . The temperature rise

at the transducer’s face for 1 measurement that consisted of all 8 SWEI sequences was measured to be 0.43 °C. This temperature rise was well tolerated by the study subjects. There was no report of patient discomfort due to transducer face heating during the study. The tissue focal temperature rise due to absorption was calculated to be 0.15 °C for each measurement of 8 SWEI sequences, using Equation (3) below [71].

$$\Delta T = \frac{2\alpha I}{c_v} t \quad (3.3)$$

Where ΔT is the focal temperature change, α is the ultrasonic attenuation of the tissue, I is the pulse-average intensity of the acoustic beam, c_v is the specific heat capacity for soft tissue (4.2 W·s/cm³/°C), and t is the pulse duration. No significant, adverse biological effects are expected from such small *in vivo* temperature rises [1].

Figure 3.3 shows that percent yield linearly increases with increasing push energy. Figure 3.4 indicates that higher push energy leads to higher displacement, which provides higher signal level of the shear waves. Therefore, the SNR of the shear wave signal increases with increasing push energy. Based on these findings, we conclude that in the clinical environment, the number of repeated acquisitions necessary to obtain 10 successful SWS estimates would likely decrease with increasing push energy. Further, the total energy deposited into patients would decrease due to the corresponding decrease in the number of repeated acquisitions.

The ANOVA analysis indicated that the SWS estimates from different push energy levels are in agreement. Seventeen out of 19 subjects produced p-value > 0.05, indicating that there is no difference between SWS estimates from the 8 push energy levels in a given subject. Both of the remaining 2 subjects had few successful measurements and outliers for low energy levels. In other words, the SWS estimates obtained in this study from all push energy levels were in agreement when reproducible measurements were obtained (≥ 3 successful SWS estimates out of 8

repeated measures). We thus conclude that SWS is not dependent on pulse duration or MI, at least over the range of values explored herein.

The current FDA guidance specifies that acoustic pressure measurements be made in water, and derated by a factor of $\alpha = 0.3$ dB/cm/MHz to account for frequency-dependent attenuation in tissue. In practice, a wide range of energy levels occur *in vivo* for a given system output due to differences in imaging location and patient-to-patient variability in attenuation. In this study, SWS was measured at a fixed depth (50 mm). However, due to liver capsule depth variability, the acoustic path from the transducer to the SWS imaging window varied significantly across study subjects. For the patient with the shallowest liver capsule, ultrasound waves traveled through 20 mm of subcutaneous tissue and 30 mm of liver tissue to reach the imaging window. On the other hand, for the patient with the deepest liver capsule, ultrasound waves traveled through 45 mm of subcutaneous tissue and only 5 mm of liver. Liver has a typical attenuation of 0.5 dB/cm/MHz, while connective tissue and fat have different attenuations of 0.68 dB/cm/MHz and 0.40 dB/cm/MHz respectively [41]. Other factors such as liver fibrosis, inflammation, and steatosis further alter the *in vivo* energy level. As a result, a wide range of energy levels could occur for the same scanner energy (E) across study subjects, and the current derating approach using a single attenuation coefficient likely overestimates *in situ* acoustic energy levels in many cases. This is the reason displacement amplitudes were normalized in each patient for comparison across patients in Figure 3.4. Given this variability, one might consider using the liver capsule depth as an indicator of when the use of elevated energy might be beneficial, as discussed below.

All 6 subjects that failed at all energy levels had high BMIs and deep liver capsules, and three of these 6 subjects had advanced fibrosis, as shown in Table 3.3. This is consistent with previous studies [101, 81]. High liver capsule depth means that the ultrasound waves have to travel through more intervening tissue to reach the

liver, leading to more pre-liver attenuation and thus smaller applied force. In addition, high BMI is typically associated with increased aberration both of the pushing and tracking pulses, which leads to decreased displacement magnitude and tracking SNR. Advanced fibrosis is associated with higher shear modulus [73], resulting in smaller displacements under the same magnitude of ARFI excitation. As shown in Figure 3.7, yield was moderately correlated with fibrosis stage ($\rho = -0.53$), SWS ($\rho = -0.41$) and BMI ($\rho = -0.48$), and yield was more strongly correlated with liver capsule depth ($\rho = -0.63$).

On the other hand, the elevated energy sequences ($E \geq 6.0$ mJ) successfully obtained SWS estimates from 9 patients who otherwise failed, which comprised 35% the population in this study. Therefore, we conclude that there would be clinical benefit to using elevated output for SWEI measurements in these patients. Since the clinician would not have prior knowledge about a patient’s fibrosis stage or SWS information before SWEI is performed, liver capsule depth (or BMI, which were strongly correlated in these data ($\rho = 0.80$, Figure 3.7e)), could serve as a marker for the need of elevated output. Liver capsule depth describes the distance that the ultrasound wave has to travel to reach the liver, which is a direct indicator of the amount of attenuation and aberration caused by the adipose tissue above the liver. BMI, on the other hand, describes the human body as a whole. The actual distribution of the body weight can vary across the patient population. Figure 3.7 shows that per patient yield is more highly correlated to liver capsule depth ($\rho = -0.63$) than to BMI ($\rho = -0.48$). In this study, liver capsule depth higher than 35 mm was arbitrarily chosen as a marker for a difficult patient who would potentially benefit from SWS measurement with elevated energy levels. In Figure 3.5, 60% of the 5 patients who only produced successful SWS estimates at the highest energy level ($E \geq 15.2$ mJ) and all of the 6 failed patients had deep livers. Figure 3.6 shows that 54% of patients with shallow livers had successful measurements at the energy

level close to commercial systems ($E = 4.0$ mJ), in contrast to only 31% of patients with deep livers at this energy level. We thus conclude that SWS measurements in patients with deep livers are more likely to fail using standard push energy levels, where elevated output could enable successful SWS measurements.

For the pair of SWEI excitations with the same total energy (Seq 3 and 5 in Table 3.1, $E = 8$ mJ), high and low MI sequences were expected to produce similar numbers of successful SWS reconstructions. Figure 3.3 shows that the higher MI excitation had a moderately higher yield (30% total percent yield, 62 successful SWS reconstructions out of 208 measurements) compared to the same energy sequence with lower MI, longer pulses (25% total percent yield, 52 successful SWS reconstructions out of 208 measurements), as determined with a t-test ($p < 0.07$). We hypothesized that this could be explained by nonlinear enhancement of the radiation force impulse in higher MI excitations [91], and/or by the improved tracking signal strength due to increased harmonic generation at the higher MI. If nonlinear force enhancement were present, then we would expect larger displacements in the higher MI sequence; however, no significant differences in displacement amplitude were observed between Seq 3 and 5 (Figure 3.4).

Since the displacement amplitudes were not significantly different between these sequences, the improved yield suggests a difference in tracking performance. To assess the signal quality of the tissue harmonic imaging (THI) tracking pulses, we quantified the jitter level in the data with matching push energies and differing MIs (Seq 3 and 5). In this study, both the push and tracking beams in a given sequence had the same MI due to experimental limitations. For tracking, a higher MI is preferable because it leads to improved harmonic imaging SNR. Figure 3.8 (a)-(b) show the frequency spectra of acoustic pulses measured in attenuating media. These measurements were made in a milk solution rather than water to more closely match the acoustic attenuation of tissue. Seq 5 (MI = 2.2) produced 11% higher

energy in the second harmonics compared to Seq 3 (MI = 1.6). The enhanced harmonic generation associated with the higher excitation voltages used in Seq 5 results in increased ultrasound tracking signal amplitudes and reduced jitter levels. Figure 3.8(c) is consistent with this assessment, in that the jitter level of seq 5 is significantly lower than that of seq 3. We thus conclude that the decreased jitter associated with the MI = 2.2 sequences also contributed to improving the SWS measurement yield. Further studies are required to tease apart the impact of pushing versus tracking signal benefits in SWEI with elevated MI levels.

3.6 Conclusions

This study investigated the clinical benefit of using elevated push energy in hepatic SWEI measurements. Both the ARFI displacement magnitude and the rate of successful SWS reconstruction are shown to increase with increasing push energy level. Elevated push energy would require fewer trials to obtain a specified number of successful SWS estimates and would enable SWS measurement in previously failed patients. The successful SWS estimates from different energy levels are in agreement. The SWS yield was moderately correlated to fibrosis stage, SWS, BMI and was more strongly correlated with liver capsule depth. Liver capsule depth ≥ 35 mm was an indicator of lower yield in this study. Patients with deep liver capsules were more likely to fail at standard push energy levels and thus we conclude that these patients would benefit from elevated output.

4

Quantifying image quality improvement using elevated acoustic output in B-mode harmonic imaging

This chapter has been submitted to the journal of Ultrasound in Medicine & Biology.

Co-authors: Mark Palmeri, Ned Rouze, Gregg Trahey, Clare Haystead, and Kathryn Nightingale.

4.1 Abstract

Tissue harmonic imaging (THI) has been widely used in abdominal imaging due to its significant reduction in acoustic noise compared to fundamental imaging. However, THI can be both signal-to-noise ratio (SNR) and penetration-depth limited during clinical imaging, resulting in decreased diagnostic utility. A logical approach is to increase the source pressure, but the *in situ* pressures used in diagnostic ultrasound have been subject to a *de facto* upper limit based upon the Food and Drug Administration (FDA) guideline for the Mechanical Index ($MI < 1.9$). A recent AIUM report concluded that an MI up to 4.0 could be warranted without concern for increased risk of cavitation in non-fetal tissues without gas bodies, but would only be justified if there were a concurrent improvement in image quality and di-

agnostic utility. This work evaluates image quality differences between normal and elevated acoustic output hepatic harmonic imaging. The results demonstrate that harmonic imaging using elevated acoustic output leads to modest improvements in contrast-to-noise ratio of hypoechoic hepatic vessels (7 – 12%) and increases in imaging penetration depth on the order of 4 – 8 cm per unit MI increase for a given focal depth. Difficult-to-image patients who suffer from poor ultrasound image quality demonstrated larger improvement than easy-to-image subjects.

4.2 Introduction

Ultrasound imaging is one of the most widely used abdominal imaging modalities in the United States, with advantages including its low cost and real-time nature, as well as a lack of ionizing radiation. Abdominal ultrasound is widely used for screening liver diseases [57, 59], and it is the recommended modality for six month screening in patients at risk for hepatocellular carcinoma (HCC) [12, 7]. The major drawback of abdominal ultrasound is poor image quality that is insufficient for diagnosis, which is reported in 25-60% of patients [7, 95, 88, 50], and is often correlated with obesity [85, 51]. In obese patients, poor image quality arises from decreased penetration depth and increased aberration, attenuation and reverberation clutter from the abdominal wall [51, 78].

Tissue harmonic imaging (THI) has become the default imaging mode for most abdominal imaging exams. THI is based upon nonlinear acoustic wave propagation, where images are made from the harmonics generated as the transmitted sound travels through biological tissues. THI is widely reported to be better than fundamental B-mode ultrasound in regard to lesion visibility and diagnostic confidence [93]. Its success in creating higher quality images is attributed to decreased sidelobe energy [16, 17] and decreased reverberation clutter in the abdominal wall [78, 11]. However, second harmonic pressure amplitude is generally 15-20 dB lower than the

corresponding fundamental pressure [29]. Therefore, THI can be both signal-to-noise ratio (SNR) and penetration depth (PD) limited during clinical imaging, resulting in decreased diagnostic utility [85, 51, 25].

A logical approach to improve THI SNR is to increase the source pressure because the second harmonic pressure increases quadratically with source pressure [16]. However, the acoustic output of diagnostic ultrasonic imaging systems in the United States has been subject to a *de facto* upper limit based upon the Food and Drug Administration (FDA) guideline for the Mechanical Index ($MI < 1.9$) [15]. The MI guideline is intended to minimize the potential risk of inertial cavitation induced by diagnostic ultrasound exams. Inertial cavitation is a bubble motion characterized by a large expansion followed by a violent collapse, which can generate damaging shock waves and raise local temperatures as high as 5000 K [21]. The original MI formulation was based on the assumption of pre-existing bubbles in water [5]. The guideline of 1.9 was based on the maximum MI computed for the commercially available products prior to 1976, rather than based upon reported evidence of bioeffects [64]. The MI is commonly further limited by commercial ultrasound vendors when a 20 – 30% safety buffer is applied to reduce the number of production transducers requiring quality assurance testing [103, 4], which results in most current commercial scanners using a maximum MI of 1.6. If bubbles are not present, the pressures (MI) required to induce cavitation are much higher [20]. A recent report from the American Institute of Ultrasound in Medicine (AIUM) concluded that exceeding the recommended maximum MI given in the FDA guidance up to an estimated *in situ* value of 4.0 could be warranted without concern for increased risk of cavitation in non-fetal tissues without gas bodies if there were concurrent improvement in diagnostic utility [64].

The work described in this paper presents a clinical study that evaluated THI data quality for hepatic imaging sequences using MI values typical in commercial ultrasound scanners ($MI = 1.6$) and elevated MI values ($MI \leq 3.3$). We hypothe-

sized that increasing acoustic output would result in higher SNR of the image data, which would increase imaging penetration depth and increase contrast-no-noise ratio of hypoechoic hepatic structures by decreasing the relative signal variance in the structures.

4.3 Methods

Two types of imaging sequences, B-mode and M-mode sequences, were implemented in this study. B-mode data were acquired from hypoechoic vascular structures in subjects' livers and contrast-to-noise ratio (CNR) was calculated to assess the image quality for low and elevated MI matched images. M-mode data were also acquired from homogeneous regions of livers, and the imaging penetration depth (PD) was estimated from M-mode data and evaluated as a function of MI.

4.3.1 Imaging pulse parameters

Pulse-inversion harmonic data were acquired using a modified Siemens S2000 scanner (Siemens Healthcare, Ultrasound Business Unit, Mountain View, CA, USA) with a 4C1 curvilinear array typical for abdominal imaging, and a custom made prototype transducer (PX) for deep abdominal imaging. A total of 4 custom imaging cases were developed and calibrated [4] using the two transducers with various transmit foci to target hepatic structures at different depths. Table 4.1 lists the transmit frequency and focal depths of the 4 imaging cases, as well as the MI values used in this study. Beamformed radio-frequency (RF) data of each transmit-receive event was collected, and pulse inversion harmonic data were created by summing the RF data from two consecutive transmit events with positive and negative leading-edge pulses and filtering the data around harmonic frequencies.

Table 4.1: Transmit frequency, focal depth, and MI configurations

Transducer	Tx frequency	Focal depth	B-mode MI values	M-mode MI values
4C1	1.8 MHz	6 cm	1.6, 2.6	1.6, 2.0, 2.3, 2.6
4C1	1.8 MHz	8 cm	1.6, 2.0	1.6, 1.7, 1.8, 2.0
PX	1.3 MHz	11 cm	1.6, 3.3	1.6, 2.3, 2.9, 3.3
PX	1.3 MHz	14 cm	1.6, 2.5	NA

4.3.2 B-mode sequence and contrast-to-noise ratio (CNR)

B-mode data acquisitions were targeted at hypoechoic vascular structures such as the portal veins in the livers of each subject. For each subject, the liver was scanned with standard MI live B-mode harmonic imaging and image planes containing target hypoechoic structures were identified. The focal depth from Table 4.1 closest to that structure was selected and the receive gain settings were adjusted to obtain the best image quality. Once the image was optimized, the scanner was triggered to acquire three pairs of harmonic images with alternating low MI (1.6) and high MI (2.0-3.3) values using real-time frame rates (≥ 7 frames per second) in a random order. Using real-time frame rate was crucial to minimize the motion between image frames for accurate matched CNR calculations. We aimed to image eight different hypoechoic structures for each subject.

Hypoechoic structures were identified from the acquired images offline after the data acquisition, and contrast-to-noise ratio (CNR) of each structure was calculated from both fundamental and harmonic images. The CNR was calculated using Equation (4.1),

$$\text{CNR} = \frac{|S_i - S_o|}{\sqrt{\sigma_i^2 + \sigma_o^2}}. \quad (4.1)$$

where S_i and S_o are the mean signal magnitudes of the regions inside and outside of

the structures respectively, and σ_i^2 and σ_o^2 are corresponding signal variances. The regions of interest (ROIs) for CNR computation inside and outside the structures were selected to be greater than 20 mm² to provide sufficient area to accurately represent mean brightness. In addition, surrounding margins within the ROI were required to be at least 3 mm to ensure the boundaries of structures were clearly delineated in the images. The CNR results were averaged across each of the three images obtained at low and high MI values respectively for each target. A CNR measurement was rejected when the standard deviation of the CNR across the three matched MI images was greater than 0.1, which indicates that there was significant motion artifact during the acquisition.

For each target, a CNR increase was defined when the difference between the mean CNR going from low to high MI images was positive and larger than the CNR standard deviation between the 3 repeated measurements at either MI. A CNR decrease was defined in a similar way, with a negative CNR difference going from low to high MI images. No change in CNR was defined when the mean CNR difference between the low and high MI images was less than the standard deviation of the 3 measurements at either MI.

4.3.3 M-mode sequence and penetration depth (PD)

M-mode sequences that consisted of repeated firings of ultrasound beams at the same spatial location were performed using a pulse repetition frequency (PRF) \geq 2 kHz. The high PRF was used to minimize motion between the repeated firings. Each beam was repeated 10 times, and each acquisition contained 8 different beam locations. For each subject, the sonographer scanned the liver to target homogeneous liver regions devoid of vessels or other structures using standard B-mode imaging. The scanner was then triggered to acquire M-mode data for 4 MI values between 1.6 and 3.3. The M-mode data were acquired using focal depths of 6 and 8 cm with the

4C1 transducer, and using a focal depth of 11 cm using the PX transducer.

Normalized cross-correlation (NX-corr) [77] was performed between the received harmonic data from repeated firings of each beam using a 1.7 mm kernel with 97% overlap. The correlation coefficient (CC) was averaged across the 10 repeated firings at each spatial location as a function of depth. Imaging penetration depth (PD) was quantified as the depth when the CC dropped below 0.8. For a given transducer and a transmit focal depth, we expect that PD will increase with increasing MI.

4.3.4 *MI measurement*

Acoustic output measurements were conducted according to [4] using a calibrated PVDF membrane hydrophone with a 0.6-mm spot size (Sonic Technologies, Wyndmoor, PA, USA). The pressure was estimated from the recorded voltage waveform using deconvolution based on the frequency dependent magnitude of the sensitivity of the hydrophone [99]. After voltage-to-pressure conversion, the MI was obtained by derating the peak rarefactional pressure by 0.3 dB/cm/MHz at the center frequency of the transmit waveform, and then dividing by the square root of the center frequency.

The maximum MI values as shown in Table 4.1 were dictated by scanner hardware. The commercial ultrasound scanner used in this study was designed to operate at an $MI \leq 1.6$. System nonlinearities could degrade harmonic image quality when the scanner operates at elevated acoustic output levels. The positive and negative leading edge pulses were measured with the hydrophone at the transducer surface at a range of MI values. Lower correlation coefficients were observed between the positive and negative leading edge pulses at higher MI values. A lower correlation coefficient results in imperfect cancellation of the transmitted signals during pulse inversion, which introduces undesirable harmonic content in the received signal and degrades harmonic image quality. We imposed a minimum correlation coefficient

Table 4.2: Subject demographics, 25 subjects in total

Gender	Total #
Male	13
Female	12
BMI (kg/m ²)	Total #
≤ 24.9	8
25.0-29.9	8
30.0-39.9	6
≥ 40.0	3
Image quality	Total #
1 (easy)	9
2 (medium)	9
3 (difficult)	7

magnitude threshold of 0.98 to maintain high levels of cancellation. This correlation coefficient threshold dictated the maximum MI for each sequence used in this study.

4.3.5 *Clinical study design and population*

Twelve patients scheduled for general abdominal ultrasound exams at Duke University Medical Center and thirteen healthy volunteers were enrolled for this study. This clinical study was approved by the institutional review board (IRB) at Duke University and Duke University Medical Center, and each study subject provided written informed consent prior to enrollment. The Body Mass Index (BMI) of each subject was recorded. All data acquisition was performed subcostally. Study subjects were asked to stop breathing during each data acquisition, which lasted approximately 5 seconds for B-mode sequences and 8-10 seconds for M-mode sequences. The study subject was instructed to resume breathing after each acquisition. The B-mode image quality of each subject was subjectively scored on a 1 – 3 scale by the study team radiologist (1 - easy, 2 - medium, 3 - difficult). Table 5.2 summarizes the subject demographics.

4.4 Results

4.4.1 Mechanical Index (MI)

The MI was measured for a range of scanner excitation voltages at each focal depth. Figure 4.1 shows example pressure waveforms measured at a focal depth of 6 cm using the 4C1 transducer. Figure 4.1 (a) and (b) plot the pressure waveforms corresponding to MI values of 1.4 and 2.8. As is typical in water measurements, both waveforms appear non-linear with the peak positive pressure significantly higher than the peak negative pressure. The corresponding MI values were calculated from peak negative pressures using Equation 2.1.

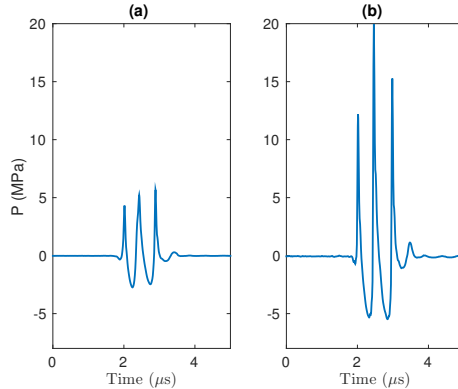


FIGURE 4.1: Hydrophone measurement results from the 4C1 transducer with a lateral focus at 6 cm. (a) Pressure waveform corresponding to an MI of 1.4. (b) Pressure waveform corresponding to an MI of 2.8.

4.4.2 Contrast-to-noise ratio (CNR)

Hepatic hypoechoic structures were identified from each B-mode image after data acquisition, and their CNR was computed. Given the rejection criteria described in Section 4.3.2, there were 188 hypoechoic structures identified in total from the B-mode images of the 25 subjects.

The two images in the top row of Figure 4.2 show an example pair of hepatic harmonic images of an average weight volunteer (BMI = 20.9 kg/m²). The arrows in

the images point to 3 hypoechoic vessels in which the CNR was computed. The CNR values of the 3 vessels at the 2 MI values are plotted in the bottom panel of Figure 4.2. The variability among the 3 pairs of the measurements at each MI is reflected in the error-bars. The vessels had CNR increases of 7% (red), 12% (cyan), and 20% (pink) going from low to high MI imaging. Figure 4.3 shows a pair of hepatic harmonic images from an overweight patient (BMI = 26.0 kg/m²) who consistently exhibited significant CNR increase (> 30%) going from low to high MI imaging. The CNR of the highlighted structure increased by 38%, and the boundary of the structure is more clearly delineated in the high MI image on the right.

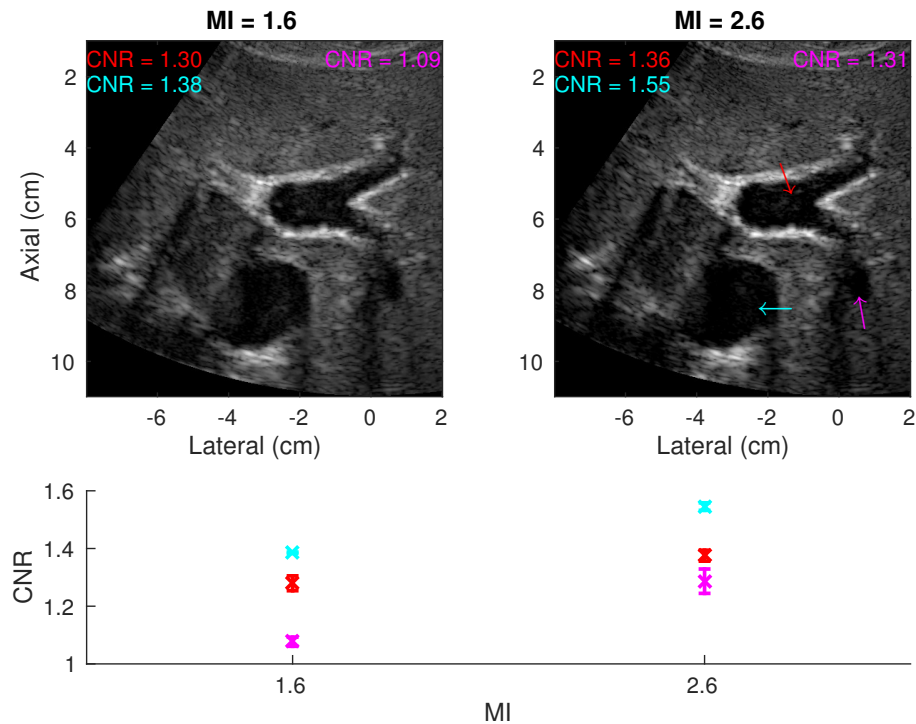


FIGURE 4.2: Top: Matched THI images using MI values of 1.6 (left) and 2.6 (right) in an easy-to-image (Category 1) volunteer with a BMI of 20.9 kg/m². The arrows indicate structures in which CNR was computed. Both images are shown with a dynamic range of 60 dB. Bottom: CNR versus MI for each structure. The error-bars reflect the variability of CNR among the 3 pairs of measurements at each MI.

Figure 4.4 shows the number of structures that exhibited a CNR increase, no change, or decrease going from low to high MI B-mode imaging across all focal

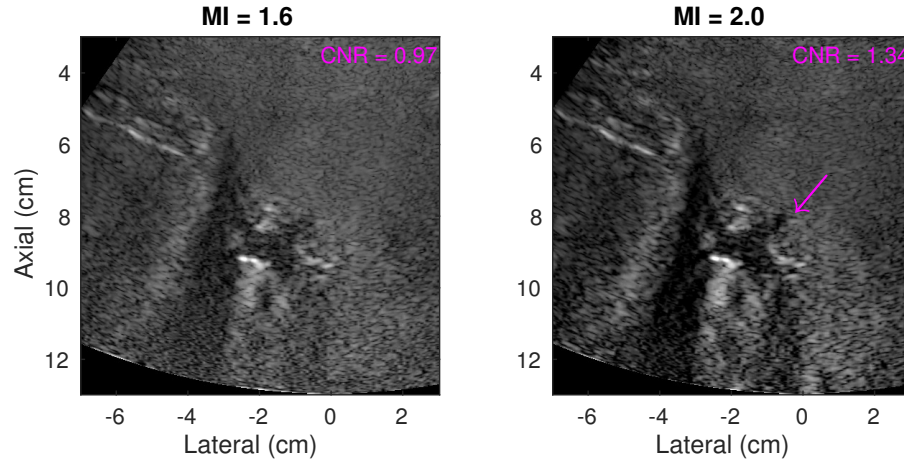


FIGURE 4.3: Matched THI images using MI values of 1.6 (left) and 2.0 (right) in a medium image quality (Category 2) patient with a BMI of 26.0 kg/m². The arrow indicates the structure in which CNR was computed. Both images are shown with a dynamic range of 60 dB.

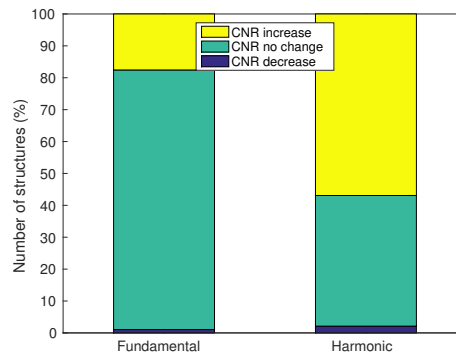


FIGURE 4.4: The number of hepatic hypoechoic structures that exhibited a CNR increase between matched low and high MI B-mode imaging across all 25 subjects. Out of the 188 identified structures, 57% of the structures had a CNR increase in harmonic images, whereas only 18% of the structures had a CNR increase in fundamental imaging.

depths and all study subjects in both fundamental and harmonic imaging modes. Out of the 188 identified structures, 57% exhibited a CNR increase in harmonic images, while only 18% exhibited a CNR increase in fundamental images.

The CNR results of harmonic images were then normalized to the CNR values at an MI of 1.6 to estimate percent CNR increase. Figure 4.5 shows percent CNR increase with respect to image quality evaluated by the radiologist. The mean CNR increase was positive for all levels of image quality with median values of 4.2% 7.2%

and 7.6% for easy, medium and difficult-to-image subjects. Using a Wilcoxon rank sum test, the CNR increase in images with quality level 1 is significantly lower than the CNR increase for image quality levels 2 and 3 ($P \leq 0.005$).

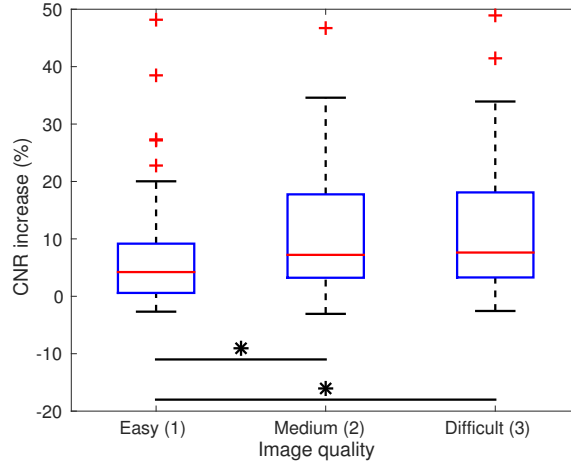


FIGURE 4.5: Percent CNR change as a function of subjective assessment of overall image quality. The mean CNR change is positive for all levels of image quality. The CNR increase for image quality level 1 is significantly lower than the CNR increase for image quality level 2 and 3 ($P \leq 0.005$).

Figure 4.6 shows scatter plots of the percent CNR increase from all subjects with respect to focal depth between low and high MI imaging. The focal depth was generally close to the depth of the hypoechoic structures. There is no significant trend between focal depth and CNR increase ($\rho = 0.13$, $P > 0.05$).

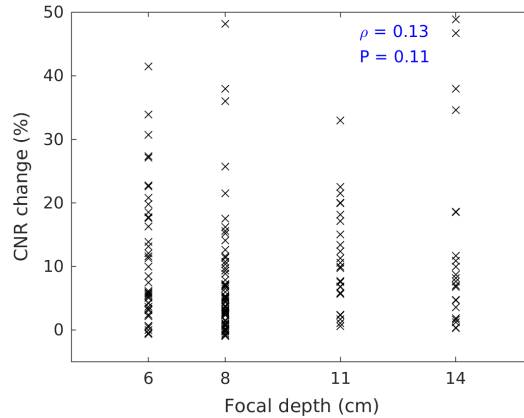


FIGURE 4.6: Percent CNR change versus focal depth

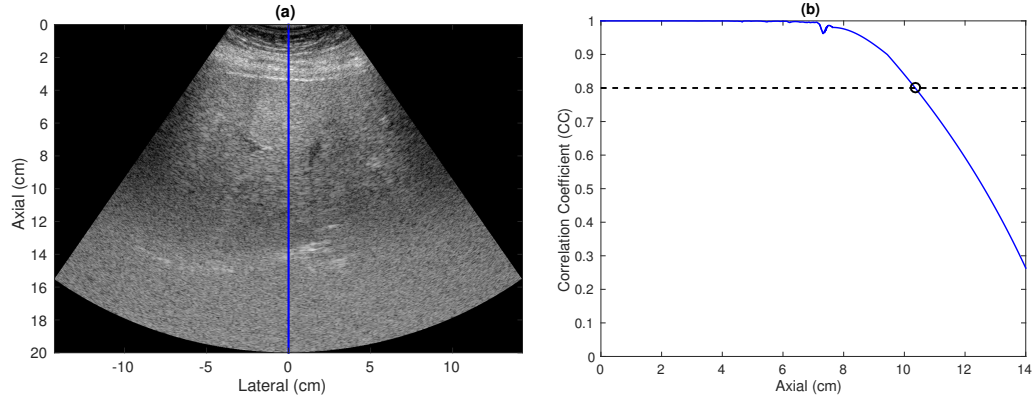


FIGURE 4.7: (a) An example harmonic image using a focal depth of 6 cm and an MI value of 1.6 from an overweight subject ($\text{BMI} = 25.7 \text{ kg/m}^2$). The image is shown with a dynamic range of 60 dB. CC was calculated from the M-mode data of the center beam of the image as highlighted by the blue line. (b) CC as a function of depth. Using a CC cut-off of 0.8, the penetration depth of this image is determined to be 10.4 cm.

4.4.3 Penetration depth (PD)

M-mode data was obtained from 23 of 25 subjects. The 2 failed subjects had trouble holding their breath during the M-mode data acquisition which took 8 – 10 seconds. Figure 4.7 (a) shows an example harmonic image using a focal depth of 6 cm and an MI value of 1.6 from an overweight subject ($\text{BMI} = 25.7 \text{ kg/m}^2$). The deepest 50% of this image is dominated by electronic noise and a lack of signal. Correlation coefficients were calculated using 1.7 mm kernels along the center beam of the image (blue line), which is one of the 8 different spatial locations where PD was evaluated. Figure 4.7 (b) plots the corresponding correlation coefficient results over depth. The correlation coefficients were close to 1.0 for shallow depths < 7 cm, and decreased with increasing depth as the harmonic signal amplitude dropped due to attenuation and the electronic noise became more apparent. Using an arbitrarily selected correlation coefficient cut-off of 0.8 to quantify penetration depth, the penetration depth for this case is 10.4 cm.

Imaging penetration depth (PD) was estimated from the M-mode data for all focal

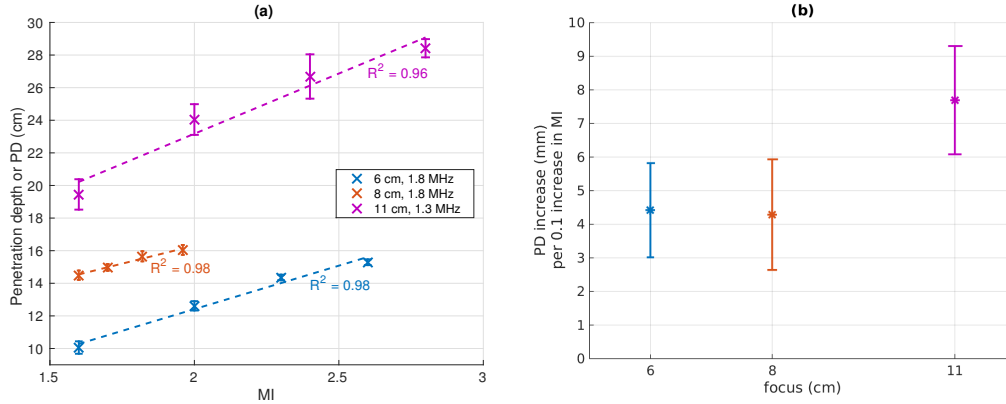


FIGURE 4.8: (a) Penetration depth (PD) as a function of MI computed in an overweight patient (BMI of 25.7 kg/m²). An increase in MI results in an increase in penetration depth for all focal depths. The dashed lines represent the linear fit between MI and mean PD. The error-bars reflect the standard deviation from 8 different spatial locations. (b) Slope of the linear fit between MI and PD as shown in (a) combining data from all the study subjects ($R^2 \geq 0.95$) as a function of focal depth. The error-bars represent inter-subject variability.

depths from the 23 subjects. Figure 4.8 (a) plots PD as a function of MI at different focal depths in the same subject as in Figure 4.7. The error-bars reflect the standard deviations of PD computed from 8 different spatial locations. PD is always higher than the focal depth, and increases with increasing MI. The mean PD follows a linear relationship with MI as shown by the dashed lines in Figure 4.8 (a). Similar trends between MI and mean PD were observed in the data from all subjects. Figure 4.8 (b) shows the slope of the increase in PD with respect to MI increase combining data from all 23 subjects. The error-bars represent inter-subject variability. The results indicate that PD increases between 4 mm and 8 mm per MI increase of 0.1 depending upon transmit focal depth, frequency and focal configuration.

4.5 Discussion

This paper evaluates the *in vivo* image quality improvement when using elevated acoustic output in hepatic harmonic B-mode imaging. The Mechanical Index (MI) was originally developed to gauge the likelihood of inertial cavitation associated with

diagnostic ultrasound [5]. The FDA guideline of $MI < 1.9$ for diagnostic ultrasound was derived from historic values, rather than being linked to scientific evidence of bioeffects. In biological tissues that are generally free of gas bubbles such as healthy livers, the cavitation pressure threshold is relatively high, with one theoretical analysis concluding that the likelihood of cavitation using an MI of 4.0 in such tissues is 1 in 1^{10} [19]. The Technical Standards Committee of the AIUM has formed a subcommittee to examine the benefits and risks of elevated acoustic output under clinical imaging scenarios where there is potentially high benefit-to-risk ratio [64]. Liver imaging is one such scenario, and this study evaluated the image quality of hepatic harmonic imaging using an MI up to 3.3.

This study evaluated the impact of using elevated acoustic output at a limited range of focal depths (6, 8, 11, and 14 cm). We were unable to achieve an $MI > 1.9$ using deeper focal depths given the finite transducer aperture and limited scanner hardware. Water-based pressure measurements are subject to a maximum pressure amplitude (saturation pressure) for a given focal configuration due to pre-focal saturation losses in water, which results in a maximum MI that can be measured for each focal depth [32]. The saturation pressure increases with increasing aperture size, and decreases with increasing imaging focal depth and frequency. For typical curvilinear array transducers such as the 4C1 transducer for abdominal imaging, it is difficult to achieve an $MI > 1.9$ for focal depths greater than 10 cm.

Elevated acoustic output results in improved CNR for a larger number of structures in harmonic imaging than in fundamental imaging as shown in Figure 4.4. Out of the 188 identified structures, 57% of the structures had a CNR increase in harmonic images, while only 18% of the structures had a CNR increase in fundamental images with increased MI. This is likely because harmonic imaging suffers from a lower SNR than fundamental imaging [11]. Second harmonic pressure increases with the square of source pressure, while fundamental pressure increases linearly with

source pressure [16]. Therefore, an MI increase leads to a quadratic increase in harmonic signal compared to a linear increase at the fundamental signal, resulting in a higher CNR increase in harmonic images.

As shown in Figure 4.6, a CNR increase with respect to MI was observed at all focal depths, and there was no correlation between focal depth and CNR increase. The CNR increases observed in this study were fairly modest (mean values of 7 – 12%), although, there was one subject in whom CNR increases consistently exceeded 30% with increased MI (going from 1.6 to 2.0) as shown in Figure 4.3.

Figure 4.5 examines the percent CNR increase with respect to image quality as subjectively assessed by the radiologist. The mean CNR increase is positive for all levels of image quality, suggesting that elevated acoustic output could lead to higher lesion visibility in subjects regardless of body habitus. On the other hand, the CNR improvement is significantly higher in medium- and difficult-to-image subjects than in easy-to-image subjects, indicating that difficult-to-image subjects could preferably benefit from using elevated acoustic output imaging.

Figure 4.8 indicates that increasing MI results in an increase in imaging penetration depth for a given focal depth in THI images. An MI increase leads to higher harmonic signal amplitude, which in turn increases the SNR of the harmonic image and the imaging penetration depth. In cases when the radiologist struggles to see the anatomy deep in an ultrasound image for a given focal configuration, we expect that increasing MI would increase the imaging penetration depth and enable the image to cover a larger axial extent, as shown in Figure 4.9. On the other hand, this study investigated a limited range of focal depths: 6 cm, 8 cm, and 11 cm, and PD was compared for matched focal depths. We did not compare, for example, high MI focused at 11 cm with lower MI focused at 24 cm. Future work will be directed to explore imaging penetration depth with varying focal depths to evaluate the optimal focal configuration and acoustic output level for deep abdominal imaging.

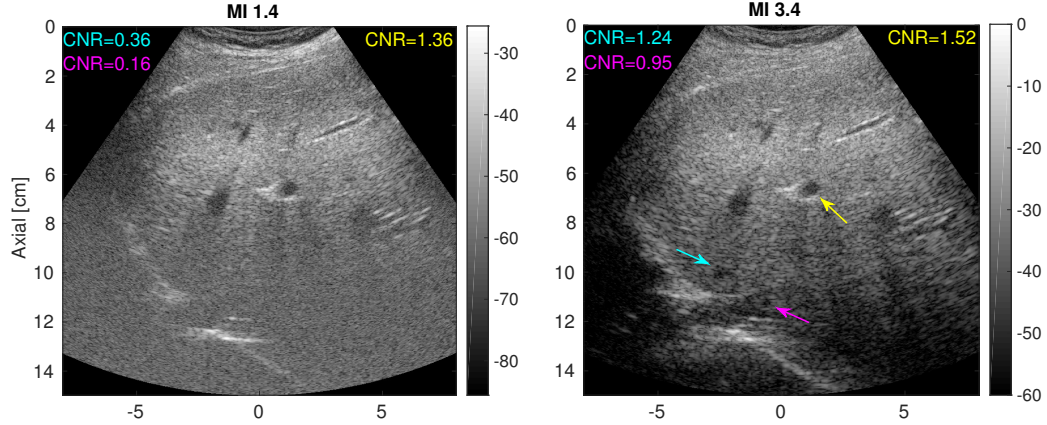


FIGURE 4.9: Matched THI images using typical an MI value (MI=1.4, left) and an elevated MI value (MI = 3.4, right) focusing at 5 cm in an obese volunteer (BMI = 30.4 kg/m²) with a fatty liver. The image intensities are shown in dB. The arrows point to vessels in which CNR was computed. The cyan and magenta arrows in the right image indicate structures deep to the focus that are only visible in the elevated MI configuration.

A limitation of this study is that targets were identified while scanning with the lower MI sequence. Each subject was first scanned with conventional THI to identify targets in the liver. After the target was located, the scanner was then triggered into data acquisition using low and high MI values. This meant that all structures were visualized at both low and high MI, and in general only modest increases in CNR were observed in these structures. In one subject, we observed some lower contrast structures deep to the focus at higher MI that were not visualized at the lower MI. Figure 4.9 shows a pair of harmonic hepatic images using MI values of 1.4 and 3.4 acquired in an obese volunteer (BMI = 30.4 kg/m²) with a fatty liver focused at 5 cm. The cyan and purple arrows in the right panel highlight structures that were not seen in the low MI imaging. In this case, elevated acoustic output imaging increased the SNR of the harmonic signal at depths beyond the focus, and enabled visualization of low-contrast structures that were not apparent at the lower MI.

Another limitation of this study was the use of only 2 MI values for each focal depth in the B-mode sequences and CNR computation. This limits the ability to

draw conclusions about MI thresholds and minimum CNR increases. This will be the focus of future work.

In addition to the FDA guideline on the Mechanical Index that minimizes the risk of non-thermal bioeffects, diagnostic ultrasound systems are also subject to thermal safety limits such as the spatial peak temporal average intensity (I_{SPTA}) and transducer face heating. I_{SPTA} is related to expected thermal bioeffects and is limited to 720 mW/cm^2 in non-fetal tissue [15]. The temperature rise at the transducer surface is limited to 27°C when transmitting into still air and 10°C when the probe is in contact with a phantom during scanning [49]. In this initial study, we adopted a very conservative scanning protocol which had low duty cycle ($< 1\%$) during high MI data acquisition to minimize temperature increase. There has been no report of patient discomfort due to transducer face heating during the study. Future work will involve developing high MI scanning sequences in order to assess detectability differences of low contrast hepatic lesions.

4.6 Conclusions

This study investigated image quality improvement using elevated acoustic output in hepatic B-mode harmonic imaging. Custom B-mode and M-mode sequences were developed with fixed focal configurations, and Contrast-to-noise ratio (CNR) as well as imaging penetration depth (PD) were computed to assess image quality. We observed modest increases in CNR in the majority of hepatic hypoechoic vascular structures using harmonic imaging with elevated acoustic output. The CNR improvement with elevated MI was apparent in all subjects, and was higher in medium and difficult-to-image subjects. We also observed that harmonic imaging PD increased linearly with increasing MI for all focal depths. The results indicate that using elevated acoustic output exceeding the current FDA guideline of MI 1.9 moderately improves the image quality of B-mode hepatic harmonic imaging in terms of increasing vessel CNR

and axial imaging depth.

5

Evaluating the benefit of elevated Mechanical Index (MI) harmonic motion estimation in ultrasonic shear wave elasticity imaging (SWEI)

This chapter has been submitted to the journal of Ultrasound in Medicine & Biology.

Co-authors: Mark Palmeri, Ned Rouze, Clare Haystead, and Kathryn Nightingale.

5.1 Abstract

Harmonic imaging techniques have been applied in ultrasonic elasticity imaging to obtain higher quality tissue motion tracking data. However, harmonic tracking can be signal-to-noise ratio (SNR) and penetration depth (PD) limited during clinical imaging, resulting in decreased yield of successful shear wave speed (SWS) measurements. A logical approach is to increase the source pressure, but the *in situ* pressures used in diagnostic ultrasound have been subject to a *de facto* upper limit based upon the Food and Drug Administration (FDA) guideline for the Mechanical Index ($MI < 1.9$). A recent AIUM report concluded that an MI up to 4.0 could be warranted without concern for increased risk of cavitation in non-fetal tissues without gas bodies if there were a concurrent clinical benefit. This work evaluates

the impact of using elevated Mechanical Index (MI) in harmonic motion tracking for hepatic shear wave elasticity imaging (SWEI). The studies demonstrate that high MI harmonic tracking increased SWS estimation yield by 27% and 37% at focal depths of 5 cm and 9 cm respectively, with larger yield increase in more difficult-to-image patients. High MI tracking improved harmonic tracking data quality by increasing the signal-to-noise ratio (SNR) and decreasing jitter of the tissue motion data. We conclude that there is clinical benefit of using elevated MI in shear wave tracking particularly in difficult-to-image patients.

5.2 Introduction

Ultrasonic elasticity imaging methods have been developed over the last 2 decades to estimate tissue stiffness, which is often associated with underlying pathological conditions [87]. An increase in tissue stiffness can be caused by the presence of fibrotic tissue as occurs in liver cirrhosis, or by an increase of tissue cellular density as typically occurs with cancer. A number of ultrasonic elasticity imaging techniques have been proposed including acoustic radiation force impulse (ARFI) imaging [63] and shear wave elasticity imaging (SWEI) [84]. These methods use long-duration focused ultrasound beams to induce tissue motion and standard ultrasound imaging techniques to track the resulting tissue motion. ARFI imaging measures on-axis tissue displacement to determine relative differences in tissue stiffness. SWEI monitors tissue motion at locations offset from the ARFI excitation to determine the propagation speed of the induced shear wave, which is related to the shear modulus of the material. The conventional SWEI method uses multiple track beams to track the shear wave generated from a single ARFI excitation, with the shear wave speed (SWS) reflecting the shear modulus between the track beams used in the estimation. This method is referred to as multiple track location SWEI (MTL-SWEI) [46]. Recently, a different beam configuration was proposed that uses multiple laterally offset

push beams and a single track beam (STL-SWEI) [56, 46]. The SWS estimated in this method reflects the tissue properties between the push beams. STL-SWEI is less susceptible to speckle bias [56], which is a source of error that leads to uncertainties in the tracking beam position.

Tissue harmonic imaging (THI) has been widely used in diagnostic ultrasound since the late 1990s because it improves image quality compared to fundamental B-mode imaging mode. THI relies on nonlinear acoustic wave propagation, which generates harmonic signals as the transmitted sound wave travels through biological tissues. An ultrasound harmonic image is created from the harmonic signal instead of the transmitted fundamental signal. THI is reported to create higher quality images compared to fundamental imaging in regard to lesion visibility and diagnostic confidence [93], due to decreased sidelobe energy [16, 17] and decreased reverberation clutter [78, 11]. However, second harmonic pressure amplitude is generally 10-20 dB lower than the corresponding fundamental pressure [29]. Therefore, THI can be both signal-to-noise ratio (SNR) and penetration depth (PD) limited during clinical imaging, resulting in decreased diagnostic utility [85, 51, 25].

THI techniques have been applied in tissue motion tracking in ultrasonic elasticity imaging methods to obtain higher quality tracking data utilizing the benefits of *in vivo* harmonic imaging [30, 3]. Harmonic tracking reduces the reverberation clutter and bias in tissue displacement estimates. On the other hand, harmonic tracking has the challenge of low SNR and low penetration depth similar to B-mode THI. The low SNR in harmonic tracking can lead to higher jitter, i.e., the magnitude of the uncertainties in ultrasonic displacement estimation. Based upon the Cramér-Rao lower bound (CRLB) (Equation 2.22) [96], due to the limited harmonic signal amplitude, CC and SNR can be lower for harmonic tracking, which can result in higher jitter. Herein, we test the hypothesis that using an elevated Mechanical Index (MI) in harmonic tracking will increase the SNR of the harmonic signal, therefore

reducing jitter magnitude and increasing the measurement success of ARFI and SWEI imaging.

The acoustic output of diagnostic ultrasonic imaging systems in the United States has been subject to a de facto upper limit based upon the Food and Drug Administration (FDA) guideline for the Mechanical Index ($MI < 1.9$) [15]. The MI guideline is intended to minimize the potential risk of inertial cavitation induced by diagnostic ultrasound exams. The MI is commonly further limited by commercial ultrasound vendors when a 20 – 30% safety buffer is applied to reduce the number of production transducers requiring quality assurance testing [103, 4], which results in most current commercial scanners using a maximum MI between 1.3 and 1.6. However, the FDA MI guideline for diagnostic ultrasound systems was based on substantial equivalence with commercial product in the market prior to 1976, rather than being linked to scientific evidence of bioeffects. A recent report from the American Institute of Ultrasound in Medicine (AIUM) concluded that exceeding the recommended maximum MI given in the FDA guidance up to an estimated *in situ* value of 4.0 could be warranted without concern for increased risk of cavitation in non-fetal tissues without gas bodies [64].

Our group has previously investigated the benefit of using elevated acoustic output in the ARFI excitation in shear wave imaging [26]. A clinical study was performed to evaluate hepatic SWEI measurement success as a function of push pulse energy using 2 MI values (1.6 and 2.2) over a range of pulse durations. The results indicated that the rate of successful SWS estimation is linearly proportional to the magnitude of the push energy. A higher push energy results in higher tissue displacement, which in turn leads to higher SNR of the tracking data. On the other hand, in our experience, the success of ultrasonic shear wave imaging largely depends on the ability to accurately track tissue motion. The impact of using elevated MIs in tissue motion tracking was not evaluated due to hardware limitations in the previous study.

The work described in this paper examines the use of elevated MIs in harmonic motion estimation in SWEI. This study evaluates SWS estimation yield and jitter amplitude for SWEI sequences using identical push beams, and either a typical MI value of 1.6 or an elevated MI value of 2.8 for motion tracking.

5.3 Methods

5.3.1 Data acquisition sequence and calibration

Group SWS was measured with a modified Siemens Acuson S2000 ultrasound scanner (Siemens Healthcare, Ultrasound Business Unit, Mountain View, CA, USA). Two transducers were used in this study, a 4C1 curvilinear array and a custom made prototype transducer (PX) for deep abdominal imaging. The push and track pulses for each SWEI sequence had concurrent focal depths, which were 5 cm for the 4C1 transducer and 9 cm for the PX. An STL-SWEI configuration was used for all sequences, with a single track beam located along the center axis of the transducer (0 mm), and eight evenly spaced push beams covering a lateral range of 1.0 – 10.2 mm [56, 46]. Table 5.1 lists the track beam configurations.

Table 5.1: Track beam configurations

Transducer	Focal depth	Tx frequency	PRF	MI values
4C1	5 cm	1.8 MHz	5.0 kHz	1.6 and 2.8
PX	9 cm	1.3 MHz	3.4 kHz	1.6 and 2.8

Each measurement consisted of two sequentially acquired SWEI sequences with identical push configurations and two track configurations. One sequence had a track MI of 1.6 (typically used in commercial ultrasound scanner), and the other had an elevated MI of 2.8. Fully sampled pulse inversion harmonic tracking followed by a bandpass filter around the harmonic frequency was used for all sequences [30]. The push configurations of the 4C1 transducer were the same as in a clinical study

previously conducted by our group [73], which used 400-cycle push pulses at 2.2 MHz. The PX used 600-cycle push pulses at 1.5 MHz.

Acoustic output measurements were conducted according to [4] using a calibrated PVDF membrane hydrophone with a 0.6-mm spot size (Sonic Technologies, Wyndmoor, PA, USA). The pressure was estimated from the recorded voltage waveform using deconvolution based on the frequency dependent magnitude of the sensitivity of the hydrophone [99]. After voltage-to-pressure conversion, the MI was computed using Equation (2.1).

5.3.2 SWS calculation and SWS yield

Beamformed radio-frequency (RF) data were obtained from each acquisition, and the data from low and high MI tracking were processed identically to generate SWS estimates. Tissue displacement was estimated using normalized cross-correlation [77]. A bandpass filter (BPF) with cut-off frequencies at 50 Hz and 1000 Hz was applied to the tissue displacement data to reduce motion artifact and displacement jitter [27]. SWS was reconstructed using 2 algorithms: the random sample consensus (RANSAC) [98] algorithm applied to arrival times of the peak tissue displacements and the radon sum [83] algorithm applied to displacement data averaged over the depth of field of the push beam (16 – 20 mm depending on push frequency). A SWS measurement was considered unsuccessful and was rejected if there were less than 50% inliers in the RANSAC algorithm, and/or when the SWS estimates from the two algorithms differed by more than 15% [26].

5.3.3 Data quality metrics: correlation coefficient (CC), displacement jitter, and maximum displacement

The correlation coefficient (CC), displacement jitter and maximum displacement were used as metrics of the tracking data quality in this study. Each metric was compared between low and high MI tracking sequences using Wilcoxon rank sum

tests. The CC is related to the signal-to-noise ratio (SNR) of the tracking data using Equation (5.1), as adapted from Equation (20) in [39]. The jitter represents the random errors in ultrasonic displacement estimation. A higher CC and lower jitter indicate higher tracking data quality. The correlation coefficient and displacement jitter were estimated from spatial locations away from the ARFI excitation and from temporal windows before the shear wave arrived where no motion is expected. The SNR of the tracking data was computed from the average CC for each MI configuration at both focal depths using Equation (5.1). The jitter was calculated as the standard deviation of the displacement data when no shear wave was present. The frequency content of shear waves generated in human livers using a curvilinear array is typically less than 500 Hz [69]. Because filtering is often used to reduce jitter, the jitter was computed for 3 different signal processing scenarios: no motion filter, BPF 50 – 1000 Hz (typically used in SWEI), and an aggressive motion filter of BPF 50 – 500 Hz.

$$\text{SNR} = \sqrt{\frac{CC}{1 - CC}} \quad (5.1)$$

Maximum displacement can be used to gauge the level of reverberation clutter present in the tracking data because a high level of stationary clutter leads to underestimation of the tracked displacement [77]. It was calculated at each MI from the average displacement within the depth of the field at the closest recorded beam to ARFI excitation, which was 1.0 mm and 1.2 mm at focal depths of 5 cm and 9 cm respectively.

5.3.4 *Clinical study design and population*

Twenty-five study subjects in total were recruited in this study, including 12 patients scheduled for abdominal ultrasound exams at Duke University Medical center and

Table 5.2: Subject demographics, 25 subjects in total

Gender	Total #
Male	13
Female	12
BMI (kg/m ²)	Total #
≤ 24.9	8
25.0-29.9	8
30.0-39.9	6
≥ 40.0	3
Image quality	Total #
1 (easy)	9
2 (medium)	9
3 (difficult)	7

13 healthy volunteers. This clinical study was approved by the institutional review board at Duke University, and each study subject provided written informed consent prior to enrollment. The Body Mass Index (BMI) of each subject was recorded. All data acquisitions were performed at the subcostal location. Commercial B-mode imaging was used to scan each subject’s liver and identify a homogeneous liver region devoid of vessels or other structures. The study subject was then asked to stop breathing during data acquisition, which lasted approximately 6 seconds and consisted of a pair of STL-SWEI measurements using low and high MI tracking. The study subject was instructed to resume breathing after each measurement. Six repeated measurements were performed for each subject. The B-mode image quality of each subject was subjectively evaluated by the sonographer, and separated into scores 1-3 (1 - easy, 2 - medium, 3 - difficult). Table 5.2 summarizes the subject demographics.

5.4 Results

Figure 5.1 shows the total percentage yield of successful SWS measurements for low and high MI tracking across all subjects. The number of successful SWS estimations was summed over six repeated measurements from each study subject to determine the total yield for each sequence. The percent yield was then calculated by dividing the total yield by the total number of measurements (6 repeated measurements \times 25 study subjects = 150). Going from low to high MI tracking, the percent yield increased from 43.3% to 70.7% focused at 5 cm, and from 16.0% to 52.7% focused at 9 cm.

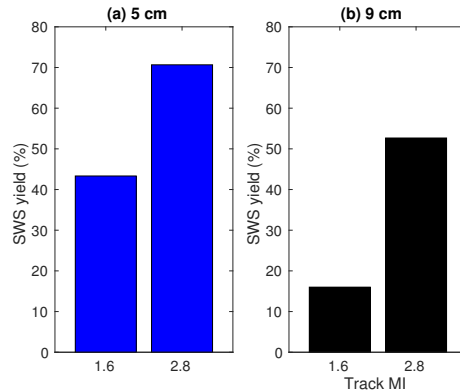


FIGURE 5.1: Percent yield of successful SWS measurements across all study subjects for low and high MI tracking. The title of each sub-figure shows the focal depth. Going from low to high MI tracking, the percent yield increased from 43.3% to 70.7% focused at 5 cm, and from 16.0% to 52.7% focused at 9 cm.

Figure 5.2 shows two example pairs of the shear wave trajectories using low and high MI tracking focused at 5 cm from (a) an easy-to-image volunteer and (b) a difficult-to-image patient. In the easy volunteer, both low and high MI tracking yielded successful estimates and resulted in similar SWS values (Figure 5.2a). Low MI tracking failed to produce a successful SWS estimate in the difficult patient (Figure 5.2b). The high MI tracking in both cases visually has a more well defined trajectory of the propagating shear wave, suggesting that high MI tracking reduces

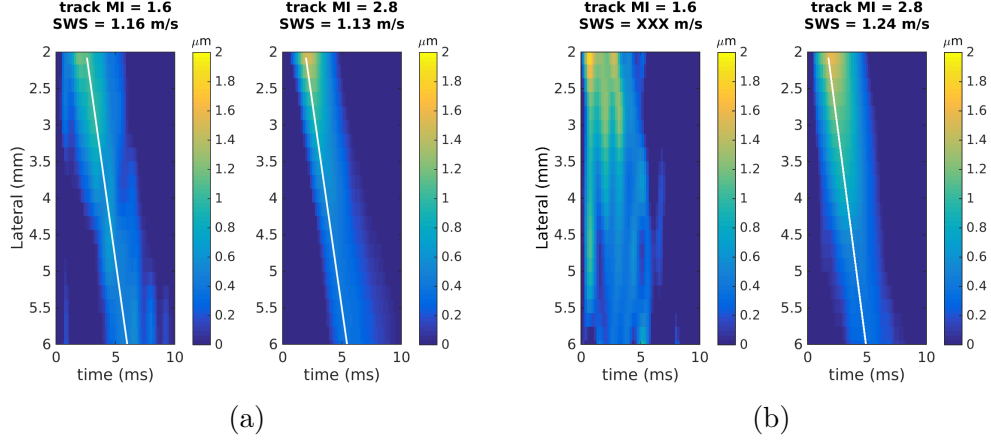


FIGURE 5.2: Example shear wave trajectories using low and high MI tracking focused at 5 cm. (a) An easy-to-image volunteer ($BMI = 20.9 \text{ kg/m}^2$), where both low and high MI tracking yield successful SWS estimates and similar SWS values. (b) A difficult-to-image patient ($BMI = 31.8 \text{ kg/m}^2$), where low MI tracking failed to produce a successful SWS estimate.

the jitter noise in the shear wave signal.

The correlation coefficients (CC) from locations away from the ARFI excitation were averaged across all acquisitions for each subject at both focal depths as shown in Figure 5.3. The error-bars reflect the inter-subject variability. High MI tracking results in significantly higher CC at both focal depths. The mean CC as well as the corresponding SNR of the tracking data are listed in Table 5.3. High MI tracking increased the SNR of the tracking data by 6.5 and 5.5 dB at focal depths of 5 cm and 9 cm respectively.

Table 5.3: Correlation coefficients (CC) and Signal-to-noise ratio (SNR) of the tracking data at both MI values for each focal depth

Focal depth	5 cm		9 cm	
Track MI	1.6	2.8	1.6	2.8
Mean CC	0.980	0.996	0.966	0.990
SNR (dB)	16.9	23.4	14.5	20.0

Displacement jitter was computed in all acquisitions for each subject and fo-

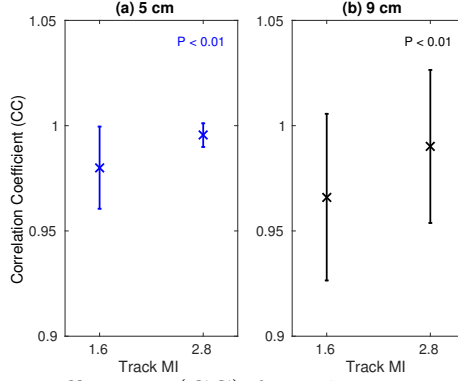


FIGURE 5.3: Correlation coefficients (CC) from locations away from the shear wave where zero motion is expected averaged across all acquisitions for each subject at low and high MI tracking for focal depths (a) 5 cm and (b) 9 cm. The error-bars reflect the inter-subject variability which was smallest at the shallowest focal depth and highest MI. High MI tracking results in significantly higher CC at both focal depths with p-values < 0.01 .

cal depth and the results are shown in Figure 5.4. Jitter was computed from raw displacement data through time, as well as filtered data with different cut-off frequencies. The error-bars reflect the inter-subject variability. In all cases, using the same push configurations, high MI tracking results in significantly lower jitter.

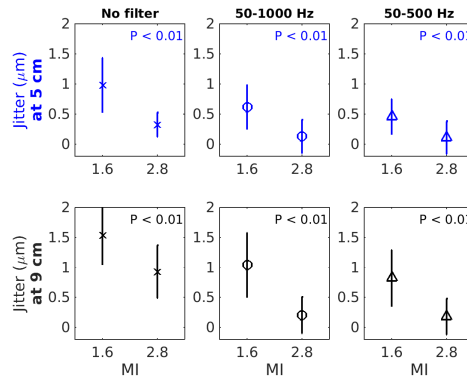


FIGURE 5.4: Displacement jitter computed from low and high MI tracking. The error-bars reflect the inter-subject variability. The top row shows the jitter when focused at 5 cm, and the bottom row shows the jitter when focused at 9 cm. The title of each sub-figure in the top row indicates the data/filtering type. In all cases, high MI tracking results in significantly lower jitter with p-values < 0.01 .

Maximum displacement at around 1 mm from the push was also estimated for each measurement. Figure 5.5 shows the maximum displacement ratio between high

and low MI tracking. The error-bars reflect the inter-subject variability. The maximum displacement is not significantly different between low and high MI tracking at either focal depth with p-values ≥ 0.65 .

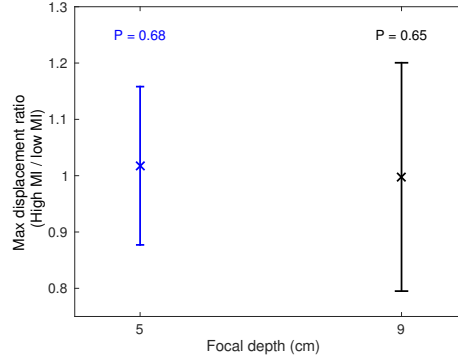


FIGURE 5.5: Ratio of maximum displacements obtained with high and low MI tracking in all acquisitions from all subjects. The error-bars reflect the inter-subject variability. The mean ratio is close to 1 at both focal depths.

The percent SWS yield data were separated with respect to B-mode image quality and illustrated in Figure 5.6. From these data we observe that high MI tracking increases SWS yield for all image qualities. SWS yield is lower in more difficult-to-image subjects at both focal depths, and the relative yield improvement going from low to high MI tracking is higher in more difficult-to-image subjects and at the deeper focal depth. Using elevated MI tracking, SWS yield improved by 1.5x, 1.7x, and 1.9x in easy, medium and difficult subjects respectively at 5 cm, and 2.4x, 5.0x, and 7.0x at 9 cm.

5.5 Discussion

This paper evaluates the benefit of using elevated MI for harmonic motion tracking in SWEI. SWS estimation yield increased significantly going from low to high MI tracking at the 2 focal depths (5 cm and 9 cm) used in this study as shown in Figures 5.1 and 5.6.

High MI tracking significantly improves the tracking data quality by increasing

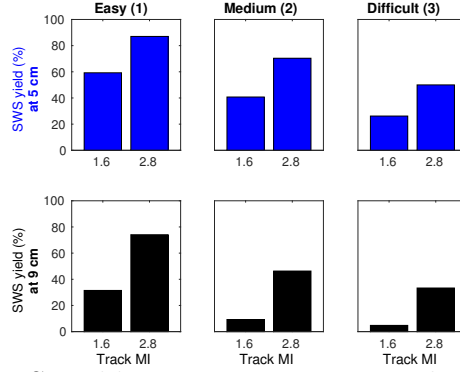


FIGURE 5.6: Percent SWS yield at various image qualities. The image quality is represented by scores 1-3 (1 - easy, 2 - medium, 3 - difficult). The top row shows the results when focused at 5 cm, and the bottom row shows the results when focused at 9 cm.

SNR and the correlation coefficient (CC) in motion estimation as shown in Figure 5.3 and Table 5.3. The SNR of harmonic tracking data increased on the order to 4 – 6 dB going from low to high MI tracking at both focal depths. The increase in SNR and CC results in the reduction of displacement jitter as described by the CRLB. Figure 5.4 shows that high MI tracking decreases jitter in raw (left) and filtered (center and right) tissue motion data. The BPF with cut-off frequencies 50 – 1000 Hz in the center column of Figure 5.4 is typically applied to tissue motion data in hepatic SWEI to reduce background motion artifact and jitter noise [27], and was included in the data processing pipeline to estimate SWS in this study. As expected, the jitter amplitude is lower in the filtered data than in the raw data at both focal depths and at both tracking MI values. On the other hand, high MI tracking has lower displacement jitter after the BPF, indicating that high MI tracking still provides the benefit of lower jitter and higher tracking data quality after the post-acquisition data filtering. The right column of Figure 5.4 shows the jitter amplitude after the displacement data was filtered with cut-off frequencies 50 – 500 Hz. The jitter amplitude of high MI tracking is still significantly lower than that of low MI tracking after this aggressive filter. These results indicate that the

benefit of lower jitter provided by high MI tracking is present in raw data as well as in filtered data after post-acquisition data processing.

As shown in Figure 5.6, SWS yield is directly related to image quality, with lower SWS yield observed from more difficult-to-image subjects at both focal depths. High MI tracking leads to higher SWS yield for all image qualities. In addition, the relative SWS yield improvement going from low to high MI tracking is higher for more difficult-to-image subjects. This indicates that difficult-to-image patients are less likely to produce successful SWS measurements under the current FDA MI guideline, and are more likely to benefit from using elevated MI in shear wave tracking to obtain reliable SWS measurements. These findings suggest that B-mode image quality could be used prospectively to identify patients who would be likely to have low SWS estimation yield, and would potentially benefit from using elevated MI shear wave tracking.

Chapter 3 concludes that liver capsule depth could be used to identify patients who would benefit from high MI ARFI excitation. In this study, the liver capsule depth was also estimated from the B-mode image of each study subject. Figure 5.7 shows the scatter plot of liver capsule depths as a function of B-mode image quality. Easy-to-image subjects had liver capsule depths ≤ 30 mm, while difficult subjects had liver capsule depths ≥ 30 mm. Liver capsule depth ≥ 30 mm can be used to identify difficult-to-image patients who would suffer from low SWS estimation yield, and would benefit from using elevated output in harmonic motion tracking.

A limitation of this study was the use of a single track focal configuration, which employs focused harmonic tracking. This method affords the highest quality data at the expense of frame rate. Alternative tracking methods include plane wave imaging, which has been used extensively in SWEI (multiple track location) [8, 46]. Future work will be directed to evaluate the impact of using elevated acoustic output between different track focal configurations, particularly between focused harmonic tracking

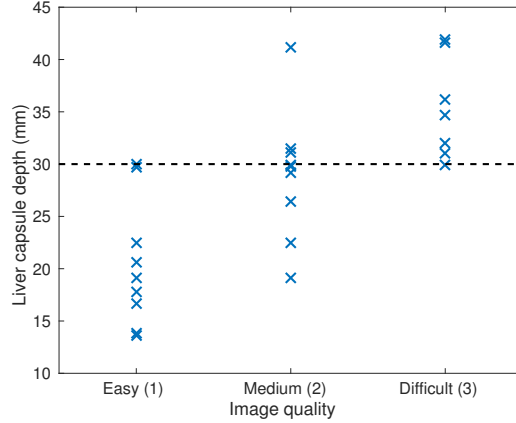


FIGURE 5.7: Scatter plot of liver capsule depths as a function of B-mode image quality. Easy-to-image subjects had liver capsule depths ≤ 30 mm, while difficult subjects had liver capsule depths ≥ 30 mm.

and plane wave harmonic tracking as well as plane wave coherent compounding [60].

5.6 Conclusions

This study investigated the clinical benefit of using elevated MI in shear wave harmonic tracking. SWS measurements were acquired from 25 subjects at two focal depths, 5 cm and 9 cm. High MI tracking resulted in higher data quality with lower jitter in tissue motion data. The rate of successful SWS reconstruction increased when going from low to high MI tracking in all subjects, with larger SWS yield improvements in difficult-to-image subjects. B-mode image quality and liver capsule depth could be used as indicators to predict patients who would have low SWS estimation yield and would benefit significantly from using elevated MI to obtain reliable SWS measurements. We thus conclude that there is clinical benefit of using elevated MI in harmonic shear wave tracking.

6

Challenges of developing high MI imaging systems

This chapter summarizes the systematic and physical challenges we encountered during the development of high MI imaging sequences for the clinical studies presented in the previous chapters.

6.1 Saturation pressure

The acoustic pressure at the focus measured in water is limited by the saturation pressure, which presents an upper limit for the pressure amplitude, and thus MI, for a given transducer configuration measured in water. The saturation pressure $p_{sat,f}$, is calculated as Equation (2) of [32]:

$$p_{sat,f} = \frac{\rho_0 c^3}{2\beta f z} \frac{G}{\ln G}. \quad (6.1)$$

where ρ_0 is the equilibrium density of the fluid, c is speed of sound, β is the nonlinear parameter of the fluid ($\beta = B/2A + 1$), f is the center frequency of the sound wave, z is the focal depth, and G is the focusing gain. The focusing gain G is dependent on the size of the transmit aperture, and G is typically between 4 – 10 in diagnostic ultrasound transducers [32]. Equation (6.1) indicates that the saturation pressure increases with increasing aperture size, and decreases with increasing imaging focal

depth, frequency, and tissue nonlinearity. Because the acoustic attenuation of water is very small (0.05 dB/cm/MHz), water-based MI measurements are often affected by acoustic saturation, where further increases in source pressure do not result in an increase in the pressure at the focus. The measured pressure at the focal point in water p_f and the saturation pressure $p_{sat,f}$ are related by (combining Equation (6.1) and Equation (A5) of [32]):

$$p_f = p_{sat,f} \frac{p_0}{A + p_0}. \quad (6.2)$$

where p_0 is the source pressure, and A is a constant that incorporates the transducer focal gain and other system and material properties:

$$A = \left(1 - \frac{1}{\pi}\right) \frac{\rho_0 c^3}{2\beta f z \ln G}. \quad (6.3)$$

Equation (6.2) indicates that p_f increases with increasing p_0 . When p_0 is very large compared to A , p_f asymptotes to saturation pressure ($p_{sat,f}$). This results in a maximum Mechanical Index that can be measured for a given focal configuration.

The blue curve in Figure 6.1 shows the MI values measured in a water tank using a range of scanner voltages with the Siemens S2000 scanner and 4C1 curvilinear array. The transmit pulse was at 2.2 MHz and focused at 5 cm. The MI values measured did not increase linearly with increasing scanner voltage. The asymptotic relationship between MI and scanner voltage is due to saturation pressure. At high scanner voltage, the MI plateaus to the maximum MI that can be achieved, which is dictated by the saturation pressure.

6.2 MI and MIE

Due to saturation pressure and pre-focal loss in water-based pressure measurement, the Mechanical Index (MI) is likely to underestimate *in situ* pressure amplitude at

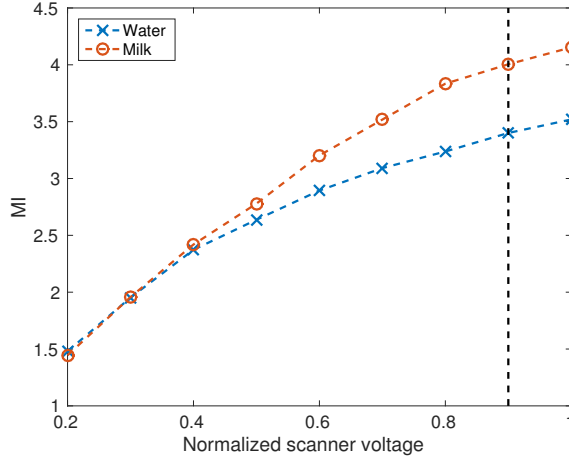


FIGURE 6.1: MI and MIE measurements at a range of scanner voltages using the 4C1 transducer at a focal depth of 5 cm. The MI values did not increase linearly with increasing scanner voltage, but rather asymptotes to the maximum value dictated by the saturation pressure. MIE values are higher than MI values at the same scanner voltages for MIs > 2.5 . Particularly, using a normalized scanner voltage of 0.9, the MI is 3.4 while the MIE is 4.0 as indicated by the black dashed line.

high MI levels. The orange curve in Figure 6.1 shows the effective Mechanical Index (MIE) measured in a milk solution. The milk solution was tuned to have an attenuation of 1.1 dB/cm at 2.2 MHz (0.5 dB/cm/MHz assuming linear frequency dependence), in order to more closely match the acoustic attenuation of tissue. Figure 6.1 shows that the MI and MIE measurements are in agreement for MI values < 2.5 . At higher MI levels, MIE values are higher than MI values at the same scanner voltages, indicating that MI underestimates the pressure amplitude in an attenuating medium. Particularly, using a normalized scanner voltage of 0.9, the MI is 3.4 while the MIE is 4.0 as indicated by the black dashed line. Based on the AIUM report [64], we should limit the acoustic output to an MIE of 4.0, which corresponds to a lower MI of 3.4 using this focal configuration.

Figure 6.1 indicates that water based MI measurements are likely to underestimate *in situ* pressure amplitude at high MI values. On the other hand, MI is likely to overestimate pressure amplitude at low pressure levels due to its fixed derating scheme as discussed in Section 2.1.2. Therefore, MIE was proposed to provide a more

accurate estimation of *in situ* pressure amplitude to assess the likelihood of cavitation. However, there is not a current consensus on a method of quantify MIE. Future work should be directed to formulate a standardized MIE measurement protocol that accurately represents *in situ* pressure amplitude.

6.3 Region of increased acoustic output

Due to the saturation pressure and the linear derating scheme employed for MI measurement, there is a focal-depth dependent upper limit on MI that can be achieved with a given transducer. Figure 6.2 shows the MI values currently employed by ultrasound manufacturers (blue line), as well as the maximum MI values achievable with commercially available abdominal transducers (6C1, 4C1, C52, red line). The red shaded region indicates the elevated acoustic output regime we explored in the previous chapters. The maximum MI achievable decreases with increasing depth. To increase MI values further at depth, larger apertures and lower frequencies are required. We have recently designed a custom prototype transducer (PX) that extends the transmit frequency capabilities down to 1.3 MHz and increases the aperture surface area. This prototype deep abdominal transducer enabled us to extend the output regime at depth as represented by the gray shaded region. We were able to achieve elevated MI values greater than 1.9 for focal depths > 10 cm using the PX in the clinical studies described in Chapters 4 and 5.

6.4 System non-linearity

Apart from the saturation pressure, the MI values used in the clinical studies were further limited by scanner hardware. The commercial ultrasound scanner S2000 used in the clinical studies in Chapters 4 and 5 was designed to operate under the FDA guideline of $MI < 1.9$. We observed system non-linearities when transmitting at high MI values.

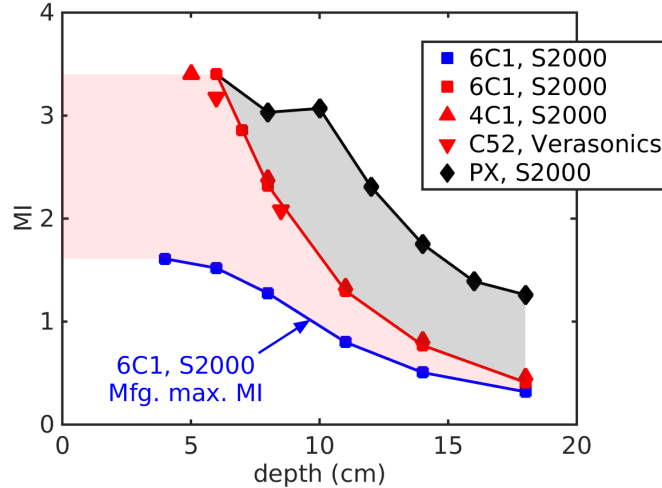


FIGURE 6.2: Region of increased acoustic output that was explored herein. The lower boundary of the shaded region (blue line, 6C1, S2000) represents the MI measured at each depth (i.e., z , not z_{MI} , see Equation 2.1) using a Siemens 6C1 curvilinear array and S2000 scanner with the maximum manufacturer-allowed MI settings. Shaded regions indicate the acoustic output regime we explored. The red shaded region indicates the regime with commercial, curvilinear arrays (4C1: 1.8 MHz; 6C1: 2.0 MHz; C52: 2.4 MHz); the black diamonds and gray shaded region represent the elevated MIs with the PX transducer.

The positive and negative leading edge transmit pulses were measured with the hydrophone at the transducer surface using a range of scanner excitation voltages. Figure 6.3 plots the surface measured pulses using the 4C1 transducer with a focal depth of 6 cm at 2 transmit powers (0.3 and 0.6). The top row of Figure 6.3 shows the positive and negative leading edge pulses. The two pulses appear to be out of phase at both scanner powers. On the other hand, the bottom row of Figure 6.3 plots the positive leading edge pulse as well as the inverse of the negative leading edge pulse concurrently to compare their differences. Qualitatively the two pulses differ to a greater extent at the higher scanner power, indicating system non-linearity particularly at the peak positive pressures.

The system non-linearity was quantified by measuring the correlation coefficient (CC) and Root-mean-square (RMS) difference between the positive and negative ledge transmitted pulses. The ideal CC is 1, so that the two pulses cancel each

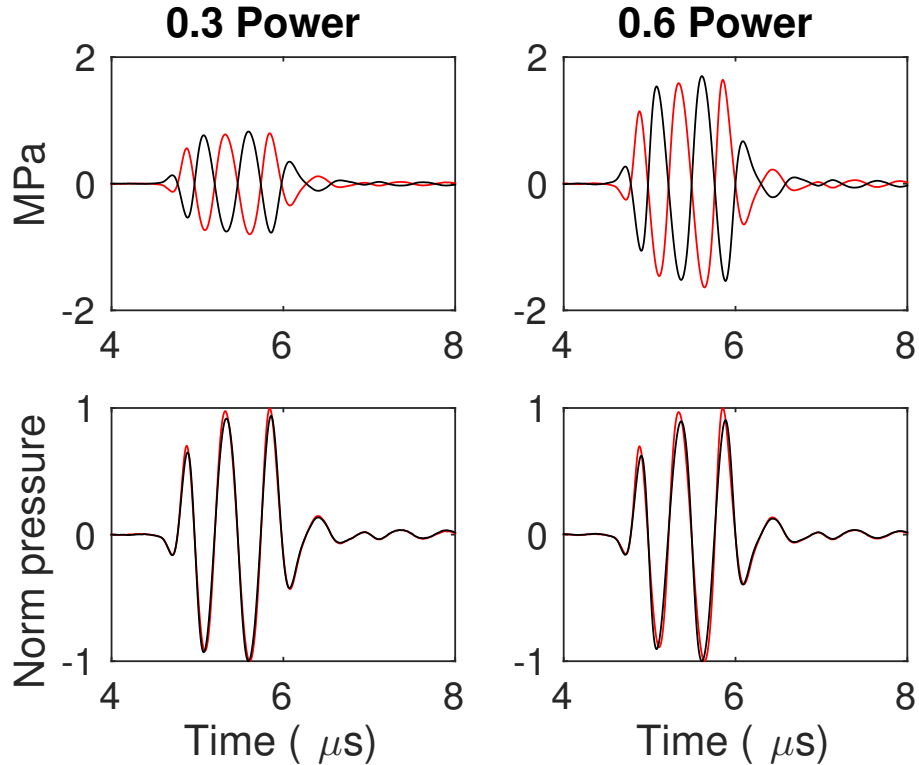


FIGURE 6.3: Positive and negative leading edge transmit pulses measured with the hydrophone at the transducer surface at 2 scanner voltages. Top: Absolute positive and negative leading edge pulses. Bottom: Normalized positive leading edge pulse and the inverse of the negative leading edge pulse.

other perfectly during summation in pulse-inversion harmonic imaging, and all the signal left is generated harmonics (as compared to transmitted). Figure 6.4 shows the correlation coefficient (CC) and RMS difference using the 4C1 transducer at a range of scanner excitation voltages. The CC decreases with increasing scanner voltage at different focal depths and pulse lengths. RMS difference increases with increasing scanner voltage. A lower CC and higher RMS difference result in imperfect cancellation of the transmitted signals during pulse inversion, which introduces undesirable harmonic content in the received signal and degrades harmonic image quality. We imposed a minimum correlation coefficient magnitude threshold of 0.98 to maintain high levels of cancellation. This correlation coefficient threshold dictated the maximum MI for each sequence used in the clinical study.

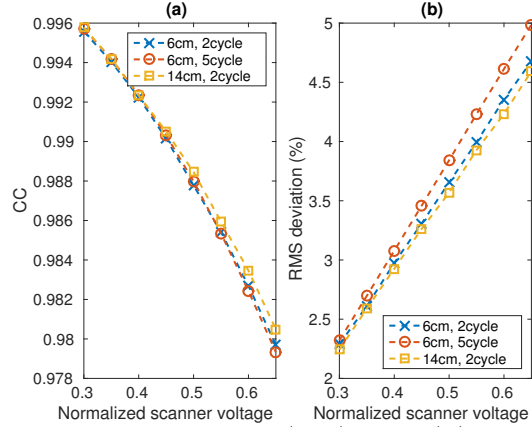


FIGURE 6.4: (a) Correlation coefficient (CC) and (b) Percent RMS pressure difference between the positive and negative ledge pulses using the 4C1 transducer at focal depths of 6 and 14 cm, using 2-cycle and 5-cycle transmits. The CC decreases with increasing scanner voltage regardless of focal depth and pulse length.

6.5 Real-time high MI imaging systems

Chapter 4 shows that high MI harmonic imaging resulted in modest improvement in CNR of hypoechoic hepatic vessels. However, all hypoechoic structures identified in that study were visualized at low MI imaging. It is useful to develop real-time high MI harmonic imaging sequences to scan for low contrast targets. Thermal related safety limits of diagnostic ultrasound, such as I_{SPTA} and transducer surface temperature rise limits, would restrict the frame rate for real-time imaging sequences. The I_{SPTA} limit, which is 720 mW/cm^2 in non-fetal tissue [15], is considered here.

A Field II simulation was performed to simulate the transmit focal configurations using the 4C1 curvilinear array at a focal depth of 6 cm with an attenuation of 0.3dB/cm/MHz . Figure 6.5 shows the transmit intensity distribution. The high MI sequence used in the clinical study in Chapter 4 had an MI of 2.6 focused at 6 cm. The corresponding pulse average intensity (I_{pa}) was measured to be 564 W/cm^2 at the focal point.

The intensity distribution was rotated with respect to the apex of the transducer to simulate different transmit beam directions in a B-mode imaging case. The B-

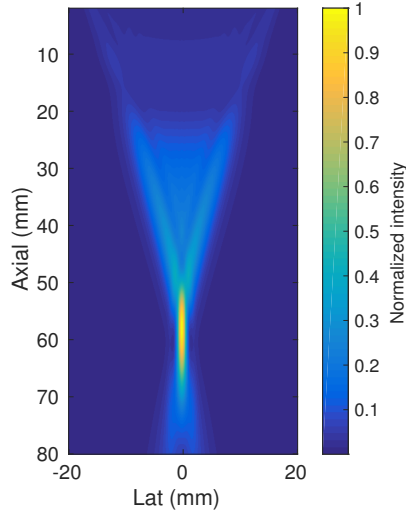


FIGURE 6.5: Intensity distribution of an F/1.5 transmit focused at 6 cm using the 4C1 transducer

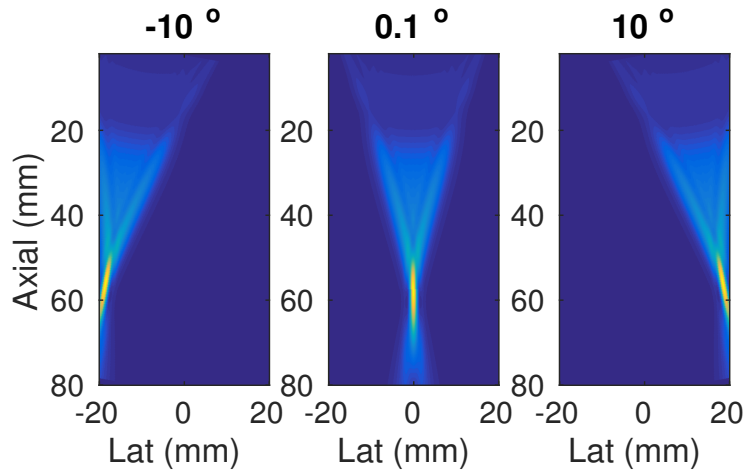


FIGURE 6.6: Example intensity distribution at -10° , 0.1° , 10° with respect to the apex of the 4C1 transducer

mode imaging sequence used in Chapter 4 consisted of 256 equally spaced beams that spanned a angular field of view of -35° to 35° . Figure 6.6 shows example intensity distribution at -10° , 0.1° , 10° .

Summing up the intensity distribution from each of the 256 transmit beams, Figure 6.7 shows that the maximum intensity of this B-mode sequence is located at 31 mm axially, and its amplitude is 7.9 times the maximum intensity of a single

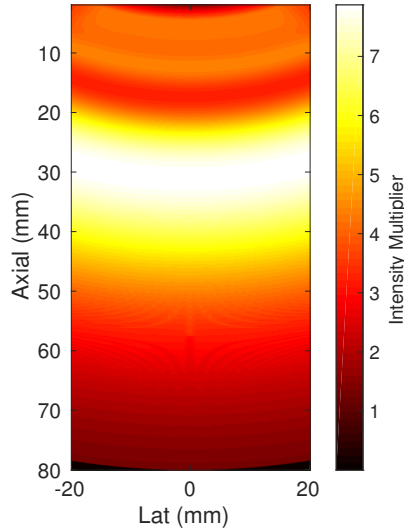


FIGURE 6.7: Intensity multiplier between the maximum intensity of a B-mode imaging case and a single transmit. The maximum intensity of this B-mode sequence is located at 31 mm axially, and its amplitude is 7.9 times the maximum intensity of a single transmit at focus.

transmit measured at the focal point. Given this intensity multiplier information, we can perform real-time harmonic imaging using an MI of 2.6 at a frame rate up to 41 frames per second to stay within the I_{SPTA} limit of 720 mW/cm^2 . Therefore, we hypothesize that transducer surface heating will be the limiting factor for the frame rate of high MI harmonic imaging. On the other hand, we did not model transducer surface heating in this analysis, which would add to tissue heating near the surface. Future work will be directed to optimize the scanning protocol to minimize transducer surface heating. A more efficient transducer design with effective heat dissipation or an active cooling system would be able to reduce the transducer surface temperature rise during scanning, and therefore facilitate increased frame rates.

7

Conclusions

Harmonic imaging is typically signal-to-noise ratio (SNR) and penetration-depth limited during clinical imaging, resulting in decreased diagnostic utility. A logical approach to increase the SNR of harmonic imaging is to increase the source pressure. This dissertation explored the potential diagnostic benefit of employing elevated acoustic output beyond the FDA guideline $MI = 1.9$ in the context of hepatic imaging, specifically in B-mode harmonic imaging and shear wave elasticity imaging (push and track). To accomplish these goals, B-mode and SWEI imaging sequences using high MI transmits were developed, and clinical studies were conducted to evaluate the clinical impact of high MI imaging.

The results from Chapter 3 show that SWS estimation yield and displacement amplitude increase with increasing push energy. The push energy (ARFI excitation) can be increased by either increasing the MI of the push pulse or increasing the push duration. Using elevated push energies enabled successful SWS measurements in previously failed patients. Liver capsule depth ≥ 35 mm was an indicator of lower SWS yield. Patients with deep liver capsules were more likely to fail at standard push energy levels and thus would benefit more from elevated output.

Chapter 4 demonstrates that using elevated acoustic output in B-mode harmonic

imaging results in modest improvement in the CNR of hypoechoic hepatic vessels, and the improvement was higher in medium and difficult-to-image subjects than easy subjects. The imaging penetration depth increased linearly with increasing MI, on the order of 4 – 7 cm per unit MI increase at a given focal depth. Additionally, in one patient, CNR increases $\geq 30\%$ were consistently observed going from low to high MI harmonic imaging.

Chapter 5 shows that harmonic motion tracking using elevated acoustic output increased SWS estimation yield by 28% and 37% at 2 focal depths (5 cm and 9 cm), caused by higher tracking data quality with higher SNR and lower jitter. The rate of successful SWS reconstruction increased going from low to high MI tracking in all subjects, with larger SWS yield improvements in difficult-to-image subjects. We found that B-mode image quality and liver capsule depth could be used as indicators to predict patients who would likely have low SWS estimation yield and would benefit from using elevated MI in harmonic motion tracking. The results presented in these studies show promise for using elevated acoustic output to provide clinical benefit to ultrasonic abdominal imaging.

7.1 Future work

The work presented in this dissertation provides evidence that using elevated acoustic output has the potential to provide clinical benefit in B-mode harmonic imaging and in ultrasound elastography. However, several challenges have been identified regarding the design and implementation of current studies, which should be addressed to further assess the cost and benefit of using elevated acoustic output in diagnostic ultrasound.

The Mechanical Index (MI) calculated from water-based pressure measurements with a linear derating factor does not accurately represent *in situ* pressure amplitude in human tissues. Acoustic propagation through water is a highly nonlinear

process that inherently differs in attenuation, nonlinearity, and path heterogeneity from propagation in tissue. The MI can overestimate or underestimate the *in situ* acoustic output depending on the pressure amplitude and that the peak rarefactional pressure (PRP) can occur in spatially offset locations when imaging through heterogeneous media such as the abdominal wall. Future work will be directed to use a full-wave [76] package to simulate acoustic propagation through various human abdominal wall samples to evaluate the position and magnitude of PRPs, in order to demonstrate how these parameters can affect PRP compared to that predicted by water based MI measurements.

High MI B-mode harmonic imaging was shown to result in modest improvement in CNR of the hypoechoic hepatic vessels in the clinical study presented in Chapter 4. As discussed previously, this study should be expanded to use real-time high MI sequences to scan liver lesions to further examine the impact of high MI imaging on lower contrast targets. Liver lesions are generally low contrast targets and are located deep in the body. Current ultrasonic exams typically fail to visualize these targets and using high MI harmonic imaging might be a promising direction to visualize these targets using B-mode ultrasound. Moreover, the optimal focal configurations for deep abdominal harmonic imaging is to be studied. Systematic evaluation of harmonic signal amplitude at depth should be performed to determine the optimal imaging parameters such as focal depth and F number to maximize harmonic generation at depth.

In addition, only 2 MI values were used for each focal depth in the B-mode sequences and CNR computation. This limits the ability to draw conclusions about MI thresholds and minimum CNR increases. Future work should also be focused on evaluating image quality at a series of MI values to determine the maximum MI needed for significant image quality improvement.

Current shear wave imaging techniques using a conventional curvilinear array

for abdominal imaging are typically limited to an axial depth of 7 cm [90]. In the motion tracking study presented in Chapter 5, we demonstrated reliable SWS measurements ($> 50\%$ yield) at 9 cm using elevated MI tracking and a custom designed low frequency transducer. Future work should be directed to combine the benefits of high MI in pushing and tracking, as well as the prototype transducer to further increase the axial field of view for shear wave imaging.

The challenges of developing high MI imaging sequences were discussed in Chapter 6. It is difficult to achieve elevated MI at deep focal depths using conventional curvilinear arrays due to pre-focal loss in water and limited aperture size. It would be valuable to design a low frequency transducer with a larger surface area for deep abdominal imaging. There are many possibilities in improving deep abdominal imaging using such a transducer and using elevated acoustic output. In addition, system non-linearity was observed, which was a confounder that could degrade image quality using elevated acoustic output. To facilitate high MI imaging, clinical scanners that have minimal system nonlinearity at high MI values must be developed.

7.2 Technical and Clinical Contributions and Implications

The work presented in this thesis demonstrates initial studies exploring the potential diagnostic benefit of employing elevated acoustic output beyond the FDA guideline of $MI = 1.9$ in hepatic imaging. B-mode, M-mode, and SWEI imaging sequences using elevated acoustic output were developed and implemented on modified clinical ultrasound scanners and used to acquire data on human subjects. Contrast-to-noise ratio (CNR), correlation coefficient (CC), imaging penetration depth (PD), SWS estimation yield and displacement jitter were developed to serve as metrics to evaluate image quality. These imaging sequences and imaging metrics lay the ground work for investigating image quality using elevated acoustic output in B-mode and shear wave imaging modes. They can be continuously employed and modified in future

studies.

The results presented in this thesis demonstrate that elevated acoustic output has the potential to improve image quality of diagnostic ultrasound. Specifically, high MI harmonic imaging improves CNR of hepatic vessels and imaging penetration depth. High MI pushing and tracking improve SWS yield in ultrasound elastography. These promising findings begin to build the foundations for a collaborative effort between ultrasound manufacturers, research communities, clinicians, as well as regulatory bodies to examine the cost and benefit of using elevated acoustic output, thereby assessing the possibility for the FDA to modify the MI guideline to improve the diagnostic utility of ultrasound imaging.

Bibliography

- [1] AIUM. American Institute of Ultrasound in Medicine Statement on Heat. Technical report, 2009.
- [2] AIUM/NEMA. Standard for Real-Time Display of Thermal and Mechanical Acoustic Output Indices on Diagnostic Ultrasound Equipment, 1992.
- [3] C. Amador, P. Song, D. D. Meixner, S. Chen, and M. W. Urban. Improvement of Shear Wave Motion Detection Using Harmonic Imaging in Healthy Human Liver. *Ultrasound in Medicine & Biology*, 42(5):1–11, 2016.
- [4] American Institute of Ultrasound in Medicine/National Electrical Manufacturers Association (AIUM/NEMA). *Acoustic output measurement standard for diagnostic ultrasound equipment*. 1998.
- [5] R. E. Apfel and C. K. Holland. Gauging the likelihood of cavitation from short-pulse, low-duty cycle diagnostic ultrasound. *Ultrasound in Medicine and Biology*, 17(2):179–185, 1991.
- [6] U. Arena, M. L. Platon, C. Stasi, S. Moscarella, A. Assarat, G. Bedogni, V. Piazzolla, R. Badea, G. Laffi, F. Marra, A. Mangia, and M. Pinzani. Liver stiffness is influenced by a standardized meal in patients with chronic hepatitis C virus at different stages of fibrotic evolution. *Hepatology*, 58(1):65–72, 2013.
- [7] E. H. Asham, A. Kaseb, and R. M. Ghobrial. Management of Hepatocellular Carcinoma. *Surgical Clinics of North America*, 93(6):1423–1450, 2013.
- [8] J. Bercoff, M. Tanter, and M. Fink. Supersonic shear imaging: A new technique for soft tissue elasticity mapping. *IEEE Transactions on Ultrasonics, Ferroelectrics, and Frequency Control*, 51(4):396–409, 2004.
- [9] W. A. Berg, D. O. Cosgrove, C. J. Dore, F. K. W. Schafer, W. E. Svensson, R. J. Hooley, R. Ohlinger, E. B. Mendelson, C. Balu-Maestro, M. Locatelli, C. Tourasse, B. C. Cavanaugh, V. Juhan, A. T. Stavros, A. Tardivon, J. Gay, J.-P. Henry, and C. Cohen-Bacrie. Shear-wave Elastography Improves the Specificity of Breast US: The BE1 Multinational Study of 939 Masses. *Radiology*, 262(2):435–449, 2012.

- [10] R. T. Beyer. Parameter of nonlinearity in fluids. *The Journal of the Acoustical Society of America*, (32):719–721, 1960.
- [11] C. Bradley. Mechanisms of image quality improvement in tissue harmonic imaging. In *AIP Conference Proceedings*, volume 838, pages 247–254, 2006.
- [12] J. Bruix and M. Sherman. Management of hepatocellular carcinoma: An update. *Journal of Hepatology*, 53(3):1020–1022, 2011.
- [13] E. Bugianesi, A. J. McCullough, and G. Marchesini. Insulin resistance: a metabolic pathway to chronic liver disease. *Hepatology (Baltimore, Md.)*, 42(5):987–1000, 2005.
- [14] P. N. Burns, S. R. Wilson, and D. H. Simpson. Pulse inversion imaging of liver blood flow: improved method for characterizing focal masses with microbubble contrast. *Investigative radiology*, 35(1):58–71, 2000.
- [15] Center for Devices and Radiological Health (CDRH). 510(k) Guide for Measuring and Reporting Acoustic Output of Diagnostic Ultrasound Medical Devices. *US Dept of Health and Human Services 1985, Rev. 1993*, 1994.
- [16] T. Christopher. Finite amplitude distortion-based inhomogeneous pulse echo ultrasonic imaging. *IEEE Transactions on Ultrasonics, Ferroelectrics, and Frequency Control*, 44(1):125–139, 1997.
- [17] T. Christopher. Experimental investigation of finite amplitude distortion-based, second harmonic pulse echo ultrasonic imaging. *IEEE Transactions on Ultrasonics, Ferroelectrics, and Frequency Control*, 45(1):158–162, 1998.
- [18] C. C. Church. Spontaneous homogeneous nucleation, inertial cavitation and the safety of diagnostic ultrasound. *Ultrasound in Medicine and Biology*, 28(10):1349–1364, 2002.
- [19] C. C. Church, E. L. Carstensen, W. L. Nyborg, P. L. Carson, L. A. Frizzell, and M. R. Bailey. The risk of exposure to diagnostic ultrasound in post-natal subjects: nonthermal mechanisms. *Journal of ultrasound in medicine*, 27(4):565–592;, 2008.
- [20] C. C. Church, C. Labuda, and K. Nightingale. A theoretical study of inertial cavitation from acoustic radiation force impulse imaging and implications for the mechanical index. *Ultrasound in medicine & biology*, 41(2):472–85, Feb. 2015.
- [21] C. C. Church, C. Labuda, and K. R. Nightingale. Should the mechanical index be revised for ARFI imaging? *IEEE International Ultrasonics Symposium : [proceedings]. IEEE International Ultrasonics Symposium*, 2012:17–20, Oct. 2012.

- [22] R. S. Cobbold. *Foundations of Biomedical Ultrasound*. Oxford University Press, 2006.
- [23] K. M. F. Cynthia L. Ogden, Margaret D. Carroll, Brian K. Kit. Prevalence of Childhood and Adult Obesity in the United States, 2011-2012. *Jama*, 2014.
- [24] N. de Jong, R. Cornet, and C. Lancée. Higher harmonics of vibrating gas-filled microspheres. Part two: measurements, 1994.
- [25] A. de Moura Almeida, H. P. Cotrim, D. B. V. Barbosa, L. G. M. de Athayde, A. S. Santos, A. G. a. V. Bitencourt, L. A. R. de Freitas, A. Rios, and E. Alves. Fatty liver disease in severe obese patients: diagnostic value of abdominal ultrasound. Technical Report 9, Faculdade de Medicina da Bahia, Universidade Federal da Bahia, Avenida Tancredo Neves, Ed. Salvador Trade Center, Torre Norte-Sala 717, Salvador, Bahia 41830-020, Brazil., 2008.
- [26] Y. Deng, M. L. Palmeri, N. C. Rouze, S. J. Rosenzweig, M. F. Abdelmalek, and K. R. Nightingale. Analyzing the Impact of Increasing Mechanical Index and Energy Deposition on Shear Wave Speed Reconstruction in Human Liver. *Ultrasound in Medicine & Biology*, 41(7):1948–1957, 2015.
- [27] Y. Deng, N. C. Rouze, M. L. Palmeri, and K. R. Nightingale. Ultrasonic Shear Wave Elasticity Imaging (SWEI) Sequencing and Data Processing Using a Verasonics Research Scanner. *IEEE Transactions on Ultrasonics, Ferroelectrics, and Frequency Control*, 64(1):164–176, 2017.
- [28] T. S. Desser, T. Jedrzejewicz, and C. Bradley. Native tissue harmonic imaging: basic principles and clinical applications. *Ultrasound Quarterly*, 16(1):40–48, 2000.
- [29] T. S. Desser and R. B. Jeffrey. Tissue harmonic imaging techniques: physical principles and clinical applications. *Seminars in ultrasound, CT, and MR*, 22(1):1–10, 2001.
- [30] J. R. Doherty, J. J. Dahl, and G. E. Trahey. Harmonic tracking of acoustic radiation force-induced displacements. *IEEE Transactions on Ultrasonics, Ferroelectrics, and Frequency Control*, 60(11):2347–2358, 2013.
- [31] J. R. Doherty, G. E. Trahey, K. R. Nightingale, and M. L. Palmeri. Acoustic radiation force elasticity imaging in diagnostic ultrasound. *IEEE transactions on ultrasonics, ferroelectrics, and frequency control*, 60(4):685–701, Apr. 2013.
- [32] F. A. Duck. Acoustic saturation and output regulation. *Ultrasound in Medicine and Biology*, 25(6):1009–1018, 1999.
- [33] F. A. Duck. Nonlinear acoustics in diagnostic ultrasound. *Ultrasound in Medicine and Biology*, 28(1):1–18, 2002.

- [34] I. electrotechnical commision. IEC 62359: Ultrasonics - Field characterization - Test methods for the determination of thermal and mechanical indices related to medical diagnostic ultrasonic fields. *International electrotechnical commision, Geneva, Switzerland, 2 edition*, 2010.
- [35] FDA. Diagnostic Ultrasound Guidance for 1993 [February 17, 1993, Revised 510 (k)] Rockville, MD: Center for Devices and Radiological Health. *Food and Drug Administration, US Department of Health and Human Services*, 1993.
- [36] C. Fierbinteanu-Braticevici, D. Andronescu, R. Usvat, D. Cretoiu, C. Baicus, and G. Marinoschi. Acoustic radiation force imaging sonoelastography for noninvasive staging of liver fibrosis. Technical Report 44, Medical Clinic II and Gastroenterology, University Hospital, Bucharest, Romania., 2009.
- [37] J. B. Fowlkes. American Institute of Ultrasound in Medicine consensus report on potential bioeffects of diagnostic ultrasound: executive summary. In *Journal of ultrasound in medicine*, volume 27, pages 503–515. Basic Radiological Sciences Division, Department of Radiology, University of Michigan Health System, Kresge III, Room 3320, 200 Zina Pitcher Pl, Ann Arbor, MI 48109-0553 USA. fowlkes@umich.edu, 2008.
- [38] M. Friedrich-Rust, K. Wunder, S. Kriener, F. Sotoudeh, S. Richter, J. Bojunga, E. Herrmann, T. Poynard, C. F. Dietrich, J. Vermehren, S. Zeuzem, and C. Sarrazin. Liver fibrosis in viral hepatitis: noninvasive assessment with acoustic radiation force impulse imaging versus transient elastography. *Radiology*, 252(2):595–604, 2009.
- [39] B. H. Friemel, L. N. Bohs, K. R. Nightingale, and G. E. Trahey. Speckle decorrelation due to two-dimensional flow gradients. *IEEE Transactions on Ultrasonics, Ferroelectrics, and Frequency Control*, 45(2):317–327, 1998.
- [40] J. L. Gennisson, N. Grenier, R. Hubrecht, L. Couzy, Y. Delmas, M. Derieppe, S. Lepreux, P. Merville, A. Criton, J. Bercoff, and M. Tanter. Multiwave technology introducing shear wave elastography of the kidney: Pre-clinical study on a kidney fibrosis model and clinical feasibility study on 49 human renal transplants. In *Proceedings - IEEE Ultrasonics Symposium*, pages 1356–1359, 2010.
- [41] S. A. Goss, R. L. Johnston, and F. Dunn. Comprehensive compilation of empirical ultrasonic properties of mammalian tissues. *The Journal of the Acoustical Society of America*, 64(2):423–457, 1978.
- [42] A. Gronningsaeter. *Reduction of acoustic and electronic noise in intravascular ultrasound imaging*. PhD thesis, University of Trondheim, 1992.
- [43] M. F. Hamilton and D. T. Blackstock. *Nonlinear acoustics*. 1997.

- [44] M. Haque, C. Robinson, D. Owen, E. M. Yoshida, and A. Harris. Comparison of acoustic radiation force impulse imaging (ARFI) to liver biopsy histologic scores in the evaluation of chronic liver disease: A pilot study. *Annals of hepatology*, 9(3):289–93, 2010.
- [45] C. Hohl, T. Schmidt, P. Haage, D. Honnef, M. Blaum, G. Staatz, and R. W. Guenther. Phase-inversion tissue harmonic imaging compared with conventional B-mode ultrasound in the evaluation of pancreatic lesions. *European Radiology*, 14(6):1109–1117, 2004.
- [46] P. J. Hollender, S. J. Rosenzweig, K. R. Nightingale, and G. E. Trahey. Single- and multiple-track-location shear wave and acoustic radiation force impulse imaging: matched comparison of contrast, contrast-to-noise ratio and resolution. *Ultrasound in medicine & biology*, 41(4):1043–57, 2015.
- [47] S. Horster, P. Mandel, R. Zachoval, and D. A. Clevert. Comparing Acoustic Radiation Force Impulse Imaging to transient elastography to assess liver stiffness in healthy volunteers with and without valsalva manoeuvre. *Clinical Hemorheology and Microcirculation*, 46(2-3):159–168, 2010.
- [48] K. G. Ishak. Inherited metabolic diseases of the liver. *Clinics in Liver Disease*, 6(2):455–479, 2002.
- [49] J. A. Jensen, M. F. Rasmussen, M. J. Pihl, S. Holbek, C. A. Villagomez Hoyos, D. P. Bradway, M. B. Stuart, and B. G. Tomov. Safety Assessment of Advanced Imaging Sequences I: Measurements. *IEEE transactions on ultrasonics, ferro-electrics, and frequency control*, 2016.
- [50] K. Joshi, M. Mendler, R. Gish, R. Loomba, A. Kuo, H. Patton, and Y. Kono. Hepatocellular Carcinoma Surveillance: A National Survey of Current Practices in the USA, 2014.
- [51] M. Klysik, S. Garg, S. Pokharel, J. Meier, N. Patel, and K. Garg. Challenges of Imaging for Cancer in Patients with Diabetes and Obesity. *Diabetes technology & therapeutics*, 2014.
- [52] R. Lazebnik. Tissue Strain Analytics Virtual Touch Tissue Imaging and Quantification Tissue Strain Analytics Virtual Touch Tissue Imaging and Quantification. *Siemens Healthcare, Malvern, PA*, 2008.
- [53] T. Loupas, J. Powers, and R. Gill. An axial velocity estimator for ultrasound blood flow imaging, based on a full evaluation of the Doppler Equation by Means of a Two-Dimensional Autocorrelation Approach. *Ultrasonics*, 1995.
- [54] M. Lupsor, R. Badea, H. Stefanescu, Z. Sparchez, H. Branda, A. Serban, and A. Maniu. Performance of a new elastographic method (ARFI technology)

- compared to unidimensional transient elastography in the noninvasive assessment of chronic hepatitis C. Preliminary results. *Journal of gastrointestinal and liver diseases*, 18(3):303–310, 2009.
- [55] M. P. Manns and M. Kruger. Immunogenetics of chronic liver diseases. *Gastroenterology*, 106(6):1676–1697, 1994.
- [56] S. McAleavey, M. Menon, and E. Eleggbe. Shear modulus imaging with spatially-modulated ultrasound radiation force. *Ultrasonic imaging*, 31(4):217–234, 2009.
- [57] M. D. Miesner. Abdominal Ultrasound. In *Veterinary Techniques for Llamas and Alpacas*, pages 161–165. Wiley-Blackwell, 2013.
- [58] D. L. Miller, E. M. Driscoll, C. Dou, W. F. Armstrong, and B. R. Lucchesi. Microvascular permeabilization and cardiomyocyte injury provoked by myocardial contrast echocardiography in a canine model. *Journal of the American College of Cardiology*, 47(7):1464–1468, 2006.
- [59] P. Mishra and Z. M. Younossi. Abdominal ultrasound for diagnosis of nonalcoholic fatty liver disease (NAFLD). *The American journal of gastroenterology*, 102(12):2716–2717, 2007.
- [60] G. Montaldo, M. Tanter, J. Bercoff, N. Benech, and M. Fink. Coherent plane-wave compounding for very high frame rate ultrasonography and transient elastography. *IEEE Transactions on Ultrasonics, Ferroelectrics, and Frequency Control*, 56(3):489–506, 2009.
- [61] M. Mukaiya, M. Nishi, H. Miyake, and K. Hirata. Chronic liver diseases for the risk of hepatocellular carcinoma: a case-control study in Japan. Etiologic association of alcohol consumption, cigarette smoking and the development of chronic liver diseases., 1998.
- [62] I. Z. Nenadic, B. Qiang, M. W. Urban, L. H. de Araujo Vasconcelo, A. Nabavizadeh, A. Alizad, J. F. Greenleaf, and M. Fatemi. Ultrasound bladder vibrometry method for measuring viscoelasticity of the bladder wall. *Physics in medicine and biology*, 58(8):2675–95, 2013.
- [63] K. Nightingale, M. S. Soo, R. Nightingale, and G. Trahey. Acoustic radiation force impulse imaging: In vivo demonstration of clinical feasibility. *Ultrasound in Medicine and Biology*, 28(2):227–235, 2002.
- [64] K. R. Nightingale, C. C. Church, G. Harris, K. a. Wear, M. R. Bailey, P. L. Carson, H. Jiang, K. L. Sandstrom, T. L. Szabo, and M. C. Ziskin. Conditionally Increased Acoustic Pressures in Nonfetal Diagnostic Ultrasound Examinations Without Contrast Agents: A Preliminary Assessment. *Journal of Ultrasound in Medicine*, 34(7):1–41, 2015.

- [65] W. L. M. Nyborg, T. Litovitz, and C. Davis. Acoustic Streaming. In W. P. Mason, editor, *Physical Acoustics*, pages 265–331. Academic Press Inc, New York, 1965.
- [66] W. D. O’Brien. Ultrasound-biophysics mechanisms. *Progress in Biophysics and Molecular Biology*, 93(1-3):212–255, 2007.
- [67] S. O. Oktar, C. Yücel, H. Özdemir, A. Ulutürk, and S. Iik. Comparison of Conventional Sonography, Real-Time Compound Sonography, Tissue Harmonic Sonography, and Tissue Harmonic Compound Sonography of Abdominal and Pelvic Lesions. *American Journal of Roentgenology*, 181(5):1341–1347, 2003.
- [68] D. Ortega, P. N. Burns, D. Hope Simpson, and S. R. Wilson. Tissue harmonic imaging: Is it a benefit for bile duct sonography? *American Journal of Roentgenology*, 176(3):653–659, 2001.
- [69] M. L. Palmeri, Y. Deng, N. C. Rouze, and K. R. Nightingale. Dependence of shear wave spectral content on acoustic radiation force excitation duration and spatial beamwidth. *IEEE International Ultrasonics Symposium : [proceedings]. IEEE International Ultrasonics Symposium*, pages 1105–1108, 2014.
- [70] M. L. Palmeri, S. A. McAleavey, G. E. Trahey, and K. R. Nightingale. Ultrasonic tracking of acoustic radiation force-induced displacements in homogeneous media. *IEEE Transactions on Ultrasonics, Ferroelectrics, and Frequency Control*, 53(7):1300–1313, 2006.
- [71] M. L. Palmeri and K. R. Nightingale. On the thermal effects associated with radiation force imaging of soft tissue. *IEEE Transactions on Ultrasonics, Ferroelectrics, and Frequency Control*, 51(5):551–565, 2004.
- [72] M. L. Palmeri, M. H. Wang, J. J. Dahl, K. D. Frinkley, and K. R. Nightingale. Quantifying hepatic shear modulus in vivo using acoustic radiation force. *Ultrasound in medicine & biology*, 34(4):546–558, 2008.
- [73] M. L. Palmeri, M. H. Wang, N. C. Rouze, M. F. Abdelmalek, C. D. Guy, B. Moser, A. M. Diehl, and K. R. Nightingale. Noninvasive evaluation of hepatic fibrosis using acoustic radiation force-based shear stiffness in patients with nonalcoholic fatty liver disease. *Journal of Hepatology*, 55(3):666–672, 2011.
- [74] H. Park, J. Y. Park, D. Y. Kim, S. H. Ahn, C. Y. Chon, K.-H. Han, and S. U. Kim. Characterization of focal liver masses using acoustic radiation force impulse elastography. *World journal of gastroenterology : WJG*, 19(2):219–26, 2013.

- [75] A. D. Pierce. Acoustics: An Introduction to Its Physical Principles and Applications. 1989 Edition. *The Journal of the Acoustical Society of America*, 87(4):1826, 1990.
- [76] G. F. Pinton, J. Dahl, S. Rosenzweig, and G. E. Trahey. A heterogeneous nonlinear attenuating full-wave model of ultrasound. *IEEE Transactions on Ultrasonics, Ferroelectrics, and Frequency Control*, 56(3):474–488, 2009.
- [77] G. F. Pinton, J. J. Dahl, and G. E. Trahey. Rapid tracking of small displacements with ultrasound. *IEEE Trans. Ultrason., Ferroelec., Freq. Contr.*, 53(6):1103–1117, June 2006.
- [78] G. F. Pinton, G. E. Trahey, and J. J. Dahl. Sources of image degradation in fundamental and harmonic ultrasound imaging using nonlinear, full-wave simulations. *IEEE Transactions on Ultrasonics, Ferroelectrics, and Frequency Control*, 58(4):754–765, 2011.
- [79] F. Piscaglia, V. Salvatore, R. Di Donato, M. D’Onofrio, S. Gualandi, A. Gallotti, E. Peri, A. Borghi, F. Conti, G. Fattovich, E. Sagrini, A. Cucchetti, P. Andreone, and L. Bolondi. Accuracy of virtualTouch acoustic radiation force impulse (ARFI) imaging for the diagnosis of cirrhosis during liver ultrasonography. *Ultraschall in der Medizin*, 32(2):167–175, 2011.
- [80] T. Poynard, P. Bedossa, and P. Opolon. Natural history of liver fibrosis progression in patients with chronic hepatitis C. *Lancet*, 349(9055):825–832, 1997.
- [81] T. Poynard, M. Munteanu, E. Luckina, H. Perazzo, Y. Ngo, L. Royer, L. Fedchuk, F. Sattoune, R. Pais, P. Lebray, M. Rudler, D. Thabut, and V. Ratziu. Liver fibrosis evaluation using real-time shear wave elastography: Applicability and diagnostic performance using methods without a gold standard. *Journal of Hepatology*, 58(5):928–935, 2013.
- [82] I. Puls, D. Berg, M. Maurer, M. Schliesser, G. Hetzel, and G. Becker. Transcranial sonography of the brain parenchyma: Comparison of B-mode imaging and tissue harmonic imaging. *Ultrasound in Medicine and Biology*, 26(2):189–194, 2000.
- [83] N. C. Rouze, M. H. Wang, M. L. Palmeri, and K. R. Nightingale. Robust estimation of time-of-flight shear wave speed using a Radon sum transformation. *IEEE Trans. Ultrason., Ferroelec., Freq. Contr.*, 57(12):2662–2670, 2010.
- [84] A. P. Sarvazyan, O. V. Rudenko, S. D. Swanson, J. B. Fowlkes, and S. Y. Emelianov. Shear wave elasticity imaging: A new ultrasonic technology of medical diagnostics. *Ultrasound in Medicine and Biology*, 24(9):1419–1435, 1998.

- [85] S. Schuh, C. Man, A. Cheng, A. Murphy, A. Mohanta, R. Moineddin, G. Tomlinson, J. C. Langer, and A. S. Doria. Predictors of non-diagnostic ultrasound scanning in children with suspected appendicitis. *Journal of Pediatrics*, 158(1):123–129, 2011.
- [86] F. Sebag, J. Vaillant-Lombard, J. Berbis, V. Griset, J. F. Henry, P. Petit, and C. Oliver. Shear wave elastography: a new ultrasound imaging mode for the differential diagnosis of benign and malignant thyroid nodules. *The Journal of clinical endocrinology and metabolism*, 95(12):5281–5288, 2010.
- [87] T. Shiina, K. R. Nightingale, M. L. Palmeri, T. J. Hall, J. C. Bamber, R. G. Barr, L. Castera, B. I. Choi, Y.-H. Chou, D. Cosgrove, C. F. Dietrich, H. Ding, D. Amy, A. Farrokh, G. Ferraioli, C. Filice, M. Friedrich-Rust, K. Nakashima, F. Schafer, I. Sporea, S. Suzuki, S. Wilson, and M. Kudo. WFUMB Guidelines and Recommendations for Clinical Use of Ultrasound Elastography: Part 1: Basic Principles and Terminology. *Ultrasound in Medicine & Biology*, 41(5):1126–1147, 2015.
- [88] A. G. Singal, M. Nehra, B. Adams-Huet, A. C. Yopp, J. a. Tiro, J. a. Marrero, A. S. Lok, and W. M. Lee. Detection of hepatocellular carcinoma at advanced stages among patients in the HALT-C trial: where did surveillance fail? *The American journal of gastroenterology*, 108(3):425–32, 2013.
- [89] P. Song, H. Zhao, M. Urban, A. Manduca, S. Pislaru, R. Kinnick, C. Pislaru, J. Greenleaf, and S. Chen. Improved Shear Wave Motion Detection Using Pulse-Inversion Harmonic Imaging with a Phased Array Transducer. *IEEE transactions on medical imaging*, 32(12):2299–2310, 2013.
- [90] I. Sporea, S. Bota, A. Sftoiu, R. Sirli, O. Gradinaru-Tascau, A. Popescu, M. Lupsor Platon, C. Fierbinteanu-Braticevici, D. I. Gheonea, L. Sandulescu, and R. Badea. Romanian national guidelines and practical recommendations on liver elastography. *Medical ultrasonography*, 16(2):123–38, 2014.
- [91] H. C. Starritt, F. A. Duck, A. J. Hawkins, and V. F. Humphrey. The development of harmonic distortion in pulsed finite-amplitude ultrasound passing through liver. *Physics in medicine and biology*, 31(12):1401–1409, 1986.
- [92] T. A. Stiles, E. L. Madsen, and G. R. Frank. An Exposimetry System Using Tissue-Mimicking Liquid. *Ultrasound in Medicine and Biology*, 34(1):123–136, 2008.
- [93] J. D. Thomas and D. N. Rubin. Tissue harmonic imaging: Why does it work? In *Journal of the American Society of Echocardiography*, volume 11, pages 803–808, 1998.

- [94] M. J. Tong, N. S. El-Farra, A. R. Reikes, and R. L. Co. Clinical outcomes after transfusion-associated hepatitis C. *The New England journal of medicine*, 332(22):1463–1466, 1995.
- [95] J. Virmani, V. Kumar, N. Kalra, and N. Khandelwal. Characterization of Primary and Secondary Malignant Liver Lesions from B-Mode Ultrasound. *Journal of digital imaging : the official journal of the Society for Computer Applications in Radiology*, pages 3–6, 2013.
- [96] W. F. Walker and G. E. Trahey. Fundamental limit on delay estimation using partially correlated speckle signals. *IEEE Transactions on Ultrasonics, Ferroelectrics, and Frequency Control*, 42(2):301–308, 1995.
- [97] M. H. Wang, M. L. Palmeri, C. D. Guy, L. Yang, L. W. Hedlund, A. M. Diehl, and K. R. Nightingale. In vivo quantification of liver stiffness in a rat model of hepatic fibrosis with acoustic radiation force. *Ultrasound in medicine & biology*, 35(10):1709–1721, 2009.
- [98] M. H. Wang, M. L. Palmeri, V. M. Rotemberg, N. C. Rouze, and K. R. Nightingale. Improving the robustness of time-of-flight based shear wave speed reconstruction methods using RANSAC in human liver in vivo. *Ultrasound in Medicine and Biology*, 36(5):802–813, 2010.
- [99] K. A. Wear, P. M. Gammell, S. Maruvada, Y. Liu, and G. R. Harris. Improved measurement of acoustic output using complex deconvolution of hydrophone sensitivity. *IEEE transactions on ultrasonics, ferroelectrics, and frequency control*, 61(1):62–75, Jan. 2014.
- [100] A. Wieckowska, A. J. McCullough, and A. E. Feldstein. Noninvasive diagnosis and monitoring of nonalcoholic steatohepatitis: present and future. *Hepatology (Baltimore, Md.)*, 46(2):582–589, 2007.
- [101] J. H. Yoon, J. M. Lee, J. K. Han, and B. I. Choi. Shear wave elastography for liver stiffness measurement in clinical sonographic examinations: evaluation of intraobserver reproducibility, technical failure, and unreliable stiffness measurements. *Journal of ultrasound in medicine*, 33(3):437–47, Mar. 2014.
- [102] L. Zhai, J. Madden, W.-C. Foo, V. Mouraviev, T. J. Polascik, M. L. Palmeri, and K. R. Nightingale. Characterizing stiffness of human prostates using acoustic radiation force. *Ultrasonic imaging*, 32(4):201–213, 2010.
- [103] M. C. Ziskin. Specification of acoustic output level and measurement uncertainty in ultrasonic exposimetry. *IEEE Transactions on Ultrasonics, Ferroelectrics, and Frequency Control*, 50(8):1023–1034, 2003.

Biography

Yufeng Deng was born September 14, 1988 in Nanjing, Jiangsu, China. He grew up and stayed in Nanjing until the age of 15, and graduated from Raffles Institution, Singapore in 2008. He completed a B.S.E. in Biomedical Engineering at Duke University in 2011. He remained at Duke University for his Ph.D. in Biomedical Engineering, now completed in 2017. He took a 8 month internship at Siemens Healthcare in Mountain View, CA in 2013. He received the Morton H. Friedman Fellowship offered by the department of Biomedical Engineering at Duke University. He received IEEE IUS student travel award in 2014, and his paper was listed in the Editor's selection in IEEE Trans Ultrason Ferroelectr Freq Control in 2016.

Selected Other Publications

1. Y Deng, M.L. Palmeri, N.C. Rouze, G.F. Pinton, and K.R. Nightingale, "Image Quality Evaluation of Harmonic Imaging for Focused and Planar Transmissions Using Fullwave Simulations", IEEE Trans Ultrason Ferroelectr Freq Control, in Revision.
2. Y Deng, N.C. Rouze, M.L. Palmeri, and K.R. Nightingale, "Ultrasonic Shear Wave Elasticity Imaging Sequencing and Data Processing Using a Verasonics Research Scanner", IEEE Trans Ultrason Ferroelectr Freq Control, vol 64, no.1, pp. 164-176, 2017.
3. Y Deng, N.C. Rouze, M.L. Palmeri, and K.R. Nightingale, "On system-dependent sources of uncertainty and bias in ultrasonic quantitative shear-wave imaging", IEEE Trans Ultrason Ferroelectr Freq Control, vol 63, no.3, pp. 381-393, 2016.